DESIGN AND FABRICATION OF HIGH POWER MICROBATTERIES AND HIGH SPECIFIC STRENGTH CELLULAR SOLIDS FROM BICONTINUOUS MICROPOROUS HIERARCHICAL MATERIALS

BY

JAMES HENRY PIKUL

DISSERTATION

Submitted in partial fulfillment of the requirements
for the degree of Doctor of Philosophy in Mechanical Engineering
in the Graduate College of the
University of Illinois at Urbana-Champaign, 2015

Urbana, Illinois

Doctoral Committee:

Professor William King, Chair and Director of Research
Professor Paul Braun
Professor Placid Ferreira
Professor John Rogers

ABSTRACT

An emerging paradigm in engineering design is the development of materials by constructing hierarchical assemblies of simple building blocks into complex architectures that address physics at multiple length scales. These hierarchical materials are increasingly important for the next generation of mechanical, electrical, chemical, and biological technologies. However, fabricating hierarchical materials with nm control over multiple chemistries in a scalable fashion is a challenge yet to be overcome. This dissertation reports the design and fabrication of hierarchical microbattery electrodes that demonstrate unprecedented power density as well as hierarchical cellular solids with controllable modulus and high specific strength.

Self-assembly, electrodeposition and microfabrication enable the fabrication of microbatteries with hierarchical electrodes. The three-dimensional bicontinuous interdigitated microelectrode architecture improves power performance by simultaneously reducing ion and electron transport distances through the anode, cathode, and electrolyte. The microbattery power densities are up to 7.4 mW cm^{-2} μm^{-1}, which equals or exceeds that of the best supercapacitors and which is 2000 times higher than that of other microbatteries. A one dimensional electrochemical model of the microbatteries enables the study of physical processes that limit power performance. Lithium diffusion through the solid cathode most significantly limits the amount of energy extracted at high power density. Experimentally-validated design rules optimize and characterize the battery architecture for high power performance without the need for multiphysics based simulations. Electrochemical deposition techniques improve the microbattery energy density while maintaining high power density by allowing high volume fractions of electrochemically active material to be integrated into the high power architectures. The microbattery energy densities are up to 45.5 μWh cm^{-2} μm^{-1}, which is greater than

previously reported three-dimensional microbatteries and comparable to commercially available lithium-based batteries.

This dissertation also demonstrates the fabrication of 3D regular macroporous microcantilevers with Young's moduli that can be varied from 2.0 to 44.3 GPa. The porosity and deformation mode of the hierarchical material, which depends on the pore structure, determine the Young's moduli of the microcantilevers. The template technique allows 3D spatial control of the ordered porous structure and the ability to use a broad set of materials, demonstrated with nickel and alumina microcantilevers. Self-assembly and electrodeposition enable the scaling of the hierarchical microcantilever material to areas larger than cm^2. The large area nickel cellular solids have specific compressive strengths up to 0.23 MPa / (kg m^{-3}). The specific strength is greater than most high strength steels and titanium alloys and is due to the size strengthening effect of the nanometer scale struts in the porous architecture. The scalable fabrication and detailed characterization of the large area cellular solids provide a route for testing high strength cellular materials in a broader set of engineering applications not available to previous techniques whose material dimensions are limited to tens of micrometers.

To my dearly loved family, for their relentless support in my education.

Acknowledgements:

I am extremely grateful for the support of my advisors William King and Paul Braun. Their different advising approaches provided me with a well rounded perspective of science and engineering. I am thankful for Bill and Paul's effort into bettering me as a person and scholar. I am especially grateful to Bill for his wisdom and dedication to improving my soft skills, and to Paul for welcoming me into his group and for his excellent experimental guidance.

I am also grateful to my committee members Dr. Placid Ferreira and Dr. John Rogers for their guidance and support beginning with my first project at Illinois. I deeply respect their leadership, capabilities, and insight.

I greatly value all the friendships I made at Illinois. Many of my friends started as work colleagues and together we endured the trials and tribulations of graduate school. Suhas Somnath and Hoe Joon Kim provided me invaluable support and friendship as we navigated the MechSE PhD process from start to finish. I am especially grateful to Huigang Zhang for teaching me how to build and test batteries. Jiung Cho, Kevin Arpin, Hailong Ning, Junjie Wang, and Chunjie Zhang were instrumental in teaching me new ways to approach science and create new materials. Elise Corbin, Curtis Johnson, and Kyle Grosse gave me lots of insight and provided me with lots of laughter and happiness. My DOE SCGF colleagues and Illinois cohort, Matt Rosenberger, Johnny Felts, and Peter Fiflis, opened my mind with many great conversations about the universe, particle physics, and nuclear engineering. Finally, Erik Johnson has been one of my best friends since we were young adults, and we are finishing our PhDs together. Thank you for all the memorable moments and for introducing me to many more friends.

I would also like to thank my family. My parents, Henry and Elizabeth; sister, Jacqueline; and grandma, Stephanie, have been instrumental in supporting me throughout my education. Thank you for visiting on weekends, becoming Illini fans, and for always guiding me in the right direction. I get my best traits from my parents. Last, but most importantly, I would like to thank my wife, Rhiannon Jerch, who I met in my first week at Illinois. Rhiannon has shifted from driver to passenger in this adventure as often as I have. Thank you for your love, for always being there, and for making me a better person every day.

TABLE OF CONTENTS

LIST OF SYMBOLS AND ABBREVIATIONS

1-D	One dimensional
2-D	Two dimensional
3-D	Three dimensional
A	Area
ALD	Atomic layer deposition
AFM	Atomic force microscope
b	Interconnect diameter
c	Concentration
σ	Stress or conductivity
$Crate$	C rate of discharge
ρ	density
D	Diffusivity
D_c	Polystyrene diameter corresponding to t_o
DMC	Dimethyl carbonate
ε	Volume fraction
E	elastic modulus
EC	Ethylene carbonate
F	Faraday constant [96,485.3365 A s mol^{-1}]
FCC	Face centered cubic
FIB	Focused Ion Beam
G	Shear modulus
h, $h2$	Spherical cap height

H.-S.	Hashin – Shtrikman
H	Electrode height
i,I	Current
K	Bulk modulus
k	Electrode conductivity or spring constant
l	Length
L	Electrode length or cantilever length
n	Shape factor
OCV	Open circuit voltage
P	Electrode pitch
PC	Propylene carbonate
PITT	Potentiostatic intermittent titration technique
PS	Polystyrene
$\dot{q}$	Depletion rate (in electrolyte)
R	Polystyrene radius, or resistance
ρ	Resistivity
SEI	Solid electrolyte interphase
SEM	Scanning electron microscopy
t	Active material thickness or cantilever thickness
τ	Time
t^+	Transference number
V	Voltage or volume
W	Electrode width or cantilever width

Subscripts

act	Active material
b	Bulk
c	Critical, Cellular
e	Electrolyte
i	Electrode with the lowest total capacity
n	Sintered polystyrene
neg	Negative electrode
Ni	Nickel
o	Optimal
pos	Positive electrode
s	Solid component
sep	Separator or region between electrodes
v	Central void
void	Void (Non-solid pore space in between polystyrene particles)

Superscripts

0	Initial condition
eff	Effective
max	Maximum

CHAPTER 1

INTRODUCTION

1.1 Hierarchical materials that address multiple length scales

Historically, engineers have used top-down methods to develop large scale materials (like steel) and technologies (like long range communication) that are superior in their capabilities to those engineered by nature (*1*). The enhanced properties over natural materials and technologies are in part due to the engineer's ability to processes and shape different bulk materials in environments that are rare in nature, like high temperature or vacuum. However, engineers and scientists have yet to match nature's ability to engineer nanoscale materials (*2-4*). The interaction of objects at the nanometer scale controls function at micro and macroscopic scales in many physical processes. Biology is ripe with examples, but there are also many engineering applications including the transport of ions and electrons in batteries (*5*), the attraction of water to a surface (*6-8*), and the strength of materials among many others (*4, 9*). An emerging paradigm in engineering design is the development of materials by constructing hierarchical assemblies of simple building blocks into complex architectures that address physics at multiple length scales. This bottom up approach is enabling engineers to match nature's ability to design across multiple length scales and develop hierarchical materials with superior properties.

Hierarchical materials are materials that have controlled structure at more than one length scale (*10, 11*). The Eiffel Tower is an engineered structure with 3 levels of hierarchy, or third order hierarchy. The hierarchical order is the number of levels of scale with a recognized structure. Materials and structures developed by engineers typically have only a few hierarchical orders, but natural materials like wood and bone can have a hierarchical order of 10 or more

(*10*). The hierarchical order of a material can be used to address one or more unique physical process and ultimately develop advanced engineering materials.

The design of hierarchical materials across multiple length scales requires advanced fabrication technologies that allow for scalable control over nanometer structures and chemistry. Materials with nanometer control over structure can be fabricated with several techniques including direct writing of functional inks (*12*), laser writing in a photoresist (*13*), and layer-by-layer stacking (*14*). However, these processes are serial and require a large amount of time and expense to fabricate large areas or volumes of material. Self-assembly and holographic lithography allow for parallel fabrication of materials with control over multiple length scales covering areas larger than cm^2 (*15-21*). Self-assembly is a powerful tool for controlling interactions at the nanometer scale while simultaneously allowing these interactions to occur with many moles of objects such that the process can be rapidly scaled to large area or volumes with minimal energy input. Colloidal self-assembly is used in this thesis to fabricate hierarchical materials (*17, 22, 23*).

The chemistry of materials made by self-assembly can be controlled through a number of chemical deposition techniques. Chemical inversion is a common technique where a metallic, dielectric, semiconducting or polymeric material is filled into the voids of the self-assembled structure, after which the self-assembled structure is sacrificed. These inverted structures can then be further modified by coating them with conformal films with a wide variety of materials properties. Chemical vapor deposition (*24-26*), atomic layer deposition (*27*), liquid precursor infiltration (*28, 29*), nanoparticle infiltration (*30*), and electrodeposition are the most common material deposition techniques used (*31, 32*).

The combination of self-assembly and modern materials deposition techniques allows for nanometer control of structure and chemistry in scalable architectures that can address multiple length scales up to the macroscopic. This thesis reports the design and fabrication of hierarchical materials and their applications towards improving the power density of batteries, integrating microbatteries with microelectronics, and improving the mechanical properties of cellular materials.

1.2 Hierarchical structuring of batteries for high power density

Electrochemical batteries that convert chemical energy to electrical energy are one of the most important and widely used technologies for energy storage. The energy density and power density are the two primary metrics for characterizing the performance of a battery. Energy density is the amount of energy stored per unit volume or weight. Power density is the rate at which that energy can be extracted from the battery. A lot of work has gone into improving the energy density of batteries beyond 150 Wh kg^{-1} and 350 Wh L^{-1} (*33, 34*), with nanometer sized materials making considerable impact in improving the cycle life of high capacity materials like silicon which undergo up to 400% strains during lithiation and de-lithiation (*35*). However, the full potential of batteries cannot be realized until the energy stored can be instantly and fully available when required. Most commercial batteries require at least one hour or more to fully charge or discharge the energy stored inside the battery (*5*). Applications such as load leveling and regenerative braking would immediately benefit form improvements in the power density of batteries (*36-38*). In addition, improving the power density of batteries could enable a whole host of other applications including the ability to charge an electric vehicle in less than ten minutes or send high fidelity signals over long distances using microelectronics (*39, 40*).

Improvements in power density have generally focused on improving the electrical and ionic conductivity, diffusivity and other transport properties of individual battery materials (*41-46*); however, it is an incredible challenge to develop new materials with thermodynamic properties that enable high energy density while simultaneously providing dramatic improvements in transport properties. In addition, the transport properties in each of the many battery components need to be simultaneously optimized as the power density of a battery is limited by the component with the slowest kinetics. High power densities up to 1000 $\mu W\ cm^{-2}\ \mu m^{-1}$ have been demonstrated in porous battery electrodes that reduce ion diffusion through the electrochemically active anode or cathode materials, referred to as active material in this work, as well as designs that reduce ion diffusion time in the electrolyte and decrease electrical resistance in the electrodes (*47-53*). Most publications focus on improving power density at the expense of energy density in individual battery components with experimental half-cells. A half-cell is an anode or cathode tested versus a reference electrode, typically lithium metal in lithium ion batteries. Such cells are useful for studying the physics of battery components, but improvements in the power density of single battery materials or electrode components do not directly translate to improved power densities in full batteries as there are many engineering design constraints in the anode, cathode, electrolyte and supporting non-electrochemically active materials that are required to realize a complete high power battery. Additionally the transport properties in the anode and cathode active materials, electrolyte, and fillers vary over many orders of magnitude. For example, the diffusivity of lithium salt in an electrolyte is typically $10^{-6}\ cm^2\ s^{-1}$, whereas lithium diffusivity in solid active materials can vary between 10^{-10} and $10^{-14}\ cm^2\ s^{-1}$ (*54*). The structuring of battery materials, or composites of multiple materials, over multiple length scales has been shown to improve power density by simultaneously addressing the

transport resistance across multiple transport physics (*5, 32, 55-63*). **Chapter 2** demonstrates the development of high power density microbatteries constructed from interdigitated three-dimensional bicontinuous nanoporous electrodes that simultaneously reduce diffusion distances in the active material and electrolyte as well as reduce electrical resistance through the electrodes and electrolyte, while maintaining a large percentage of active material (*22*). This bicontinuous battery architecture allows for control over length scales from tens of nanometers to millimeters. There have only been a few demonstrations of complete battery cells that achieve ultra-high power density by reducing the transport resistances for all major physics with structural control of the transport lengths (*22, 64*).

In addition to the limited number of experimental demonstrations of ultra-high power density batteries, there lacks an in depth understanding of the physical processes that most limit power density and experimentally validated design rules for designing ultra-high power density batteries. Simulations of batteries have in the past provided detailed characterization and design optimization of conventional batteries, but these models have not been validated at C rates greater than 10 C (*65-73*). Batteries that have been modeled at higher rates have been limited to applications with short pulses or in combination with supercapacitors (*74-77*). A one-dimensional (1-D) electrochemical model based on work by Newman et al. was used to study the discharge performance of a hybrid electric vehicle battery at discharge rates up to 25 C (*65, 66, 71, 78*). **Chapter 3** adapts the 1-D electrochemical model developed by Newman et al. to model the high power performance of the bicontinuous electrodes, explore which physical processes limit power performance, and develop design rules for high power batteries.

1.3 Hierarchical structuring of batteries for microelectronics integration

The integration of miniature sensors, radio devices, and other electronics into consumer and industrial goods has driven significant interest in miniature energy storage technologies that can power these integrated electronics (*79*); however, there has been much less progress in the miniaturization and integration of power sources compared to electronic components (*55*). Capacitors can be directly integrated into electronics, but capacitors have poor energy density compared to batteries (*80-82*). Batteries have considerably more energy density than capacitors, but are limited in their power performance and have proven difficult to miniaturize and integrate. Thin film microbatteries formed by a layered anode, solid electrolyte, cathode structure are commercially available, but their low areal energy densities, 70 – 600 μWh cm^{-2}, are insufficient for most microelectronics applications (*83*). Microbatteries based on 3-D electrodes have areal energy densities greater than 3.5 mWh cm^{-2}, but at the cost of low volumetric energy and power densities relative to macroscale conventional lithium ion batteries, limiting their use (*55*, *83-92*). Typical volumetric energy and power densities are around 10-60 μWh cm^{-2} μm^{-1} and 1-100 μW cm^{-2} μm^{-1} for conventional lithium ion batteries. An ideal microbattery electrode would provide both high volumetric power and energy density comparable to conventional format batteries in a 3-D electrode architecture that can simultaneously offer high areal energy and power density as well as be easily integrated into microelectronics. It is challenging to integrate 3-D electrodes into a complete microbattery cell, owing to the difficulty of integrating 3-D elements of anode and cathode materials without cross-contamination, along with the need to control materials uniformity and feature sizes across a range of lengths scales 10 nm – 1 mm. **Chapter 2** demonstrates how an interdigitated bicontinuous architecture combined with electrodeposition allows for precise integration of 3-D microbattery electrodes with high energy and power

density. **Chapter 4** integrates primary battery chemistry into the bicontinuous architecture and demonstrates techniques for depositing high volume fractions of high capacity materials for microbatteries with improved energy density and high power density.

1.4 Hierarchical structuring of cellular solids for unique mechanical properties

Materials with a hierarchical structure can have dramatically different properties compared to their bulk form (*10*, *11*). In particular, the hierarchical pore structure of cellular solids allows for a large range of mechanical properties and densities (*93*). Cellular solids are materials made from an assembly of cells enclosed with solid edges or faces (*94*). Wood, bone, and coral are examples of cellular solids with unique mechanical properties that are prevalent in nature. Cellular solids are also widely used in engineering applications from cardboard to ceramic foams that insulate the Space Shuttle during atmospheric reentry. Cellular solids deform mechanically either through stretching or bending dominated modes (*95*). The elastic modulus, yield stress, and other mechanical properties can be related to the relative density of the cellular solid. The elastic modulus of a cellular material, E_c, is related to the bulk elastic modulus, E_b, by

$$E_c = C_1 E_b \left(\frac{\rho_c}{\rho_b}\right)^{k_1}, \tag{1.2}$$

where ρ_c and ρ_b are the densities of the cellular and bulk materials. The yield stress of a cellular material, σ_c, depends on the yield stress of the bulk materials, σ_b, through a similar relationship

$$\sigma_c = C_2 \sigma_b \left(\frac{\rho_c}{\rho_b}\right)^{k_2}, \tag{1.3}$$

where C_1, C_2, k_1 and k_2 are constants that depend on the geometry and deformation mode of the foam (*96*). $C_1 = 1$, $C_2 = 0.3$, $k_1 = 2$ and $k_2 = 3/2$ for open-cell foams, which are the most common

cellular material and generally deform due to bending of the struts that connect the joints in the foam architecture (*94, 95*). Cellular material that deform due to stretching have mechanical properties that are linearly related to the bulk material properties, with the octet-truss structure regarded as the best stretch dominated isotropic cellular structure (*95, 97-99*). **Chapter 5** demonstrates the integration of regular porous cellular materials into micromechanical devices and discusses how such architectures can lead to unique mechanical and physical properties.

A large body of research has been directed towards developing cellular solids with high specific strength. Equation 1.3 shows how the deformation mode affects the strength of a porous solid. Even in the case of complete elastic deformation in a single direction, the specific strength of a porous solid cannot exceed the specific strength of the bulk material unless some feature of the porous solid increases the strength of the material it is made of. It is well known that the strength of a material can be enhanced by reducing the critical flaw size (*100*). The Hall-Petch relationship between grain size and strength is the most widely studied relationship between strength and flaw size (*101, 102*); however, a reduced grain size also improves the strength of the bulk material, giving no strength benefit to the porous structure. At small grain sizes less than 100 nm the Hall-Petch relationship is no longer valid and a maximum strength occurs (*103-105*). More recently, strength enhancement based on a mechanical size effect has been studied (*106, 107*). Compression tests on micropillars have shown that reducing the pillar diameter leads to significant strengthening (*106, 107*). The strength of the pillar can approach the theoretical strength of the pillar material when the diameter is less than 100 nm (*108-111*). This size effect has been introduced to cellular materials where the strut thickness or diameter is reduced to less than 100 nm to improve the strength of the strut and thus improve the strength of the cellular material (*112-114*).

Several studies have demonstrated interesting strength and deformation mechanisms due to this size effect (*112, 115, 116*). These studies show much promise for developing cellular materials with macroscopic mechanical properties beyond the capabilities of today's materials. There are; however, several challenges to overcome to meet this goal. The first challenge is scaling cellular solids with nanometer sized struts to bulk sizes greater than 100's of μm so they can be realized as engineering materials and integrated into mechanical devices. Fabrication technologies like two photon lithography and 3D direct laser writing have been used to fabricate nm precise cellular solid architectures but these techniques are serial and yield materials with bulk dimensions around 10 μm (*112-114, 117-119*). Polymer waveguides and microstereolithography were used to fabricate cellular structures scalable to mm or larger bulk dimensions, but these techniques lack nm control over structural dimensions besides surface coating thickness (*117, 120*). Electrochemical de-alloying of gold-silver alloys enabled mm^2 and larger samples of porous gold with the same macroscopic strength of bulk gold (*111, 115, 121-124*). The relatively easy manufacturing method, comprehensive nanoindentation and micropillar compression experiments, and mechanical simulations made these materials easy to study; however, their high cost of raw materials and low specific strength of 16 MPa / (Mg m^{-3}) due to the high density and low yield stress of bulk gold severely limit the applications of nanoporous gold. Self-assembly based techniques like those developed in nature have the potential to provide nm control over structure while being scalable to areas larger than cm^2 (*4, 10, 15, 17, 21*). A few cellular materials based on the self-assembly of opal based structures have been reported (*125, 126*). The first study demonstrated a size effect on the hardness of the cellular solids that depended on pore size, but detailed analysis and strength measurements were not provided (*125*). Recently inverse opals made of SiO_2 and TiO_2 have demonstrated high specific strength between

145 and 369 MPa / (Mg m^{-3}), which is higher than nano cellular materials with octet truss architectures and shows promise for future materials based on self-assembly fabrication (*126*). A cellular material that demonstrates high specific strength, can be controlled across multiple dimensions, is easy to fabricate with multiple materials, and whose deformation mode is understood would enable many engineering applications and provide and more available method for studying the strength enhancement due to the size effect. **Chapter 6** demonstrates the use of self-assembly to create cm^2 of cellular solids with specific compressive strengths greater than 0.2 MPa / (kg m^{-3}), greater than most high strength steels and titanium alloys. The cellular solids are made with nickel and rhenium electrodeposited at room temperature. The deformation mode of the nickel inverse opal is modeled and combined with data on different strut diameters to develop relations between the cellular geometry and material strength.

1.5 References

1. S. Vogel, *Cats' paws and catapults: Mechanical worlds of nature and people*. (WW Norton & Company, 2000).
2. K. Schmidt-Nielsen, *Scaling: why is animal size so important?* , (Cambridge University Press, 1984).
3. D. W. Thompson, On growth and form. *On growth and form.*, (1942).
4. U. G. K. Wegst, H. Bai, E. Saiz, A. P. Tomsia, R. O. Ritchie, Bioinspired structural materials. *Nat Mater* **14**, 23 (2015).
5. P. V. Braun, J. Cho, J. H. Pikul, W. P. King, H. Zhang, High power rechargeable batteries. *Curr. Opin. Solid State Mater. Sci.* **16**, 186 (2012).
6. N. Giovambattista, P. G. Debenedetti, P. J. Rossky, Effect of Surface Polarity on Water Contact Angle and Interfacial Hydration Structure. *The Journal of Physical Chemistry B* **111**, 9581 (2007/08/01, 2007).
7. G. Azimi, R. Dhiman, H.-M. Kwon, A. T. Paxson, K. K. Varanasi, Hydrophobicity of rare-earth oxide ceramics. *Nat Mater* **12**, 315 (2013).
8. L. Feng *et al.*, Super-Hydrophobic Surfaces: From Natural to Artificial. *Advanced Materials* **14**, 1857 (2002).
9. W. D. Callister, D. G. Rethwisch, *Materials science and engineering: an introduction*. (Wiley New York, 2007), vol. 7.
10. P. Fratzl, R. Weinkamer, Nature's hierarchical materials. *Progress in Materials Science* **52**, 1263 (2007).
11. R. Lakes, Materials with structural hierarchy. *Nature* **361**, 511 (1993).
12. G. M. Gratson *et al.*, Direct-Write Assembly of Three-Dimensional Photonic Crystals: Conversion of Polymer Scaffolds to Silicon Hollow-Woodpile Structures. *Advanced Materials* **18**, 461 (2006).
13. G. Von Freymann *et al.*, Three-Dimensional Nanostructures for Photonics. *Advanced Functional Materials* **20**, 1038 (2010).
14. S. Noda, K. Tomoda, N. Yamamoto, A. Chutinan, Full three-dimensional photonic bandgap crystals at near-infrared wavelengths. *Science* **289**, 604 (2000).
15. K. A. Arpin *et al.*, Multidimensional architectures for functional optical devices. *Advanced Materials* **22**, 1084 (2010).
16. K. A. Arpin, J. H. Pikul, W. P. King, H. Fan, P. V. Braun, Template directed assembly of dynamic micellar nanoparticles. *Soft Matter* **7**, 10252 (2011).
17. P. Jiang, J. F. Bertone, K. S. Hwang, V. L. Colvin, Single-Crystal Colloidal Multilayers of Controlled Thickness. *Chem. Mater.* **11**, 2132 (1999/08/01, 1999).
18. S. Jeon *et al.*, Fabricating complex three-dimensional nanostructures with high-resolution conformable phase masks. *Proceedings of the National Academy of Sciences of the United States of America* **101**, 12428 (Aug, 2004).
19. H. Ning *et al.*, Holographic patterning of high-performance on-chip 3D lithium-ion microbatteries. *Proceedings of the National Academy of Sciences*, (May 11, 2015, 2015).
20. Y. Lin *et al.*, Self-directed self-assembly of nanoparticle/copolymer mixtures. *Nature* **434**, 55 (2005).
21. C. Park, J. Yoon, E. L. Thomas, Enabling nanotechnology with self assembled block copolymer patterns. *Polymer* **44**, 6725 (2003).
22. J. H. Pikul, H. Gang Zhang, J. Cho, P. V. Braun, W. P. King, High-power lithium ion microbatteries from interdigitated three-dimensional bicontinuous nanoporous electrodes. *Nat. Commun.* **4**, 1732 (2013).
23. H. P. James *et al.*, Micromechanical devices with controllable stiffness fabricated from regular 3D porous materials. *Journal of Micromechanics and Microengineering* **24**, 105006 (2014).

24. G. von Freymann *et al.*, Tungsten inverse opals: The influence of absorption on the photonic band structure in the visible spectral region. *Appl. Phys. Lett.* **84**, 224 (2004).
25. A. Blanco *et al.*, Large-scale synthesis of a silicon photonic crystal with a complete three-dimensional bandgap near 1.5 micrometres. *Nature* **405**, 437 (2000).
26. H. Zhang, P. V. Braun, Three-Dimensional Metal Scaffold Supported Bicontinuous Silicon Battery Anodes. *Nano Letters* **12**, 2778 (2012/06/13, 2012).
27. K. A. Arpin *et al.*, Three-dimensional self-assembled photonic crystals with high temperature stability for thermal emission modification. *Nat Commun* **4**, (2013).
28. B. T. Holland, C. F. Blanford, A. Stein, Synthesis of Macroporous Minerals with Highly Ordered Three-Dimensional Arrays of Spheroidal Voids. *Science* **281**, 538 (July 24, 1998, 1998).
29. A. Imhof, D. J. Pine, Ordered macroporous materials by emulsion templating. *Nature* **389**, 948 (1997).
30. Y. A. Vlasov, N. Yao, D. J. Norris, Synthesis of Photonic Crystals for Optical Wavelengths from Semiconductor Quantum Dots. *Advanced Materials* **11**, 165 (1999).
31. K. A. Arpin, M. D. Losego, P. V. Braun, Electrodeposited 3D tungsten photonic crystals with enhanced thermal stability. *Chem. Mater.* **23**, 4783 (2011).
32. H. Zhang, X. Yu, P. V. Braun, Three-dimensional bicontinuous ultrafast-charge and -discharge bulk battery electrodes. *Nat. Nanotechnol.* **6**, 277 (2011).
33. J. M. Tarascon, M. Armand, Issues and challenges facing rechargeable lithium batteries. *Nature* **414**, 359 (2001).
34. M. Armand, J. M. Tarascon, Building better batteries. *Nature* **451**, 652 (2008).
35. P. G. Bruce, B. Scrosati, J.-M. Tarascon, Nanomaterials for Rechargeable Lithium Batteries. *Angewandte Chemie International Edition* **47**, 2930 (2008).
36. B. Dunn, H. Kamath, J.-M. Tarascon, Electrical Energy Storage for the Grid: A Battery of Choices. *Science* **334**, 928 (November 18, 2011, 2011).
37. R. Kötz, M. Carlen, Principles and applications of electrochemical capacitors. *Electrochim. Acta* **45**, 2483 (2000).
38. C. Fellner, J. Newman, High-power batteries for use in hybrid vehicles. *J. Power Sources* **85**, 229 (2000).
39. R. A. Huggins, Supercapacitors and electrochemical pulse sources. *Solid State Ionics* **134**, 179 (2000).
40. P. Chulsung, K. Lahiri, A. Raghunathan, in *Sensor and Ad Hoc Communications and Networks, 2005. IEEE SECON 2005. 2005 Second Annual IEEE Communications Society Conference on*. (2005), pp. 430-440.
41. J.-S. Kim *et al.*, A Truncated Manganese Spinel Cathode for Excellent Power and Lifetime in Lithium-Ion Batteries. *Nano Letters* **12**, 6358 (2012/12/12, 2012).
42. J. M. Feckl, K. Fominykh, M. Döblinger, D. Fattakhova-Rohlfing, T. Bein, Nanoscale Porous Framework of Lithium Titanate for Ultrafast Lithium Insertion. *Angewandte Chemie International Edition* **51**, 7459 (2012).
43. Z.-S. Wu, W. Ren, L. Xu, F. Li, H.-M. Cheng, Doped Graphene Sheets As Anode Materials with Superhigh Rate and Large Capacity for Lithium Ion Batteries. *ACS Nano* **5**, 5463 (2011/07/26, 2011).
44. S.-T. Myung *et al.*, Black anatase titania enabling ultra high cycling rates for rechargeable lithium batteries. *Energy & Environmental Science* **6**, 2609 (2013).
45. H.-G. Jung, M. W. Jang, J. Hassoun, Y.-K. Sun, B. Scrosati, A high-rate long-life Li4Ti5O12/Li[Ni0.45Co0.1Mn1.45]O4 lithium-ion battery. *Nat Commun* **2**, 516 (2011).
46. H. Wu *et al.*, Stable cycling of double-walled silicon nanotube battery anodes through solid-electrolyte interphase control. *Nat Nano* **7**, 310 (2012).
47. K. Brezesinski *et al.*, Ordered Mesoporous alpha-Fe_2O_3 (Hematite) Thin-Film Electrodes for Application in High Rate Rechargeable Lithium Batteries. *Small* **7**, 407 (Feb, 2011).

48. H. G. Zhang, X. D. Yu, P. V. Braun, Three-dimensional bicontinuous ultrafast-charge and -discharge bulk battery electrodes. *Nat. Nanotechnol.* **6**, 277 (May, 2011).
49. A. Esmanski, G. A. Ozin, Silicon Inverse-Opal-Based Macroporous Materials as Negative Electrodes for Lithium Ion Batteries. *Advanced Functional Materials* **19**, 1999 (2009).
50. N. S. Ergang *et al.*, Photonic Crystal Structures as a Basis for a Three-Dimensionally Interpenetrating Electrochemical-Cell System. *Advanced Materials* **18**, 1750 (2006).
51. J. S. Sakamoto, B. Dunn, Hierarchical battery electrodes based on inverted opal structures. *Journal of Materials Chemistry* **12**, 2859 (2002).
52. L. Taberna, S. Mitra, P. Poizot, P. Simon, J. M. Tarascon, High rate capabilities Fe_3O_4-based Cu nano-architectured electrodes for lithium-ion battery applications. *Nat. Mater.* **5**, 567 (2006).
53. M. Yao *et al.*, Nickel substrate having three-dimensional micronetwork structure for high-power nickel/metal-hydride battery. *Electrochemical and Solid State Letters* **10**, A56 (2007).
54. M. Park, X. Zhang, M. Chung, G. B. Less, A. M. Sastry, A review of conduction phenomena in Li-ion batteries. *J. Power Sources* **195**, 7904 (2010).
55. T. S. Arthur *et al.*, Three-dimensional electrodes and battery architectures. *MRS Bulletin* **36**, 523 (2011).
56. Y. Tang, Y. Zhang, W. Li, B. Ma, X. Chen, Rational material design for ultrafast rechargeable lithium-ion batteries. *Chemical Society Reviews*, (2015).
57. S. Lee, Y. Cho, H.-K. Song, K. T. Lee, J. Cho, Carbon-Coated Single-Crystal LiMn2O4 Nanoparticle Clusters as Cathode Material for High-Energy and High-Power Lithium-Ion Batteries. *Angewandte Chemie International Edition* **51**, 8748 (2012).
58. S. Chen *et al.*, Self-supported Li4Ti5O12 nanosheet arrays for lithium ion batteries with excellent rate capability and ultralong cycle life. *Energy & Environmental Science* **7**, 1924 (2014).
59. M. A. Martin *et al.*, Morphological Influence in Lithium-Ion Battery 3D Electrode Architectures. *J. Electrochem. Soc.* **162**, A991 (January 1, 2015, 2015).
60. A. Shah *et al.*, A Layered Carbon Nanotube Architecture for High Power Lithium Ion Batteries. *J. Electrochem. Soc.* **161**, A989 (January 1, 2014, 2014).
61. Y. Tang *et al.*, Unravelling the Correlation between the Aspect Ratio of Nanotubular Structures and Their Electrochemical Performance To Achieve High-Rate and Long-Life Lithium-Ion Batteries. *Angewandte Chemie International Edition* **53**, 13488 (2014).
62. A. S. Westover *et al.*, On-chip high power porous silicon lithium ion batteries with stable capacity over 10 000 cycles. *Nanoscale* **7**, 98 (2015).
63. X. Wang *et al.*, Cu/Li4Ti5O12 scaffolds as superior anodes for lithium-ion batteries. *NPG Asia Mater* **7**, e171 (2015).
64. C. Liu *et al.*, An all-in-one nanopore battery array. *Nat Nano* **9**, 1031 (2014).
65. M. Doyle, J. Newman, A. S. Gozdz, C. N. Schmutz, J.-M. Tarascon, Comparison of Modeling Predictions with Experimental Data from Plastic Lithium Ion Cells. *J. Electrochem. Soc.* **143**, 1890 (1996).
66. T. F. Fuller, M. Doyle, J. Newman, Simulation and Optimization of the Dual Lithium Ion Insertion Cell. *J. Electrochem. Soc.* **141**, 1 (January 1, 1994, 1994).
67. M. Doyle, J. Newman, Modeling the performance of rechargeable lithium-based cells: design correlations for limiting cases. *J. Power Sources* **54**, 46 (1995).
68. Á. G. Miranda, C. W. Hong, Integrated modeling for the cyclic behavior of high power Li-ion batteries under extended operating conditions. *Applied Energy* **111**, 681 (2013).
69. C. Min, G. A. Rincon-Mora, Accurate electrical battery model capable of predicting runtime and I-V performance. *Energy Conversion, IEEE Transactions on* **21**, 504 (2006).
70. I. Papic, Simulation model for discharging a lead-acid battery energy storage system for load leveling. *Energy Conversion, IEEE Transactions on* **21**, 608 (2006).
71. P. Arora, M. Doyle, A. S. Gozdz, R. E. White, J. Newman, Comparison between computer simulations and experimental data for high-rate discharges of plastic lithium-ion batteries. *J. Power Sources* **88**, 219 (2000).

72. O. Tremblay, L. A. Dessaint, A. I. Dekkiche, in *Vehicle Power and Propulsion Conference, 2007. VPPC 2007. IEEE*. (2007), pp. 284-289.
73. K. Smith, C.-Y. Wang, Solid-state diffusion limitations on pulse operation of a lithium ion cell for hybrid electric vehicles. *J. Power Sources* **161**, 628 (2006).
74. D. Cericola, P. W. Ruch, R. Kötz, P. Novák, A. Wokaun, Simulation of a supercapacitor/Li-ion battery hybrid for pulsed applications. *J. Power Sources* **195**, 2731 (2010).
75. S. Buller, M. Thele, R. W. A. A. De Doncker, E. Karden, Impedance-based simulation models of supercapacitors and Li-ion batteries for power electronic applications. *Industry Applications, IEEE Transactions on* **41**, 742 (2005).
76. B. Schweighofer, K. M. Raab, G. Brasseur, Modeling of high power automotive batteries by the use of an automated test system. *Instrumentation and Measurement, IEEE Transactions on* **52**, 1087 (2003).
77. P. M. Gomadam, J. W. Weidner, R. A. Dougal, R. E. White, Mathematical modeling of lithium-ion and nickel battery systems. *J. Power Sources* **110**, 267 (2002).
78. K. Smith, C.-Y. Wang, Power and thermal characterization of a lithium-ion battery pack for hybrid-electric vehicles. *J. Power Sources* **160**, 662 (2006).
79. V. Narain, "Global thin-film batteries (TFB) market" (Frost and Sullivan, 2013).
80. C. Liu, Z. Yu, D. Neff, A. Zhamu, B. Z. Jang, Graphene-Based Supercapacitor with an Ultrahigh Energy Density. *Nano Letters* **10**, 4863 (2010/12/08, 2010).
81. Y. Zhu *et al.*, Carbon-Based Supercapacitors Produced by Activation of Graphene. *Science* **332**, 1537 (June 24, 2011, 2011).
82. D. Pech *et al.*, Ultrahigh-power micrometre-sized supercapacitors based on onion-like carbon. *Nat Nano* **5**, 651 (2010).
83. J. W. Long, B. Dunn, D. R. Rolison, H. S. White, Three-dimensional battery architectures. *Chemical Reviews* **104**, 4463 (Oct, 2004).
84. F. Chamran, Y. Yeh, H. S. Min, B. Dunn, C. J. Kim, Fabrication of high-aspect-ratio electrode arrays for three-dimensional microbatteries. *J. Microelectromech. Syst.* **16**, 844 (Aug, 2007).
85. H. S. Min *et al.*, Fabrication and properties of a carbon/polypyrrole three-dimensional microbattery. *J. Power Sources* **178**, 795 (Apr, 2008).
86. M. Nathan *et al.*, Three-dimensional thin-film Li-ion microbatteries for autonomous MEMS. *J. Microelectromech. Syst.* **14**, 879 (Oct, 2005).
87. M. Kotobuki *et al.*, Effect of sol composition on solid electrode/solid electrolyte interface for all-solid-state lithium ion battery. *Electrochim. Acta* **56**, 1023 (2011).
88. P. H. L. Notten, F. Roozeboom, R. A. H. Niessen, L. Baggetto, 3-D Integrated All-Solid-State Rechargeable Batteries. *Advanced Materials* **19**, 4564 (2007).
89. K. Yoshima, H. Munakata, K. Kanamura, Fabrication of micro lithium-ion battery with 3D anode and 3D cathode by using polymer wall. *J. Power Sources* **208**, 404 (2012).
90. K. Sun *et al.*, 3D Printing of Interdigitated Li-Ion Microbattery Architectures. *Advanced Materials* **25**, 4539 (2013).
91. W. Lai *et al.*, Ultrahigh-Energy-Density Microbatteries Enabled by New Electrode Architecture and Micropackaging Design. *Advanced Materials* **22**, E139 (2010).
92. D. Golodnitsky *et al.*, Progress in three-dimensional (3D) Li-ion microbatteries. *Solid State Ionics* **177**, 2811 (Oct, 2006).
93. M. F. Ashby, The properties of foams and lattices. *Philosophical Transactions of the Royal Society A: Mathematical, Physical and Engineering Sciences* **364**, 15 (January 15, 2006, 2006).
94. L. J. Gibson, M. F. Ashby, *Cellular Solids : Structure and Properties*. (Cambridge University Press, Cambridge, ed. Second, 1997).
95. V. S. Deshpande, M. F. Ashby, N. A. Fleck, Foam topology: bending versus stretching dominated architectures. *Acta Materialia* **49**, 1035 (2001).
96. A. G. Evans, J. W. Hutchinson, M. F. Ashby, Cellular metals. *Curr. Opin. Solid State Mater. Sci.* **3**, 288 (1998).

97. V. S. Deshpande, N. A. Fleck, M. F. Ashby, Effective properties of the octet-truss lattice material. *Journal of the Mechanics and Physics of Solids* **49**, 1747 (2001).
98. N. A. Fleck, V. S. Deshpande, M. F. Ashby, *Micro-architectured materials: past, present and future*. (2010), vol. 466, pp. 2495-2516.
99. A. G. Evans, J. W. Hutchinson, N. A. Fleck, M. F. Ashby, H. N. G. Wadley, The topological design of multifunctional cellular metals. *Progress in Materials Science* **46**, 309 (2001).
100. A. A. Griffith, *The Phenomena of Rupture and Flow in Solids*. (1921), vol. 221, pp. 163-198.
101. E. O. Hall, The Deformation and Ageing of Mild Steel: III Discussion of Results. *Proceedings of the Physical Society. Section B* **64**, 747 (1951).
102. N. J. Petch, The Cleavage Strength of Polycrystals. *Journal of the Iron and Steel Institute* **174**, 25 (1953).
103. F. Ebrahimi, G. R. Bourne, M. S. Kelly, T. E. Matthews, Mechanical properties of nanocrystalline nickel produced by electrodeposition. *Nanostructured Materials* **11**, 343 (1999).
104. G. D. Hughes, S. D. Smith, C. S. Pande, H. R. Johnson, R. W. Armstrong, Hall-petch strengthening for the microhardness of twelve nanometer grain diameter electrodeposited nickel. *Scripta Metallurgica* **20**, 93 (1986).
105. A. M. El-Sherik, U. Erb, G. Palumbo, K. T. Aust, Deviations from hall-petch behaviour in as-prepared nanocrystalline nickel. *Scripta Metallurgica et Materialia* **27**, 1185 (1992).
106. J. R. Greer, J. T. M. De Hosson, Plasticity in small-sized metallic systems: Intrinsic versus extrinsic size effect. *Progress in Materials Science* **56**, 654 (2011).
107. M. D. Uchic, P. A. Shade, D. M. Dimiduk, Plasticity of Micrometer-Scale Single Crystals in Compression. *Annual Review of Materials Research* **39**, 361 (2009).
108. Z. Shan, R. K. Mishra, S. S. Asif, O. L. Warren, A. M. Minor, Mechanical annealing and source-limited deformation in submicrometre-diameter Ni crystals. *Nat. Mater.* **7**, 115 (2008).
109. J. R. Greer, W. C. Oliver, W. D. Nix, Size dependence of mechanical properties of gold at the micron scale in the absence of strain gradients. *Acta Materialia* **53**, 1821 (2005).
110. C. P. Frick, B. G. Clark, S. Orso, A. S. Schneider, E. Arzt, Size effect on strength and strain hardening of small-scale [1 1 1] nickel compression pillars. *Materials Science and Engineering: A* **489**, 319 (2008).
111. C. Volkert, E. Lilleodden, D. Kramer, J. Weissmuller, Approaching the theoretical strength in nanoporous Au. *Appl. Phys. Lett.* **89**, 061920 (2006).
112. L. R. Meza, S. Das, J. R. Greer, Strong, lightweight, and recoverable three-dimensional ceramic nanolattices. *Science* **345**, 1322 (September 12, 2014, 2014).
113. X. Wendy Gu, J. R. Greer, Ultra-strong architected Cu meso-lattices. *Extreme Mechanics Letters* **2**, 7 (2015).
114. J. Bauer, S. Hengsbach, I. Tesari, R. Schwaiger, O. Kraft, High-strength cellular ceramic composites with 3D microarchitecture. *Proceedings of the National Academy of Sciences*, (February 3, 2014, 2014).
115. J. Biener, A. M. Hodge, A. V. Hamza, L. M. Hsiung, J. H. Satcher, Nanoporous Au: A high yield strength material. *Journal of Applied Physics* **97**, 024301 (2005).
116. J.-H. Lee, L. Wang, M. C. Boyce, E. L. Thomas, Periodic Bicontinuous Composites for High Specific Energy Absorption. *Nano Letters* **12**, 4392 (2012/08/08, 2012).
117. X. Zheng *et al.*, Ultralight, ultrastiff mechanical metamaterials. *Science* **344**, 1373 (June 20, 2014, 2014).
118. D. Jang, L. R. Meza, F. Greer, J. R. Greer, Fabrication and deformation of three-dimensional hollow ceramic nanostructures. *Nat Mater* **12**, 893 (2013).
119. L. C. Montemayor, L. R. Meza, J. R. Greer, Design and Fabrication of Hollow Rigid Nanolattices via Two-Photon Lithography. *Adv. Eng. Mater.* **16**, 184 (2014).
120. T. A. Schaedler *et al.*, Ultralight Metallic Microlattices. *Science* **334**, 962 (November 18, 2011, 2011).

121. J. Biener, A. M. Hodge, A. V. Hamza, Microscopic failure behavior of nanoporous gold. *Appl. Phys. Lett.* **87**, 121908 (2005).
122. J. Biener *et al.*, Size Effects on the Mechanical Behavior of Nanoporous Au. *Nano Letters* **6**, 2379 (2006/10/01, 2006).
123. A. M. Hodge *et al.*, Scaling equation for yield strength of nanoporous open-cell foams. *Acta Materialia* **55**, 1343 (2007).
124. D. Lee *et al.*, Microfabrication and mechanical properties of nanoporous gold at the nanoscale. *Scripta Materialia* **56**, 437 (2007).
125. Z. Li *et al.*, Effects of pore size on the mechanical properties of three-dimensionally ordered macroporous nickel. *Materials & Design* **45**, 52 (2013).
126. J. J. do Rosário *et al.*, Self-Assembled Ultra High Strength, Ultra Stiff Mechanical Metamaterials Based on Inverse Opals. *Adv. Eng. Mater.*, n/a (2015).

CHAPTER 2

HIGH POWER MICROBATTERIES FROM INTERDIGITATED THREE DIMENSIONAL BICONTINUOUS MICROPOROUS ELECTRODES*

2.1 Introduction

For conventional lithium ion batteries, typical volumetric energy and power densities are around 10-60 μWh cm^{-2} μm and 1-100 μW cm^{-2} μm. It is possible to achieve higher power density, up to 1000 μW cm^{-2} μm^{-1}, by using porous battery electrodes that reduce ion diffusion through the active anode and cathode materials, as well as designs that reduce ion diffusion time in the electrolyte and decrease electrical resistance in the electrodes (*1-7*). Most publications on high power batteries focus on either anode or cathode half cells, and show improved power density at the expense of energy density. In principle, a battery architecture based on 3-D integrated porous microelectrodes could achieve high power density without sacrificing energy density, by combining small ion diffusion distances, large percentage of active material, and highly conductive electrodes. Such a microarchitecture could also enable miniature batteries suitable for microelectronics integration (*8*). Previous research on microbatteries has focused on achieving high areal energy density rather than volumetric energy density or volumetric power density, leading to 3D microbattery energy and power densities 0.01-7 μWh cm^{-2} μm^{-1} and 0.04-

---

* Content in this chapter was previously published by the author and reproduced with permission from (*9*).

3.5 μW cm^{-2} μm^{-1} (*10-14*). It has proven difficult for batteries of any size to achieve the high power of a supercapacitor, which can be fabricated at nearly any size and have power density larger than 4.0 mW cm^{-2} μm^{-1} (*15*, *16*). It is also challenging to integrate 3-D electrodes into a complete microbattery cell, owing to the difficulty of integrating 3-D elements of anode and cathode materials, along with the need to control materials uniformity and feature sizes across a range of lengths scales 10 nm – 1 mm. A number of 3-D half-cell electrode designs for microbatteries, consisting of only the anode or cathode, have been presented (*6*, *10*, *17-21*). There are however only a few publications reporting the performance of microbattery cells having fully integrated 3-D anodes and cathodes (*10-13*).

This chapter presents lithium ion microbatteries with power densities up to 7.4 mW cm^{-2} μm^{-1} and energy densities up to 15 μWh cm^{-2} μm^{-1}. These microbatteries meet or exceed the power densities of the best supercapacitors, while retaining comparable energy density (*16*, *22*, *23*). Compared to other 3-D microbatteries, these microbatteries have 2,000X greater power density and 2X greater energy density (*10-13*). The energy and power performance is made possible by the integration of hierarchical interdigitated 3-D bicontinuous nanoporous electrodes into a microbattery form factor.

2.2 Results and Discussion

Microbattery architecture

Figure 2.1 shows the microbattery cell architecture. The electrodes are a thin layer of nickel-tin (anode) or manganese dioxide (cathode) conformally coated onto interdigitated highly porous metallic scaffolds. The microarchitecture provides short electron and ion transport lengths in the electrolytically active material and electrolyte (yielding high power density) while

maintaining a high volume of active material (yielding high energy density) (*2, 24*). The active material thickness varies between 17 and 90 nm. The metallic scaffold has 330 or 500 nm diameter pores. The interdigitated electrodes have a width 30 μm and spacing 10 μm, and the full battery cell has a volume of about 0.03 mm^3. The architecture based on interdigitated porous electrodes allows control over the disparate length scales necessary for high power and overcomes the challenge of fabricating full cells on a single substrate by allowing independent electrodeposition of the active materials onto their respective metallic scaffolds, taking advantage of the anode and cathode electrical isolation. Figure 2.1a illustrates the fabrication advantage of electrodeposition. We designed 8 different batteries (A through H) with variations of pore size, active material thickness, and battery geometry. Table 2.1 shows the geometry and discharge parameters for batteries A through H. An effective cathode thickness was approximated for each cell by matching the performance to a diffusion simulation, assuming a constant lithium diffusivity of 2.2×10^{-13} cm^2 s^{-1}. The effective cathode capacity was then calculated using this active material thickness.

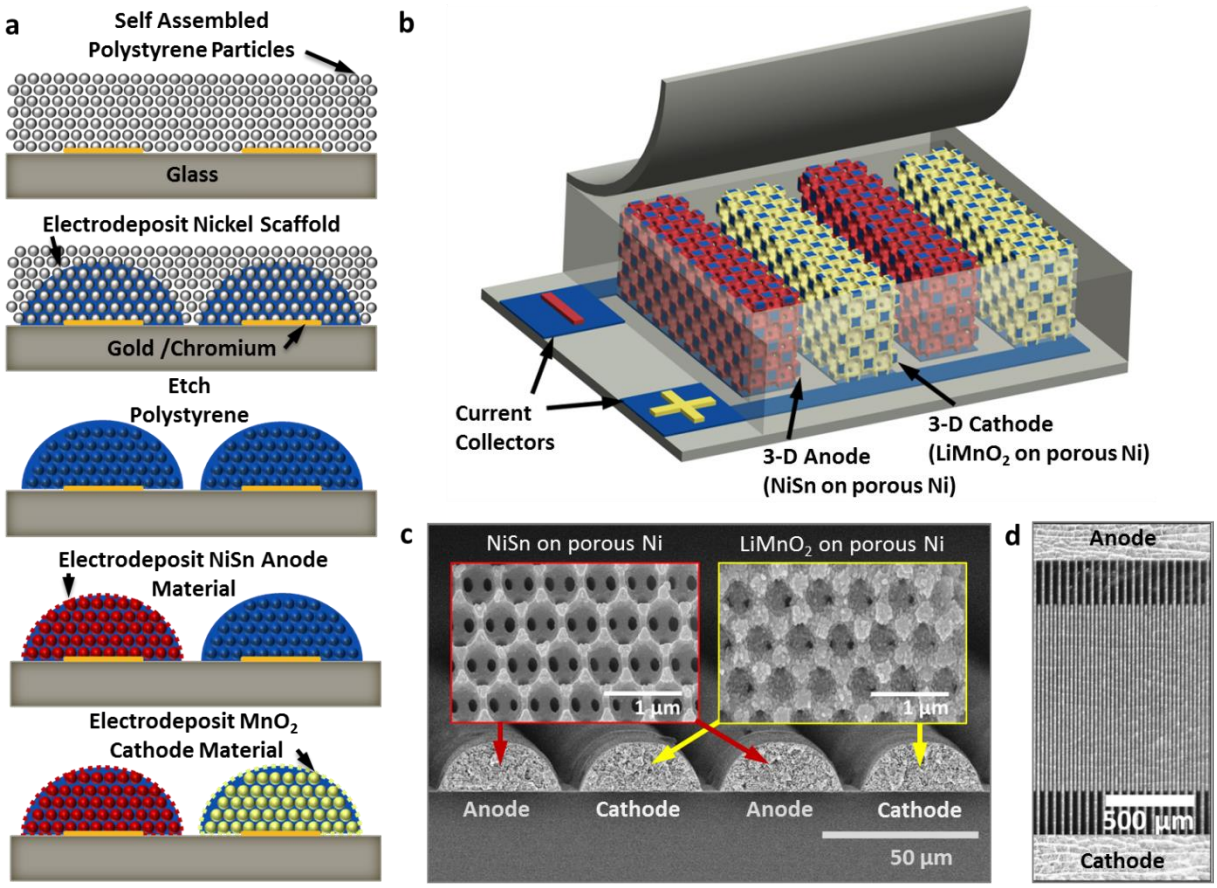

Figure 2.1: Microbattery fabrication and design. (**a**) Schematic of the fabrication process where the nickel scaffold defines the battery architecture and the active materials are electrodeposited onto the nickel scaffold for precise integration of the electrodes on a single substrate. (**b**) Microbattery design. The nanoporous microbattery electrodes consists of an electrolytically active layer (red and yellow) coated on an electrically conductive bicontinuous nickel scaffold (blue). The nickel scaffold acts the current collector attached to an outside circuit. A nickel-tin alloy is used as the anode (red), and lithiated manganese oxide as the cathode (yellow). (**c**) SEM cross section of the interdigitated electrodes spanning two periods. The interdigitated electrodes alternate between anode and cathode. The insets show the magnified electrodes with the nickel scaffold coated with nickel – tin on the left and lithiated manganese oxide on the right. Scale bars are 50 µm and 1 µm in the insets. (**d**) A top-down SEM image of the interdigitated electrodes with the anode electrodes connecting at the top, cathode electrodes connecting at the bottom, and the interdigitated anode and cathode electrodes overlapping in the middle. Scale bar is 500 µm.

Table 2.1: Cell geometry and discharge parameters for microbatteries A – H.

Battery	1 C Current (μA)	Footprint (mm^2)	Electrode Height (μm)	Pore Size (nm)	Effective Cathode Thickness (nm)	Effective Cathode Capacity ($mAh\ g^{-1}$)	Electrode Width (μm)	Electrode Pitch (μm)
A	1.7	2	14.9	500	60	120	33	45
B	0.7	1.7	12.6	500	28	185	28	45
C	0.6	1.5	9.9	500	67	70	22	27
D	1.5	3.5	15.2	500	28	130	40	50
E	0.5	1.9	14.9	500	37	70	33	45
F	0.5	1.8	14.7	330	34	40	38	45
G	0.25	1.6	14.9	500	22	70	33	45
H	0.5	4.6	11.7	330	17	50	30	45

Performance of the microbattery cells

Table 2.2 presents the volumetric energy and average power density of our microbattery cells and also lists the performance characteristics of 3D microbattery cells from the literature. The volume used for the calculations is the entire cell volume, including the volume occupied by the electrodes and between electrodes. At a 1.5 C discharge rate, our microbattery cell A has a 15 $\mu Wh\ cm^{-2}\ \mu m^{-1}$ energy density and 23 $\mu W\ cm^{-2}\ \mu m^{-1}$ power density, 2X the energy density and 6X the power density of the best published cells (*10-13*). At an 870 C discharge rate, microbattery cell B has a 0.6 $\mu Wh\ cm^{-2}\ \mu m^{-1}$ energy density and 7.4 $mW\ cm^{-2}\ \mu m^{-1}$ power density, a larger energy density than 3 of the 4 published cells and 2,000X the power density of the best published cell (*10-13*). Table 2.3 shows the energy and power density of microbattery cells A – H.

Table 2.2: Volumetric energy and power density of our microbattery cells and published 3D microbattery cells.

Battery	Chemistry	C Rate	Electrode Height (μm)	Energy Density ($\mu Wh\ cm^{-2}\ \mu m^{-1}$)	Power Density ($\mu W\ cm^{-2}\ \mu m^{-1}$)
MB1[10]	Carbon - PPYDBS	2.1	65	0.33	2.77
MB2[11]	MCMB – MoO_yS_z	Low	500	7.0	0.7
MB2[11]	MCMB – MoO_yS_z	High	500	2.31	3.5
MB3[12]	$LiCoO_2$ – $Li_4Mn_5O_{12}$		180	0.17	0.04
MB4[9]	Ni – Zn	16	200	0.01	0.17
A	**NiSn – LMO***	**1.5**	**15**	**15**	**23**
B	**NiSn – LMO***	**870**	**12.6**	**0.6**	**7,400**

Table 2.3: Volumetric energy and power density at the highest and lowest discharge rates for microbatteries A – H.

Battery	Low Rate		High Rate	
	Energy ($\mu Wh\ cm^{-2}\ \mu m^{-1}$)	Power ($\mu W\ cm^{-2}\ \mu m^{-1}$)	Energy ($\mu Wh\ cm^{-2}\ \mu m^{-1}$)	Power ($\mu Wh\ cm^{-2}\ \mu m^{-1}$)
A	15.0	22.9	0.01	5870
B	8.4	12.0	0.62	7360
C	10.9	4.7	0.08	4450
D	7.7	7.1	1.09	7260
E	4.7	4.6	0.19	4900
F	5.0	4.7	0.005	3920
G	2.9	2.7	0.39	2940
H	2.5	1.2	0.68	2420

Figure 2.2a shows the discharge data of microbattery cell H. At 1 C the battery is near steady state, since its energy is 96% of its energy at 0.5 C. At high discharge rates the cell retains a large percentage of its low rate energy, 28% at 965 C. Figures 2.3 show the discharge of cell H versus time. Figure 2.2b shows the normalized discharge capacity of microbattery cell H after 15

charge / discharge cycles. The microbattery cell retains 92% of its energy after 4 high rate discharges. The cell retains 64% of its initial energy after 15 cycles, loosing on average 5% of its energy after each low rate cycle. One reason for capacity fade may be the lithium capacity in the anode and cathode were not matched, such that the anode acted as a large ion source but reduced the number of transportable ions because of irreversible capacity loss from SEI formation after each cycle.

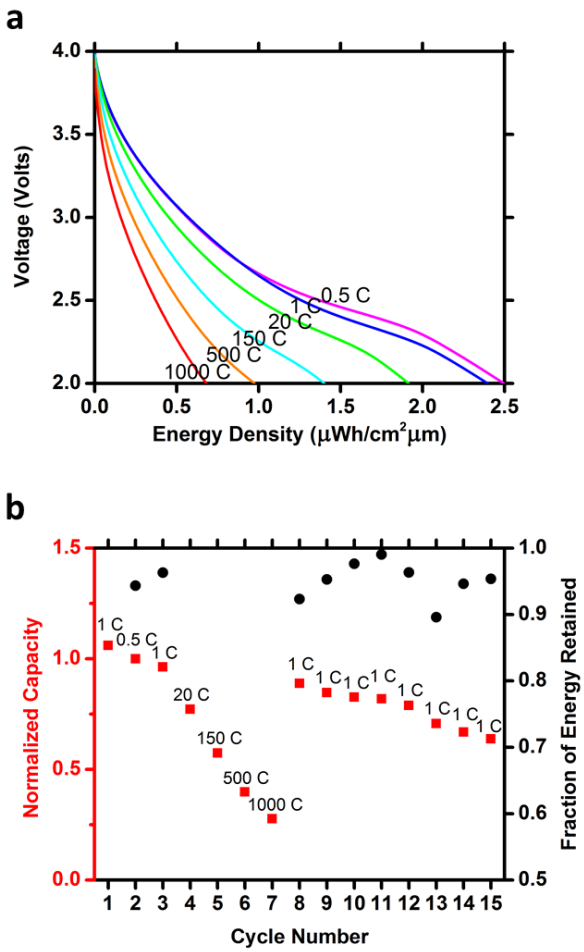

Figure 2.2: Electrochemical properties of the microbattery. (**a**) Discharge from microbattery cell H at C rates ranging 0.5 to 1000. (**b**) Capacity of microbattery cell H for the first 15 cycles at the noted C rate, normalized to the energy at 0.5 C. The secondary Y axis indicates the percentage of capacity retained in the given cycle when compared to the previous cycle (calculated for low C rate cycles only).

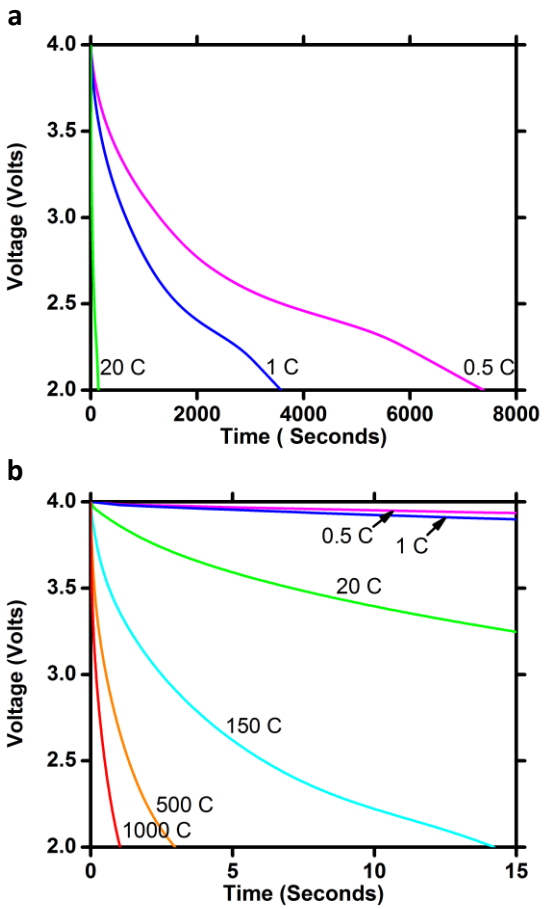

Figure 2.3: Discharge versus time of microbattery H at various C rates. (**b**) Discharge curves for the first 15 seconds of discharge.

Figure 2.4 presents a Ragone plot of the energy and power densities of microbattery cells presented here, along with conventional energy storage technologies including two commercial batteries. The energy densities of our microbattery cells at low rates vary from 2.5 to 15 μWh cm^{-2} μm^{-1}. At high rate (order 1000 C), our microbatteries have power densities up to 7400 μW cm^{-2} μm^{-1}. Compared to conventional supercapacitors, our microbattery delivers 10X the power of a supercapacitor at comparable energy density, delivers 10X the energy of a supercapacitor at comparable power density, or has 10X smaller volume than a supercapacitor at comparable performance. Figure 2.5 compares the volumetric energy and power density of our microbatteries

to the energy and power density of some of the most recent and highest performance supercapacitors, including two recently published in *Science (16, 22, 23, 25)*. The power densities of the microbatteries are equivalent to or exceed the power densities of most supercapacitors. Microbatteries B and D have higher power density than the power density reported by supercapacitors C1 – C4. The supercapacitors were discharged in the range of 4 to 0 volts, whereas microbatteries A – H output their power over a higher and more consistent range of 4 to 2 volts, which is important when integrating power management electronics with energy storage devices. Supercapacitor C5 has the highest power density of 13 mW cm^{-2} μm^{-1}, but achieves this with the lowest energy density of 0.1 μWh cm^{-2} μm^{-1}. There is a sharp cutoff in the maximum energy density of the supercapacitors, around 4.0 μWh cm^{-2} μm^{-1}. Six of our microbatteries can achieve a higher energy density than 4.0 μWh cm^{-2} μm^{-1}, with the maximum being 15 μWh cm^{-2} μm^{-1}, an almost 4X increase. The energy densities of the microbatteries are initially superior to the supercapcitors, but lose an average 5% total energy density after each cycle. Supercapacitors, however, are known for their ability to achieve up to 10,000 cycles without losing significant energy density (*25*). The volumetric energy and power density of supercapacitors C1, C4, and C5 were published and converted to the units used here, as well as adjusted to include the volume of just the electrodes, electrolytes, and separators where needed. The volumetric energy and power density of the active electrode material in supercapacitors C2 and C3 were determined by multiplying the specific energy and power of the carbon electrodes by the density of graphite, assumed 2.23 g cm^{-3}. The porosity of the electrodes were then determined using the total pore volume per gram of carbon, which was presented in each publication, and the final volumetric energy and power density was calculated by assuming each device has two electrodes and 10% separator volume.

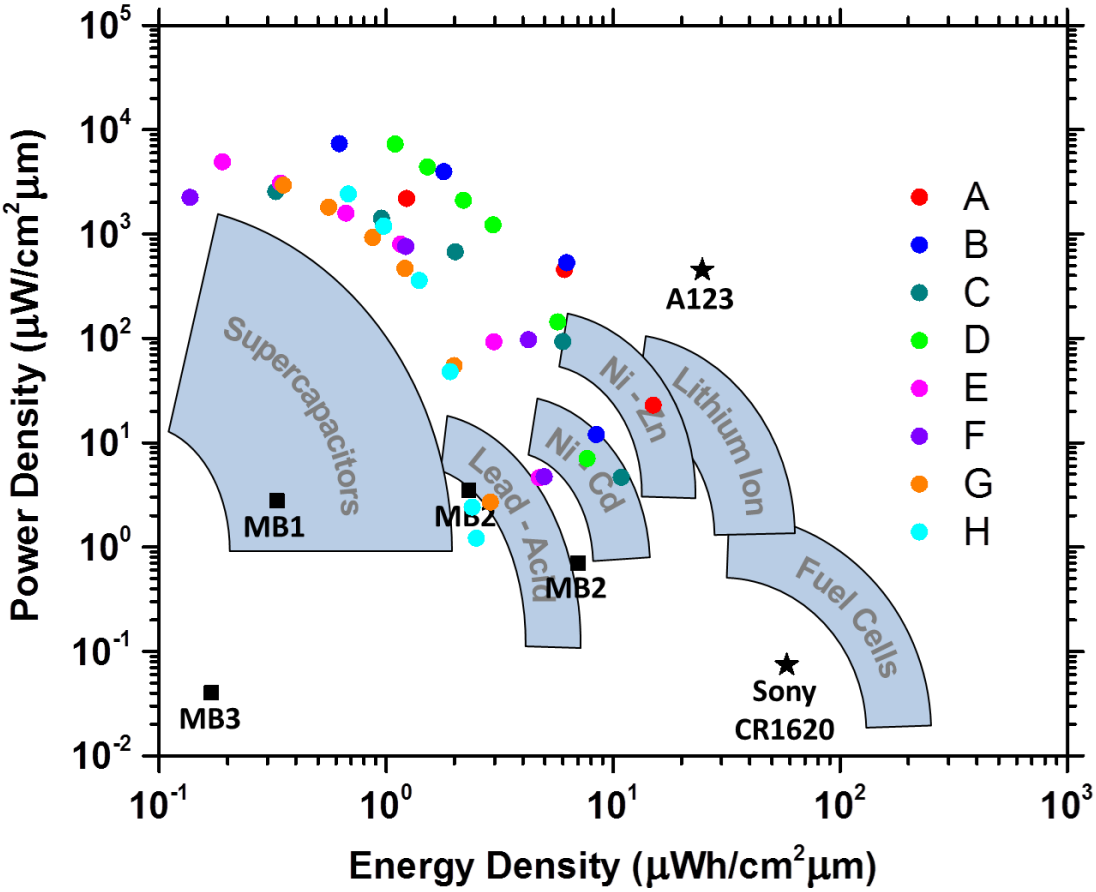

Figure 2.4: Ragone plot showing the performance of our microbattery cells and conventional power technologies. The energy and power density of our microbattery cells (A through H) at low to high C rates, along with previous microbattery cells having 3D electrodes (MB1 through MB3). The plot also includes the performance range of conventional power technologies and commercial batteries from A123 (high power) and Sony (high energy).

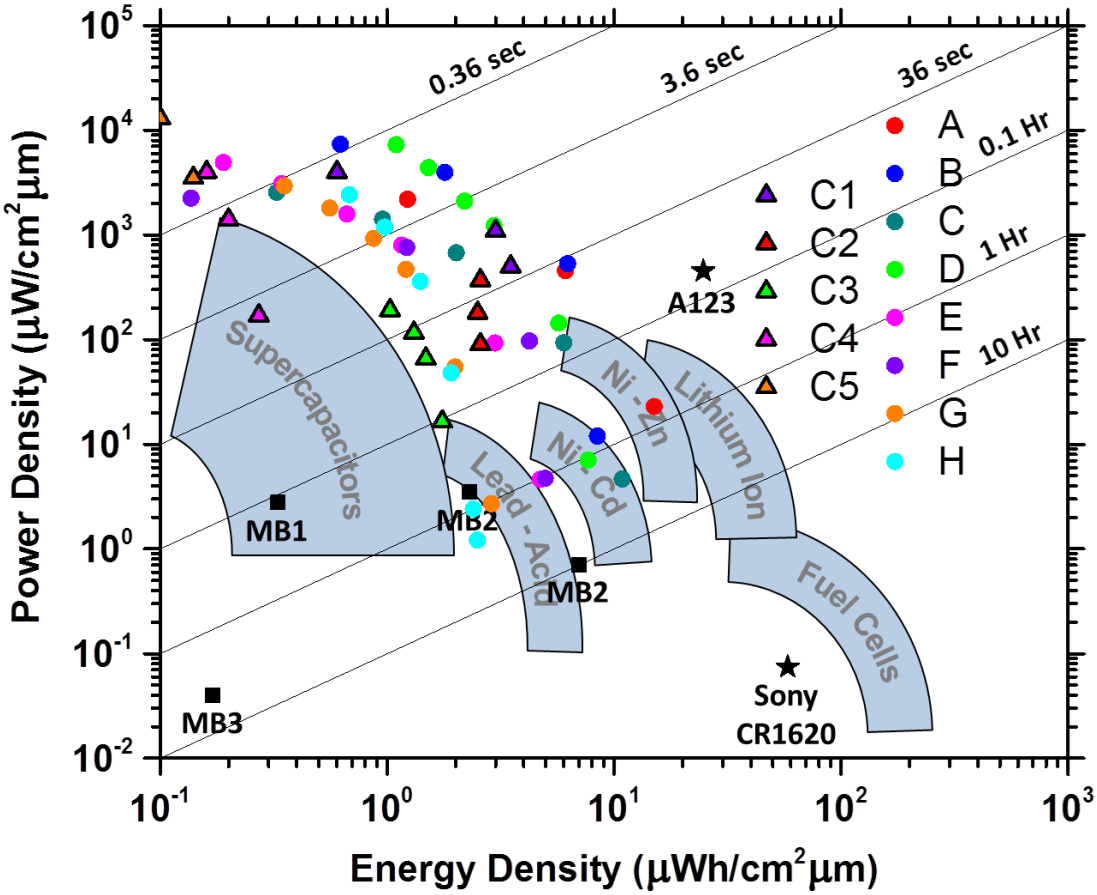

Figure 2.5: Ragone plot showing the performance of our microbatteries and select supercapacitors. The energy and power density of our microbattery cells (A through H) are shown along with high energy density and miniature supercapacitors (C1[15], C2[22], C3[21], C4[24], and C5[15] ENREF 4). The sloping lines on the Ragone plot show the approximate time to remove charge from the device. The plot also shows the performance range of conventional power source technologies, commercial batteries from A123 (high power) and Sony (high energy), and previous microbattery cells having 3D electrodes (MB1 through MB3).

2.3 Conclusion

The microbattery architecture reported here improves power density and enables microelectronics integration of lithium ion batteries. The high power density is achieved by simultaneously reducing ion diffusion lengths and electrical resistances across the entire microbattery system. The architecture allows compact integration of the anode and cathode on a

single substrate for microelectronics applications. This work illustrates how a micro-engineered architecture and materials integration can improve performance and enable the integration of miniature power sources, which have broad applications from medical implants to remote sensor networks. The batteries could be further improved by taller 3D electrodes, which would require improvements in the fabrication process. Additional research could explore the fundamentals of ion transport in this type of 3D battery, explore other battery chemistries, and explore routes to microelectronics packaging.

2.4 Methods

Nickel scaffold and microbattery architecture fabrication

We fabricated the fully integrated microbattery cells with anode, cathode, and liquid electrolyte by growing 3-D porous electrodes on electrically isolated, interdigitated metallic templates. Figure 2.6 illustrates the electrode fabrication. The bicontinuous nickel scaffold for the electrodes was fabricated by electrodepositing nickel through a polystyrene (PS) opal self-assembled on a glass substrate with interdigitated gold templates, and then removing the PS. The interdigitated gold templates for the microbattery electrodes were fabricated by sputtering 8 nm of chromium followed by 70 nm of gold on a 1 mm thick soda lime glass slide. The gold and chromium were then etched into 5 – 10 mm long interdigitated rectangles, called fingers, connected to two 4 mm wide contact pads such that every other finger was electrically connected and neighboring fingers were electrically isolated, making the templates for an interdigitated anode and cathode cell. Table 2.4 shows the finger area, width, and separation for the three templates used to test the influence of electrode width and spacing on the energy and power density. The glass slide with interdigitated gold templates was then diced into smaller

microbattery substrates, piranha cleaned for ten minutes, and then immersed in Millipore water with 2.2 % by weight 3-mercapto-1-propanesulfonic acid, sodium salt for 3 hours and rinsed to prepare them for PS opal growth. The substrates were positioned vertically in a colloid solution of 330 or 500 nm in diameter PS spheres and set on a hot plat at 55^{o} C, covered, and left for 24 to 30 hours until the solution was dry. During evaporation the spheres at the receding water-substrate meniscus are self-assembled onto the substrate into an opal, typically face centered cubic in structure. The substrates were then sintered at 96 °C for either 12 (opal made from 330 nm PS spheres) or 16 hours (opal made from 500 nm PS spheres), to increase the interconnect size between the PS spheres. The diameter of the interconnects could be made up to 58% of the pore diameter with sintering and electropolishing (*26*). The solution of PS spheres used to fabricate the opals was made by combining 1.2 grams of an 8 wt% PS sphere solution with 40 grams of Millipore water. The nickel for the anode and cathode 3-D scaffold was electrodeposited through the PS opal for about 20 minutes at a constant -2.0 volts versus a nickel reference electrode in commercial plating solution. The nickel grew both vertically and horizontally through the PS opal as it was plated. The typical width and height of the electrodes with template T1 was 33 µm wide and 15 µm tall. The nickel scaffold could be made up to 96.4% porous by maximizing the diameter of the interconnects and electropolishing the nickel after removal of the PS (*26*). The PS was removed by immersing the plated substrates in tetrahydrofuran for 5 hours followed by oxygen plasma etching at 400 mTorr for 10 minutes. The resulting nickel structure was a network of interconnecting pores, each pore adjoined by twelve others, which acted as a current collector and provided the scaffold for the microbattery electrodes. In the microbattery cells presented here the pore size of the nickel scaffold was 500 nm and 330 nm with 200 nm and 115 nm diameter interconnects, approximately 87% porous.

Table 2.4: Area, finger width, and finger separation for microbattery templates T1 – T3.

Templates	Area (mm x mm)	Finger width (µm)	Finger Separation (µm)
T1	3 x 35	5	40
T2	3 x 35	3	24
T3	5.5 x 35	10	40

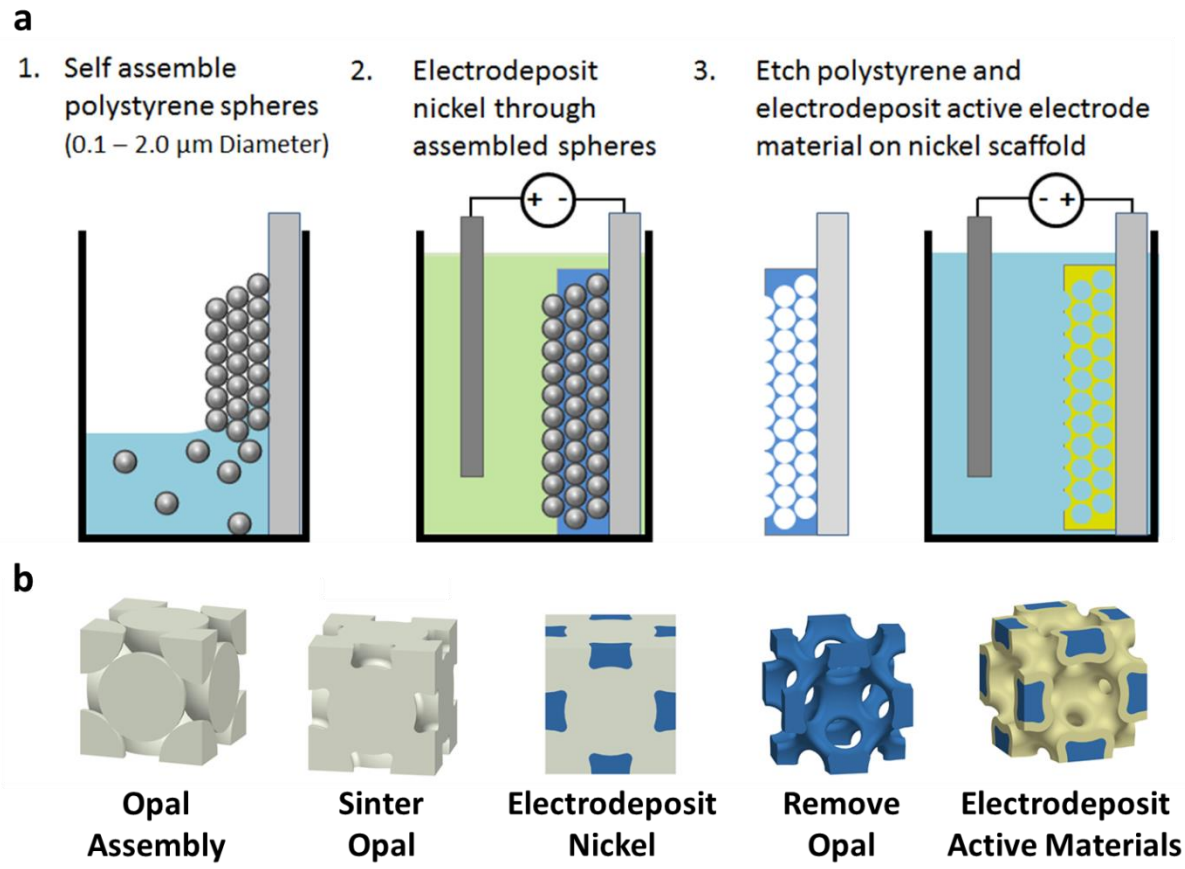

Figure 2.6: Fabrication of the electrodes. (**a**) A substrate with a conductive coating was immersed in a colloid solution of polystyrene spheres in water. During evaporation the spheres self-assembled onto the substrate into an opal assembly, typically face centered cubic in structure. The opal assembly was then sintered at 96 °C. Nickel was then electrodeposited through the voids of the opal assembly using a commercial nickel electroplating solution. After removing the polystyrene with a THF soak and O_2 plasma, the electrolytically active material was electrodeposited onto the nickel using a voltage controlled pulse signal. (**b**) Unit cells of the electrode structure throughout the fabrication process.

Anode and cathode electrodeposition

The anode and cathode electrolytic materials were sequentially electrodeposited on the nickel scaffold. Voltage controlled, pulsed electrodeposition was used to ensure conformal coating of the active materials throughout the 3-D structure. Figure 2.7 shows the process flow diagram for fabricating the full microbattery cells. A nickel – tin alloy was electrodeposited onto the nickel scaffold corresponding to the anode. MnOOH was then electrodeposited on the nickel scaffold corresponding to the cathode. The plating solution chemistries and voltage deposition profiles are detailed below:

MnOOH electrochemical deposition solution:

0.1 M manganese acetate tetrahydrate and 0.1 M sodium sulfate in Milli-Q water.

MnOOH pulsed voltage deposition profile:

1. Surface Preparation

    1.8 volts on for 0.15 seconds, 0 volts off for 4 seconds, cycled 60 – 80 times

2. Deposition

    1.8 volts on for 0.15 seconds, 1.1 volts off for 4 seconds, cycled 40 – 300 times

Ni-Sn electrochemical deposition solution:

100 ml Milli-Q water, 30 g $K_4P_2O_7$, 0.8 g $NiCl_2$, 0.8 g glycine, 0.8 g potassium sodium tartrate, 2.0 g $SnCl_2 \cdot 2H_2O$.

Ni-Sn pulsed voltage deposition profile:

-0.22 volts on for 0.6 seconds, 0 volts off for 3 seconds, cycled 15 – 30 times

After electrodeposition, the substrate was immersed in molten lithium salts, $LiNO_3$ and LiOH, at 300^o C for 30 minutes to form lithiated manganese oxide. Figure 2.1b shows cross section micrographs of the nickel – tin coated anode and lithiated manganese oxide coated

cathode. The materials were chosen because they could be conformally fabricated in 3-D. The thickness of the electrodeposited anode (30 – 90 nm) and cathode (17 – 67 nm) layers determine the solid state ion and electron transport lengths. The volume of active material varies from 14 to 45 % of the available electrode volume, depending on the active layer thickness and pore diameter. Figure 2.1d shows the interdigitated microelectrodes with fully integrated anodes and cathodes. The center to center distance between electrodes (27 – 50 μm) governs the ion transport length in the electrolyte.

Electrochemical testing of the microbattery

The microbattery substrate was covered with TorrSeal® after the electrode fabrication, except for the area to be tested. The anode and cathode were independently charged to 0.05 V and 4.0 V versus lithium metal in 1:1 ethylene carbonate (EC) and dimethyl carbonate (DMC) with 1 molar $LiClO_4$ liquid electrolyte. The microbattery cell was then capped with a sheet of silicone and tested by galvanostatically discharging the cells from 4 to 2 volts at various C rates. At a 1 C rate the cell discharges in one hour, and at a C rate of *N*, the cell discharges at *N* times the 1 C current.

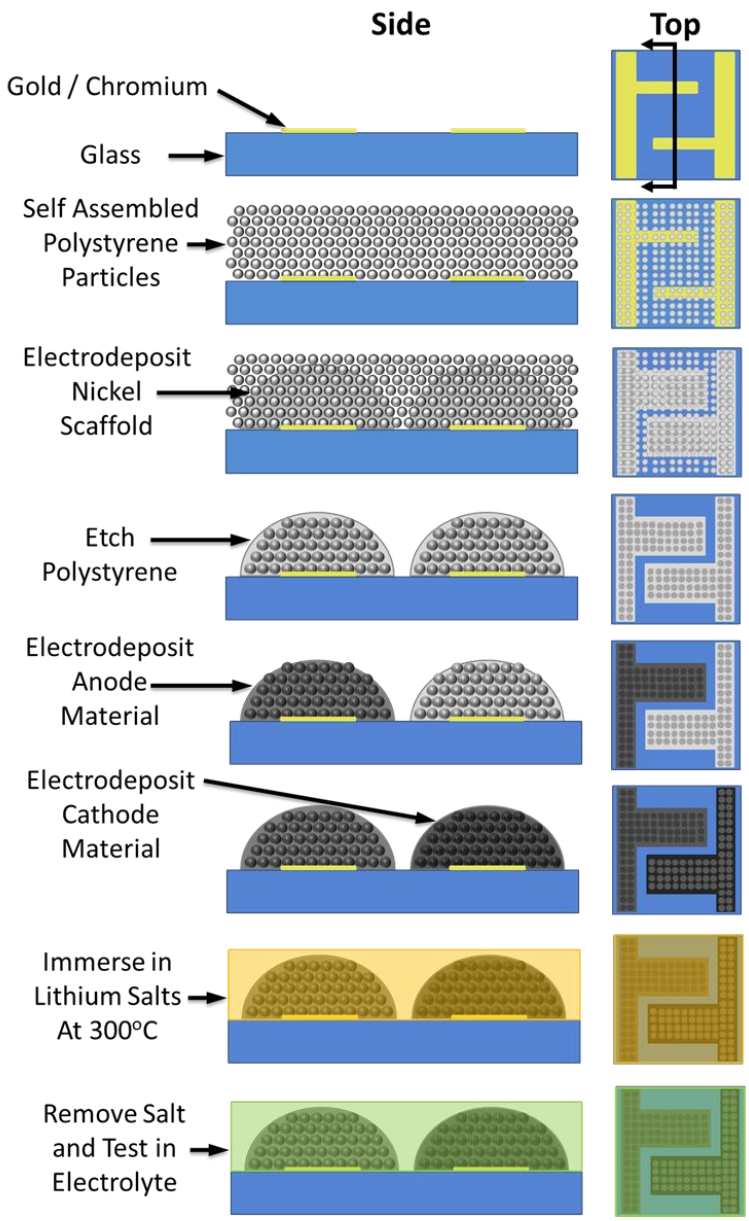

Figure 2.7: Fabrication of the interdigitated microbattery cells. The gold interdigitated electrode template was fabricated onto a 1 mm thick soda lime glass substrate using conventional lithography. The gold was functionalized with a 3-mercapto-1-propanesulfonic acid, sodium salt monolayer after which polystyrene colloids were assembled onto the substrate and the nickel scaffold was electrodeposited. The nickel grew horizontally and vertically during electrodeposition, thus the width of each electrode and the electrode spacing could be precisely controlled by adjusting the nickel deposition time. A nickel – tin alloy was then electrodeposited onto the nickel scaffold corresponding to the anode. MnOOH was then electrodeposited on the nickel scaffold corresponding to the cathode. Finally the substrate was immersed in molten lithium salts, $LiNO_3$ and LiOH, at 300^o C to form lithiated manganese oxide.

Microbattery cell characterization

The energy and power density of the microbattery cells were obtained by measuring the voltage and current during the cell discharge, calculating the total energy and power, and normalizing the energy and power to the volume of the microbattery cell. During the cell discharge the time (τ), voltage (V), and current (i) were recorded every second or for every 50 mV drop in cell voltage, whichever time is smaller. Each measurement corresponded to a time $d\tau$, during which a set number of Coulombs were discharged by the cell, $dq = i*d\tau$. The energy discharged at each time was calculated by the product of the voltage and dq. The total microbattery cell energy is the sum of the energy discharged at each $d\tau$ for the entire discharge time. The power of the microbattery at each time was calculated by the product of the cell voltage and current. The power density values presented are the average power density over the entire discharge. The microbattery cell volume includes the total volume occupied by the electrode (anode, cathode, Ni current collector, and electrolyte in the porous 3-D electrode) and the electrolyte in the separation between the electrodes. The volume was calculated by multiplying the height of the microbattery cell by the total area of the cell. The height of the microbattery electrodes was correlated to the width of the electrodes and thus could be calculated for the microbattery cell by measuring the average width of the electrodes in the cell. This allowed non-destructive height measurements of the microbattery cells. The ratio of electrode height to width was measured on sacrificial electrodes in an SEM. The height to width ratio was 0.45 for electrodes made with 500 nm PS spheres and 0.39 for the electrodes made with 330 nm PS spheres.

2.5 References

1. K. Brezesinski *et al.*, Ordered Mesoporous alpha-Fe_2O_3 (Hematite) Thin-Film Electrodes for Application in High Rate Rechargeable Lithium Batteries. *Small* **7**, 407 (Feb, 2011).
2. H. G. Zhang, X. D. Yu, P. V. Braun, Three-dimensional bicontinuous ultrafast-charge and -discharge bulk battery electrodes. *Nat. Nanotechnol.* **6**, 277 (May, 2011).
3. A. Esmanski, G. A. Ozin, Silicon Inverse-Opal-Based Macroporous Materials as Negative Electrodes for Lithium Ion Batteries. *Advanced Functional Materials* **19**, 1999 (2009).
4. N. S. Ergang *et al.*, Photonic Crystal Structures as a Basis for a Three-Dimensionally Interpenetrating Electrochemical-Cell System. *Advanced Materials* **18**, 1750 (2006).
5. J. S. Sakamoto, B. Dunn, Hierarchical battery electrodes based on inverted opal structures. *Journal of Materials Chemistry* **12**, 2859 (2002).
6. L. Taberna, S. Mitra, P. Poizot, P. Simon, J. M. Tarascon, High rate capabilities Fe_3O_4-based Cu nano-architectured electrodes for lithium-ion battery applications. *Nat. Mater.* **5**, 567 (2006).
7. M. Yao *et al.*, Nickel substrate having three-dimensional micronetwork structure for high-power nickel/metal-hydride battery. *Electrochemical and Solid State Letters* **10**, A56 (2007).
8. J. W. Long, B. Dunn, D. R. Rolison, H. S. White, Three-dimensional battery architectures. *Chemical Reviews* **104**, 4463 (Oct, 2004).
9. J. H. Pikul, H. Gang Zhang, J. Cho, P. V. Braun, W. P. King, High-power lithium ion microbatteries from interdigitated three-dimensional bicontinuous nanoporous electrodes. *Nat. Commun.* **4**, 1732 (2013).
10. F. Chamran, Y. Yeh, H. S. Min, B. Dunn, C. J. Kim, Fabrication of high-aspect-ratio electrode arrays for three-dimensional microbatteries. *J. Microelectromech. Syst.* **16**, 844 (Aug, 2007).
11. H. S. Min *et al.*, Fabrication and properties of a carbon/polypyrrole three-dimensional microbattery. *J. Power Sources* **178**, 795 (Apr, 2008).
12. M. Nathan *et al.*, Three-dimensional thin-film Li-ion microbatteries for autonomous MEMS. *J. Microelectromech. Syst.* **14**, 879 (Oct, 2005).
13. M. Kotobuki *et al.*, Effect of sol composition on solid electrode/solid electrolyte interface for all-solid-state lithium ion battery. *Electrochim. Acta* **56**, 1023 (2011).
14. P. H. L. Notten, F. Roozeboom, R. A. H. Niessen, L. Baggetto, 3-D Integrated All-Solid-State Rechargeable Batteries. *Advanced Materials* **19**, 4564 (2007).
15. J. Chmiola, C. Largeot, P.-L. Taberna, P. Simon, Y. Gogotsi, Monolithic Carbide-Derived Carbon Films for Micro-Supercapacitors. *Science* **328**, 480 (April 23, 2010, 2010).
16. D. Pech *et al.*, Ultrahigh-power micrometre-sized supercapacitors based on onion-like carbon. *Nat Nano* **5**, 651 (2010).
17. M. Nishizawa, K. Mukai, S. Kuwabata, C. R. Martin, H. Yoneyama, Template Synthesis of Polypyrrole-Coated Spinel $LiMn_2O_4$ Nanotubules and Their Properties as Cathode Active Materials for Lithium Batteries. *J. Electrochem. Soc.* **144**, 1923 (1997).
18. G. T. Teixidor, R. B. Zaouk, B. Y. Park, M. J. Madou, Fabrication and characterization of three-dimensional carbon electrodes for lithium-ion batteries. *J. Power Sources* **183**, 730 (2008).

19. N. Li, C. R. Martin, B. Scrosati, A High-Rate, High-Capacity, Nanostructured Tin Oxide Electrode. *Electrochemical and Solid-State Letters* **3**, 316 (2000).
20. M. M. Shaijumon *et al.*, Nanoarchitectured 3D Cathodes for Li-Ion Microbatteries. *Advanced Materials* **22**, 4978 (2010).
21. S. K. Cheah *et al.*, Self-Supported Three-Dimensional Nanoelectrodes for Microbattery Applications. *Nano Letters* **9**, 3230 (2009).
22. C. Liu, Z. Yu, D. Neff, A. Zhamu, B. Z. Jang, Graphene-Based Supercapacitor with an Ultrahigh Energy Density. *Nano Letters* **10**, 4863 (2010/12/08, 2010).
23. Y. Zhu *et al.*, Carbon-Based Supercapacitors Produced by Activation of Graphene. *Science* **332**, 1537 (June 24, 2011, 2011).
24. H. Zhang, P. V. Braun, Three-Dimensional Metal Scaffold Supported Bicontinuous Silicon Battery Anodes. *Nano Letters* **12**, 2778 (2012/06/13, 2012).
25. M. F. El-Kady, V. Strong, S. Dubin, R. B. Kaner, Laser Scribing of High-Performance and Flexible Graphene-Based Electrochemical Capacitors. *Science* **335**, 1326 (March 16, 2012, 2012).
26. X. Yu, Y. J. Lee, R. Furstenberg, J. O. White, P. V. Braun, Filling Fraction Dependent Properties of Inverse Opal Metallic Photonic Crystals. *Advanced Materials* **19**, 1689 (2007).

CHAPTER 3

PERFORMANCE MODELING AND DESIGN OF ULTRA HIGH POWER MICROBATTERIES

3.1 Introduction

High power density microbatteries would enable new capabilities for miniature sensors, radios, and industrial electronics (*1-4*). Recent improvements in electrode architectures, materials, and fabrication technologies have enabled microbatteries with power densities as high as 7.4 mW cm^{-2} μm^{-1}, which is about 100 times greater than power densities provided by larger conventional format batteries (*5-7*). The ultra-high power densities were achieved by the simultaneous reduction of ion and electron transport resistances across the anode, cathode, and electrolyte. Transport resistances are typically reduced by fabricating electrodes with increasingly fine nanostructures, which provide increasingly shorter ion and electron transport paths (*2, 5-16*). However, as the electrode dimensions decrease, electrode fabrication and incorporation of large volume fractions of high capacity materials into the nano architectures (important for obtaining high energy densities) becomes more difficult. Additionally, the larger surface area leads to increased SEI formation. To realize both high power and high energy density it is critically important to understand how battery architecture and materials affect the physical processes that limit power density and energy density, and to develop experimentally validated design rules that address the many engineering constraints in full battery assemblies.

Full-cell battery simulations have enabled design optimization of conventional batteries and better understanding of failure mechanisms, but the validity of the models has rarely been

explored above 25 C rate discharges (*17-25*), with only a few exceptions (*26-30*). No models have been validated for batteries discharged at the 100 – 1000 C rates demonstrated in high power microbatteries. The time it takes to discharge a battery in one hour is 1 C rate. An X C rate discharge corresponds to a current density X times the 1 C rate current density. An experimentally validated battery model that could characterize the physical processes that limit battery performance at high C rates would provide valuable physical and chemical metrics for future high power microbattery designs and fabrication.

In this chapter we present a 1-D electrochemical model that accurately simulates the power performance of batteries discharged at up to 600 C rates. The simulations were compared to high power interdigitated bicontinuous electrodes we previously reported (*5*). The model enables the study of local lithium concentration and overpotentials, which indicate that diffusion through the solid electrodes most limits the microbattery performance. Using the model, experimentally-validated design rules for high power batteries that optimize and characterize battery performance without the need for multiphysics based simulations are developed.

3.2 System Description and Modeling Approach

Figures 3.1a and b show a schematic and SEMs of the high power battery modeled in this work. The battery has interdigitated electrodes composed of a highly porous bicontinuous nickel current collector (blue) conformally coated with electrochemically active materials (active materials). The active material is nickel-tin (red) in the anode and lithiated manganese oxide (yellow) in the cathode. The electrolyte fills the volume between the electrodes and inside the electrode pores. Figure 3.1c shows a diagram of the lithium and electron transport paths during discharge. Lithium is stored at a high energy state in the anode. An oxidation reaction at the anode-electrolyte surface releases lithium ions and electrons which are transported to the lower

energy state cathode where they undergo reduction. Electrons cannot travel through the electrolyte and travel from the anode active material surface through the anode active material, anode current collector, external circuit where they power a load, cathode current collector and cathode active material until they react at the cathode surface (black). Lithium ions are transported from the anode to the cathode through the electrolyte (light blue). As lithium ions are released or inserted into the active material, lithium stored in the active material bulk diffuses to or away from the active material surface according to the concentration gradients (dark blue). Charging is the reverse process powered by an external device. The microbattery architecture simultaneously reduces the ion and electron transport lengths to achieve high power density.

The battery power performance depends on the battery voltage. Energy density is the product of the voltage and amount of charge transferred between electrodes per battery volume. Power density is the product of the voltage and charge transfer rate between electrodes per battery volume. The battery voltage is the electrochemical potential difference between anode and cathode minus any internal voltage drops. As the discharge current density increases, the electrochemical potential difference decreases and the internal voltage drops increase, so that the battery output voltage is reduced below its equilibrium value. The electrochemical potential difference is reduced because the lithium concentration at the active material surface is depleted or inserted faster than the lithium diffusion rate to the active material bulk. Internal voltage drops are due to the ohmic conduction of electrons through the electrodes, the ohmic conduction of ions across the electrolyte, and the electrochemical kinetics at the anode and cathode surface. At high discharge rates, the reduced output battery voltage from internal transport resistances causes the battery to reach a cut-off voltage before all of the energy can be fully extracted, which reduces power performance or amount of energy extracted at a given power density.

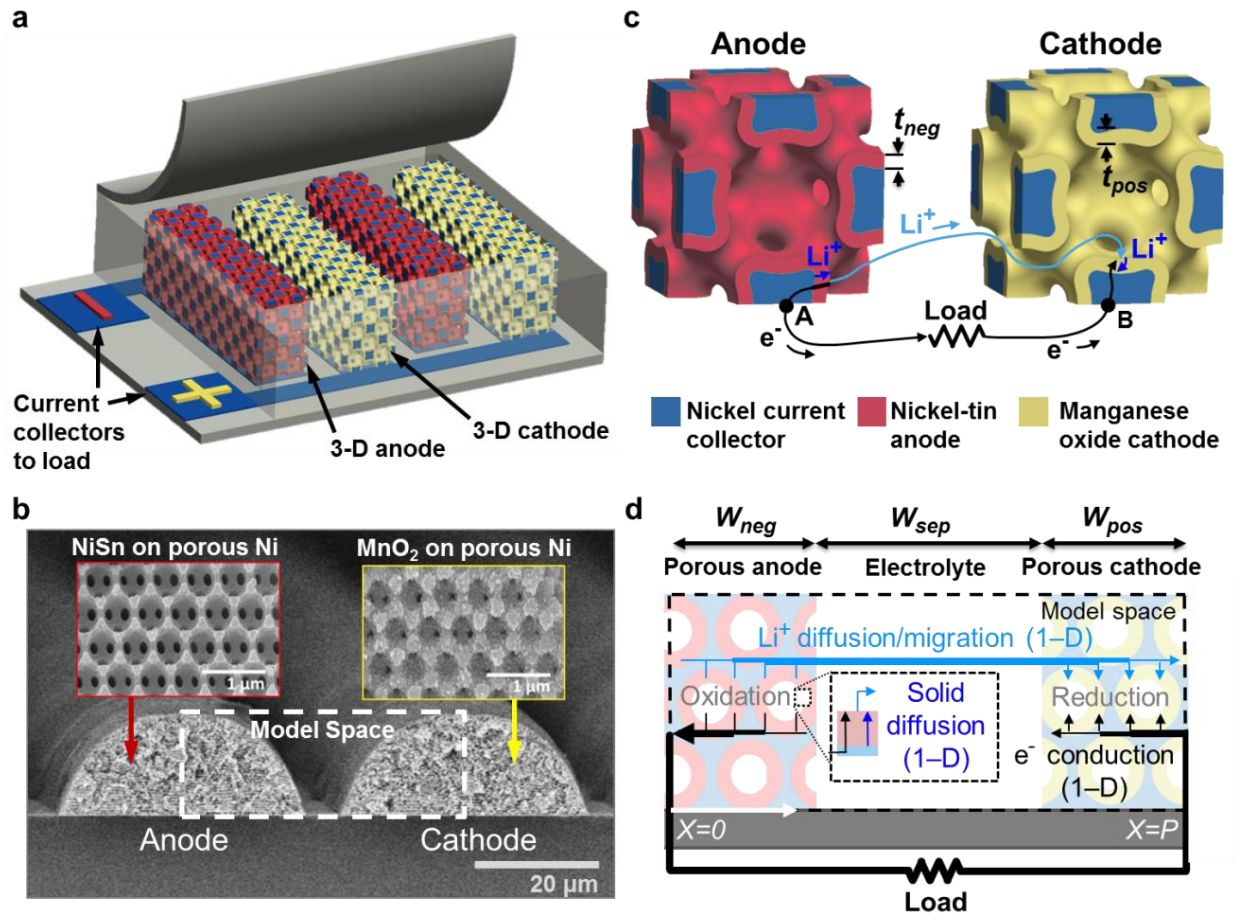

Figure 3.1: (**a**) A diagram of the simulated microbatteries with interdigitated electrodes that consist of an electrochemically active layer (red and yellow) coated on an electrically conductive porous bicontinuous nickel scaffold (blue). (**b**) Electron microscopy cross-section image of the interdigitated microbatteries. (**c**) A diagram depicting the important transport physics in unit cells of the lithium ion microbattery electrodes. (**d**) A schematic of the one dimensional model used to simulate the transport physics in the microbattery.

The power performance of the high power interdigitated bicontinuous microbattery is simulated using a 1-D ion and electron transport model that captures the major ion and electron transport physics (*17, 18*). Figure 1d shows the model space for the microbattery simulation, which is separated into the porous anode, porous cathode and separator. The model space simplifies the interdigitated electrode design to two electrodes bounded by the electrode

centerlines with a symmetric boundary condition. The electrodes are approximated as rectangular to enable the 1-D assumption. The effective electrode widths, W_{neg} and W_{pos}, are determined by calculating half the area of a circular segment that represents half the cross sectional area of the circular electrodes shown in fig. 3.1b, and dividing it by the electrode height, *H*. The lines in fig. 3.1d show the 1-D transport of ions and electrons. Transport through the electrolyte is governed by migration and diffusion using concentrated solution theory (*17, 18*). Electron transport is ohmic. The total current through each differential length, dx, of the battery is the sum of the current due to local conduction of electrons and ions and is constant across the entire pitch. The line thicknesses in fig. 3.1d represent the amount of current being transported by each process. At each differential length in the electrodes, there are separate models of 1-D diffusion through active material. The active material coating is approximated as a thin film with zero lithium flux to the nickel scaffold and flux at the electrode-electrolyte interface determined by Fick's law. The amount of lithium inserted or removed from the active material is determined by Butler-Volmer kinetics which link the electrolyte simulation to the electrochemical potential determined by the active material surface concentration. The model space and boundary conditions are chosen to match conventional battery formats so results can be generalized to other electrode architectures.

The nickel current collector volume fraction, ε_{Ni}, active material volume fraction, ε_{act}, and electrolyte volume fraction, ε_e, are important model inputs that determine the energy density of the batteries as well as impact the transport of ions and electrons. ε_{Ni}, ε_{act} and ε_e depend on the bicontinuous electrode structure and are calculated from a geometric model of self-assembled polystyrene (PS) spheres organized in a FCC unit cell. The current collector volume is the cubic unit cell volume minus the void volume left by the sintered PS spheres, V_{void}. The active material

volume, V_{act}, is the volume of a thin layer of thickness t subtracted from the surface of V_{void}. Figures 2a and 2b show a diagram of an inverse opal unit cell and the geometric model used to calculate the volume fractions. V_{act} and V_{void} are calculated from the simplified geometry of two neighboring spheres due to the FCC unit cell symmetry. The circles with radius R represent two PS spheres in contact after opal self-assembly with an initial 0.74 volume fraction expected for FCC packing. The PS volume increases after sintering and is calculated by increasing R to R_n such that neighboring radii overlap by a length b. V_{void} is the volume of 4 spheres of radii R_n minus the volume of 48 overlapping spherical caps of height h or

$$V_{void} = 4\,\frac{4}{3}\,\pi\,{R_n}^3 - 48\,\frac{1}{3}\,\pi\,h^2(3\,R_n - h), \tag{3.1}$$

where $R_n = \sqrt{(b/2)^2 - R^2}$ and h is R_n – R. V_{act} is the volume of the sphere of radius R_v subtracted from V_{void}. Additionally, the volume where the active material does not deposit, marked with hatching, is integrated and subtracted out, but not including the volume of the spherical cap marked by *h2*.

$$V_{act} = V_{void} - \,4\,\frac{4}{3}\,\pi\,(R_v)^3 - 48\int_0^{\frac{R_v R}{R_n}} \pi\,\left(\frac{b}{2} - \sqrt{t^2 - x^2}\right)^2\,dx + 48\frac{1}{3}\,\pi\,h2^2(3\,R_v - h2), \tag{3.2}$$

where *h2* is $R_v\,(1 - R\,/\,R_n)$. ε_{Ni}, ε_{act} and ε_e are then calculated from the V_{act} and V_{void} normalized by the unit cell volume , $\left(2\,R\,\sqrt{2}\right)^3$.

$$\varepsilon_{Ni} = 1 - \frac{V_{void}}{\left(2\,R\,\sqrt{2}\right)^3}, \tag{3.3}$$

$$\varepsilon_{act} = \frac{V_{act}}{\left(2\,R\,\sqrt{2}\right)^3}, \text{ and} \tag{3.4}$$

$$\varepsilon_e = \,1 - \varepsilon_{act} - \varepsilon_{Ni}. \tag{3.5}$$

Equations 3 – 5 calculate ε_{Ni}, ε_{act} and ε_e from fitting parameter t and experimental measurements of R and b. ε_{Ni} is 0.12 for the experimental batteries where b is 200 nm and R is 500 nm.

The composite nature of the bicontinuous electrode requires the calculation of an effective electrical conductivity, k^{eff}, that depends on ε_{Ni} and ε_{act}. Conductivity of the active material and nickel current collector, σ^{eff}, is approximated as conduction through the two media in parallel with their volume fractions normalized to 1, such that

$$\sigma^{eff} = \frac{\varepsilon_{Ni}}{\varepsilon_{Ni}+\varepsilon_{act}}\sigma_{Ni} + \frac{\varepsilon_{act}}{\varepsilon_{Ni}+\varepsilon_{act}}\sigma_{act}\,. \tag{3.6}$$

σ_{pos}^{eff} is 3.3×10^6 S m^{-1} and σ_{neg}^{eff} is 1.1×10^7 S m^{-1}. The voltage loss down the electrode length normal to the model space, L, is included in the 1-D model by correcting σ^{eff} to k^{eff}, where the conductance down the electrode length and width are the same,

$$\frac{k^{eff}LH}{W} = \frac{2\sigma^{eff}WH}{L}. \tag{3.7}$$

k^{eff} is then corrected for the porosity of the electrode with a Bruggeman exponent of 1.5.

The electrolyte material properties used in the model are based on available electrolyte data. 1:1 ethylene carbonate : dimethyl carbonate (EC:DMC) with initial concentration, c_e^0, of 1000 mol m^{-3} $LiClO_4$ is the electrolyte used in the experimental batteries. 2.6×10^{-10} m^2 s^{-1} is the approximate diffusivity based on 1 M $LiClO_4$ in propylene carbonate (PC) (*31*). The electrolyte conductivity depends on concentration and is taken from data on $LiClO_4$ in EC:PC (*32*), where the 8.5×10^{-3} S cm^{-1} maximum conductivity, σ_e, agrees well with 1 M $LiClO_4$ in EC:DMC (*33, 34*). The lithium transference number, t^+, is 0.363 based on $LiPF_6$ in EC:DMC because the transference number depends on the solvation radius of the anion, which is similar for PF_6^- and

ClO_4^- (*17, 33, 35*). The electrolyte conductivity and diffusivity through the porous electrodes is corrected for the increased path length using a Bruggeman exponent of 1.5 (*17, 18*).

The following are material properties used for the electrochemically active materials. Figure 3.3 shows the open circuit voltage (OCV), versus lithium, as a function of the state of charge for the anode and cathode active materials. The OCV is measured from batteries discharged at low rates. The maximum capacity of the cathode, c_{pos}^{max}, is 23,000 mol m^{-3} based on a 145 mAh g^{-1} manganese oxide cathode (*36*). The initial cathode concentration, c_{pos}^{0}, is approximated as 50 mol m^{-3} for all batteries. The nickel-tin anode is composed of 80% tin. At a full state of charge, the anode OCV corresponds to Li_3Sn and a 55,000 mol m^{-3} volumetric capacity (*37*). c_{neg}^{0} is set so that the low rate voltage plateau matches between simulation and experiment.

The material properties are combined with the electrode geometry and 1-D transport models and simulated in COMSOL using the 1-D battery module. The active material diffusivity, *D*, and thickness, *t*, are fitting parameters that match the experimental and simulated discharge curves and are bound by physical measurements in the battery architecture and materials. The maximum active material thickness is half the interconnect diameter between pores, or 100 nm. The diffusivities of the anode and cathode materials were measured using PITT. The anode diffusivities varied between 9.34×10^{-18} and 8.51×10^{-17} m^2 s^{-1}, with an average of 3.35×10^{-17} m^2 s^{-1}. The cathode diffusivities varied between 1.57×10^{-19} and 1.14×10^{-16} m^2 s^{-1}, with an average of 1.83×10^{-17} m^2 s^{-1}. The simulations use a constant diffusivity representing an average. Table 3.1 shows the thickness and diffusivity used to simulate each battery in addition to experimentally measured parameters. The anode and cathode diffusivities vary by a maximum of 3.35 and 3.66 X from the average measured diffusivities.

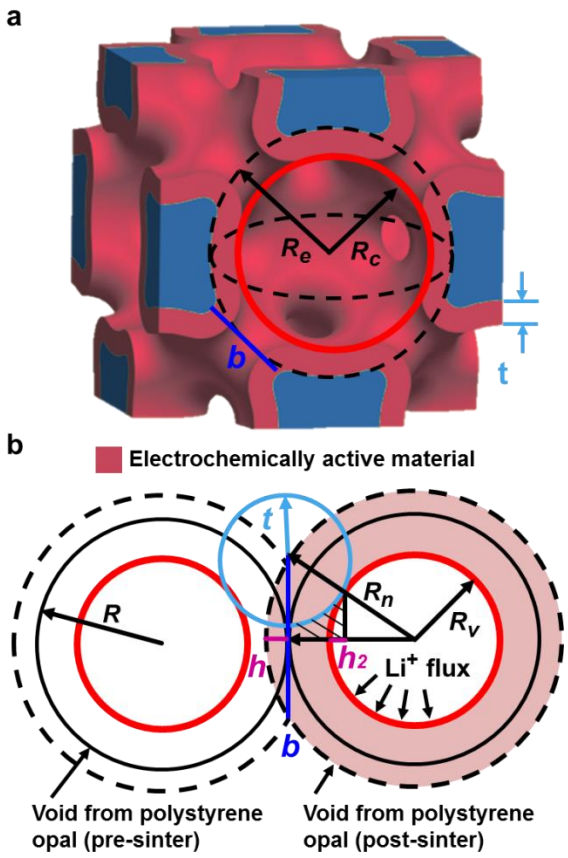

Figure 3.2: The geometric model used to characterize the electrode architecture. (**a**) A unit cell of the microbattery electrode with some geometric parameters. (**b**) The geometric model used to calculate the polystyrene radius, active material thickness, and volume fractions of the current collector and electrochemically active materials.

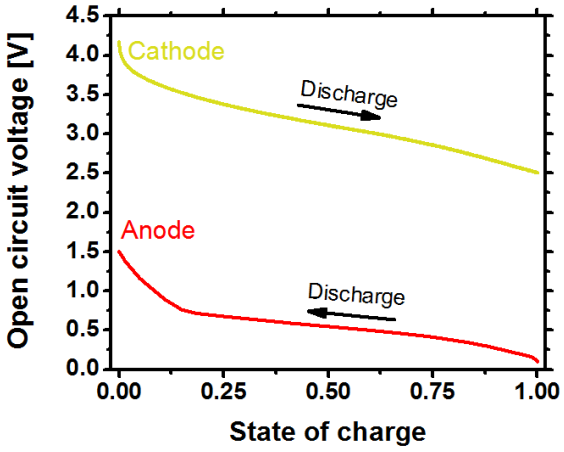

Figure 3.3: The equilibrium voltage profiles used for the anode and cathode materials in the simulation. Typically the anode starts at a SOC of 1 and the cathode at a SOC of 0.

Table 3.1: Parameters used for the simulation of batteries 1 through 5.

		Battery				
Parameter		1	2	3	4	5
D_{neg}	[m^2 s^{-1}]	3.0 X 10^{-17}	1.0 X 10^{-17}	3.0 X 10^{-17}	3.5 X 10^{-17}	4 X 10^{-17}
D_{pos}	[m^2 s^{-1}]	1.3 X 10^{-17}	5.0 X 10^{-18}	6.0 X 10^{-18}	3.9 X 10^{-17}	6.0 X 10^{-18}
t_{neg}	[nm]	30.0	17.0	30.0	21.0	27.0
t_{pos}	[nm]	55.0	37.0	20.0	29.5	13.3
c_{neg}^{0}	[mol m^{-3}]	54,500	54,500	21,000	54,500	15,700
H	[µm]	14.9	9.9	14.9	12.6	14.9
W_{neg}, W_{pos}	[µm]	12.6	8.4	12.6	10.7	12.6
P	[µm]	45	27	45	45	45

3.3 Modeling results

Figure 3.4 shows simulated and experimental discharge curves of batteries 1 – 4, which have the highest combined energy and power densities of the fabricated high power microbatteries (*5*). Figure 3.4a shows the discharge curves of battery 1. The experimental and simulated discharge curves directly overlap at low C rates. At 457 C the simulation predicts a larger capacity than measured; although, both simulation and experimental capacities are less than 5% of the total capacity. Figures 3.4b and 3.4c show the discharge curves of batteries 2 and 3. The simulation and experimental discharge curves for both batteries closely overlap at low and high discharge rates. At moderate discharges of 8.6 and 20 C the simulation predicts a higher capacity than measured experimentally. In battery 3, the experimental discharge voltage is higher than the simulated voltage during the first 0.15 Ah m^{-2}. Figure 3.4d shows the discharge curves for battery 4. The experimental and simulated discharges are similar except after 1.0 Ah m^{-2} at

1.42 C, where the experimental discharge has a more flat curve giving it extra capacity. Overall, the simulated discharge of all four batteries agrees well with the experimental data. Differences between the simulation and experiment are primarily due to experimental irregularities. The difference in the shape of the simulated and experimental discharge curves in battery 4 at low current density is due to the low temperature processing of the active materials, which allows for multiple active material phases with different shaped OCV curves. The lower average voltage of the discharge curves in battery 3 indicates that the anode was not fully charged before cycling, which caused to cathode to be overcharged when the battery was charged to a 4.0 volt cut-off. The overcharging caused a higher voltage for the first 0.15 Ah m^2 of experimental discharge. The higher simulated capacities at moderate rates for batteries 2 and 3 are likely due to error in the thin film approximation as the amount of capacity extracted from a thin film is larger than concave geometries at moderate discharge rates. The overall good agreement between simulation and experiment indicates that the model captures the major physics for high rate discharging and that the 1-D transport model provides an accurate foundation for design studies. The simulation accuracy could be improved by accounting for material property changes, including capacitive transport, and accounting for pore wall or surface film mass transport limitations.

The battery model simulates the concentration of lithium throughout the battery and can be used to probe the physics that limit battery performance. Figure 3.5a shows the electrolyte concentration in battery 1 at the end of discharge at multiple C rates. The change in electrolyte concentration increases as the C rate increases, except at 457 C, where the concentration change is less than that at 146 C. The maximum concentration change is 250 mol m^{-3} at 146 C. The concentration in the electrolyte is lower at 457 C than 146 C because the battery quickly shuts off at 457 C before a significant amount of ions can be removed from the electrolyte. This quick

shut off is due to limits in the solid active material diffusion and will be discussed later. The 250 mol m^{-3} maximum change in concentration changes the electrolyte conductivity from 8.6×10^{-3} S cm^{-1} to 8.2×10^{-3} S cm^{-1} in the cathode region and 8.5×10^{-3} S cm^{-1} in the anode region, which is insignificant and shows that conductivity, and also diffusion, in the electrolyte is not limiting the power performance of battery 1. Figure 3.5b shows the final lithium concentrations at the surface and center of the electrode active materials in battery 1. The center and surface concentrations are similar at low discharge rates. At high rates, the concentrations at the center of the electrodes are near the initial concentration; whereas, the cathode surface concentration approaches the maximum. Figure 3.5c shows a detailed concentration profile across the cathode thickness at each discharge rate. The concentration at the surface and center of the cathode is 22,200 mol m^{-3} and 2,600 mol m^{-3} at 30.5 C, which corresponds to a 1.26 volt difference or 63% of the battery voltage window. At 457 C the cathode surface concentration reaches a maximum in 0.17 seconds and limits the capacity to 0.058 Ah m^{-2}. The large concentration difference across the anode and cathode active materials and the associated overpotential at moderate and high discharge rates indicates that diffusion in the active material limits the power performance. Diffusive limitations in the active materials limit the power performance of all simulated batteries.

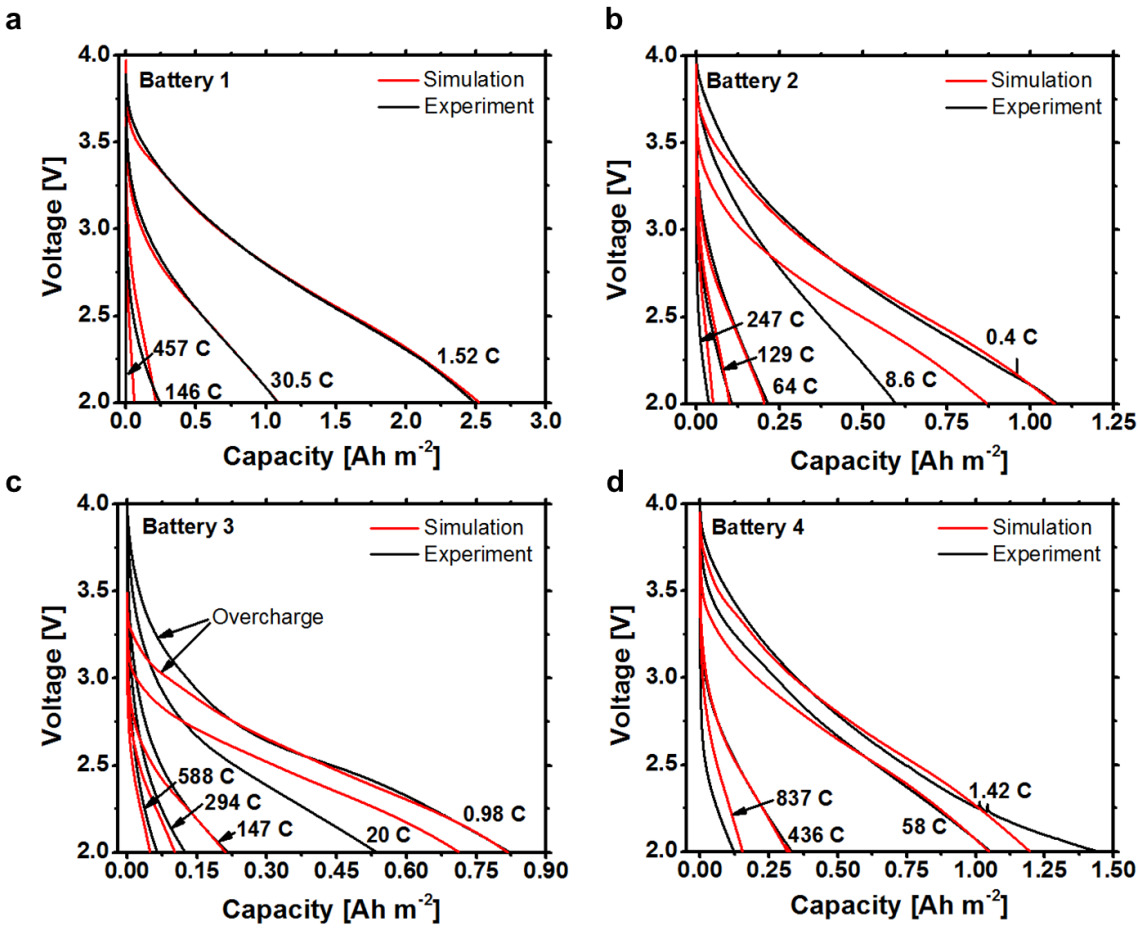

Figure 3.4: Comparison of simulation and experimental discharge curves in microbatteries 1 through 4. The capacity is normalized by the separator area.

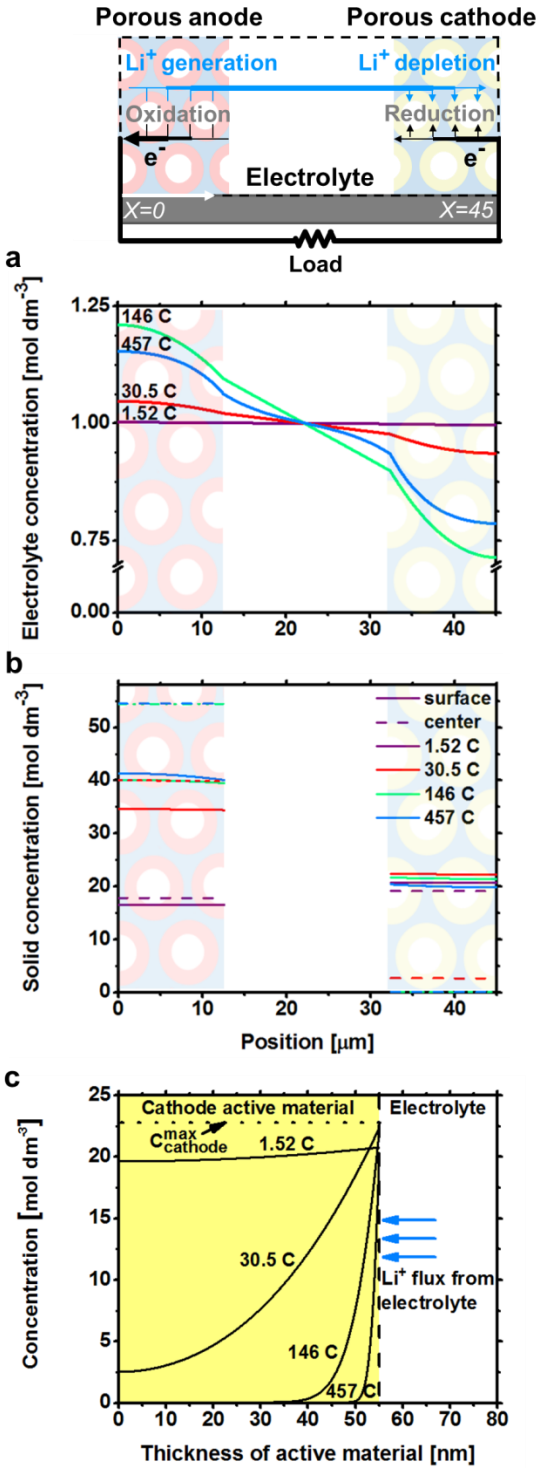

Figure 3.5: (**a** – **b**) Concentration of lithium in the electrolyte and solid active material at the end of discharge for battery 1 at various discharge rates. (**c**) Detailed concentration of lithium across the cathode active material thickness for battery 1 at various discharge rates.

3.4 Design and optimization considerations

The battery model developed in the previous section allows exploration of the physical processes that limit power performance. In this section, a set of design rules that characterize and optimize the battery performance are developed. Power performance, or energy density extracted at a power density, is the metric used for the design process. Power performance better informs the use case for high power batteries than power density alone. Volumetric energy density is used to characterize the power performance due to its technological relevance to microbatteries and because high power density is achievable with high gravimetric energy density materials that are thin and have low mass loading; however, low mass loading is technologically uninteresting for most applications. This holds true for supercapacitors. High power performance can be achieved by reducing internal transport resistances without sacrificing volumetric energy density. The design process presented here informs how engineering parameters influence the trade-offs between energy and power density, and develops design parameters that guide these trade-offs.

Engineering parameters are geometric parameters that can be controlled by electrode architecture and fabrication, and whose characteristic dimensions govern a transport process in the 1-D model. Figure 3.6 shows the engineering parameters explored in this study. Figure 3.6a shows the electrode width, W, and electrode pitch, P. The electrode width governs diffusion through the electrolyte because the largest concentration gradients, and thus the most significant ionic diffusion, in the electrolyte occur from depletion and generation of lithium ions in the electrode regions. The electrode pitch governs ionic conduction in the electrolyte. Figure 3.6b shows the active material thickness, t, which is the engineering parameter for diffusion in the active material. In other electrode designs the particle radius could function as the thickness. Multiple parameters govern electron conduction through the electrode as conduction occurs

along the width and length of the electrodes, in addition to across multiple materials in series and parallel. The electron conduction path in this work is controlled primarily by the bicontinuous electrode architecture shown in fig. 3.6b as well as the electrode length shown in fig. 3.6c.

The dominant effect each engineering parameter has on the power performance can be isolated by simulating the energy density output at various C rates for a range of values of a single engineering parameter or governing transport property. Design rules that relate the battery geometric and material properties to the power performance are then developed for each engineering parameter. Each engineering parameter is studied sequentially.

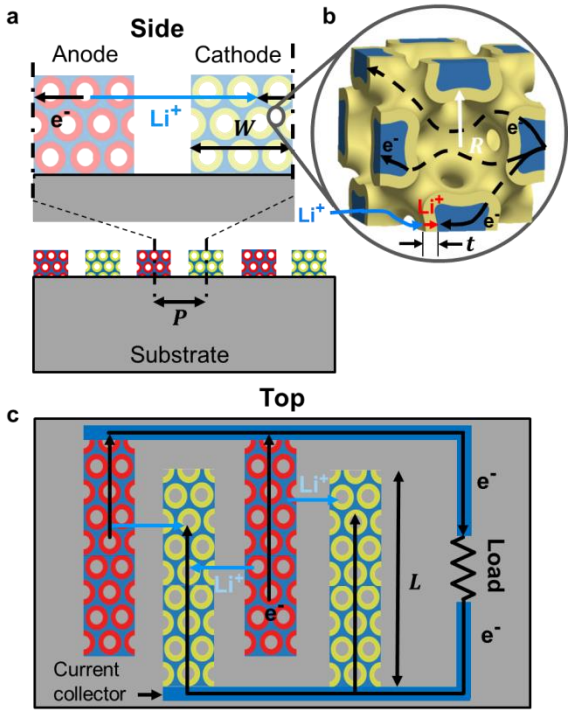

Figure 3.6: Diagrams of the microbattery electrodes depicting important engineering parameters. (**a**) Cross-section diagrams of the microbattery showing the electrode width, *W*, and electrode pitch, *P*. The electrode width is defined as half the physical width of the interdigitated electrodes due to symmetric boundary conditions. (**b**) A diagram of the microbattery electrode architecture depicting the electrode pore size and active material thickness, as well as electron transport through the bicontinuous nickel scaffold. (**c**) A diagram of the microbattery top showing the interdigitated layout and the electrode length, *L*.

Electrode width (W)

Figure 3.7a shows the simulated energy and power density of battery 1 when the electrode width and electrolyte diffusivity are varied. 5, 12.6 and 50 μm wide electrodes are simulated with the diffusivity scaled by factor of 0.04, 0.2, 1, 5, and 25 X from the value in table 3.1 for each electrode width. Simulations with the same electrode width are plotted in the same color. The primary feature in fig. 3.7a is a concavity in the Ragone curves for batteries with wide electrodes and low electrolyte diffusivities. The concave regions have bad power performance and are the result of lithium ions severely depleting in the cathode region so that the concentration in the electrolyte near the electrode centerline is near zero. The low concentration reduces the local electrolyte conductivity and causes a large voltage to develop across the electrolyte, which brings the battery to the shut off voltage before more energy can be extracted. The Ragone curves return to normal at higher C rates because diffusion in the active material causes the battery to shutoff before severe electrolyte depletion occurs. Figure 3.7a shows that the diffusion in the electrolyte has a minimal effect on the battery performance unless the concentration in the cathode region depletes to near zero, at which point the effect is dramatic.

The cathode width corresponding to complete depletion of electrolyte at a C rate discharge current can be predicted by solving for steady state diffusion in the cathode electrolyte region. The governing equation for 1-D diffusion in the electrolyte with constant and uniform depletion is

$$D\frac{\partial^2 c}{\partial x^2} + \dot{q} = 0. \tag{3.8}$$

The depletion rate in the electrolyte, $\dot{q}$, is assumed constant when discharged at a constant C rate and uniformly distributed throughout the electrode region. $\dot{q}$ is the amount of lithium ions that enter the cathode from the electrolyte per electrode volume, or

$$\dot{q} = -\left(c_{pos}^{max} - c_{pos}^{0}\right) \varepsilon_{pos} \frac{Crate}{3600}, \tag{3.9}$$

which is valid when the capacity in the battery electrodes are balanced, or when the cathode limits capacity. The discharge time is approximated as the time it takes to fully discharge a battery at a constant current density and is equivalent to 3600 seconds in and hour divided by the C rate, which is the inverse of the discharge time in hours. Solving equation 3.8 yields the concentration profile

$$c = -\frac{\dot{q}\, x^2}{2\, D_e\, {\varepsilon_e}^{1.5}} + Ax + B, \tag{3.10}$$

where x is the distance between the separator, $x = 0$, and the electrode centerline, $x = W_{pos}$. The diffusivity is corrected using the Bruggeman approximation. B is the electrolyte concentration at $x = 0$, which is assumed to be the initial concentration of the electrolyte, c_e^0, and is valid for most batteries because the concentration change across the separator is small. A is solved by setting the electrolyte flux at $x = W_{pos}$ to zero due to the symmetric boundary condition,

$$A = \frac{\dot{q}\, W_{pos}}{D_e\, {\varepsilon_e}^{1.5}}. \tag{3.11}$$

Equation 3.10 is used to solve the critical electrode width where the steady state electrolyte concentration depletes to zero, W_c, by setting $x = W_c = W_{pos}$ when $c = 0$. W_c is then

$$W_c = \sqrt{\frac{-2\, c_e^0\, D_e\, {\varepsilon_e}^{1.5}}{\dot{q}}}\,. \tag{3.12}$$

Figure 3.7b shows the simulated energy densities of battery 1 discharged at multiple C rates with electrode widths varied between 3 – 100 µm and a constant 19.8 µm W_{sep}. A maximum energy density occurs for each C rate. The dashed line shows the energy density of batteries with electrodes set to W_c using equation 12. The energy density at 12, 20 and 30.5 C dramatically decreases after the maximum energy density is reached because the concentration of lithium is depleted to near zero in the cathode electrolyte. The maximum energy density at each

C rate occurs due to competition between the geometric increases in electrode volume fraction that improve energy density (W/P) and the difficulty of ions diffusing through the increased electrode width. W_c does a good job of approximating the cathode width where the energy density starts to decrease due to ion depletion. W_c is therefore a good design parameter for the cathode width as it approximates the largest allowable cathode electrode width before severe ion depletion occurs.

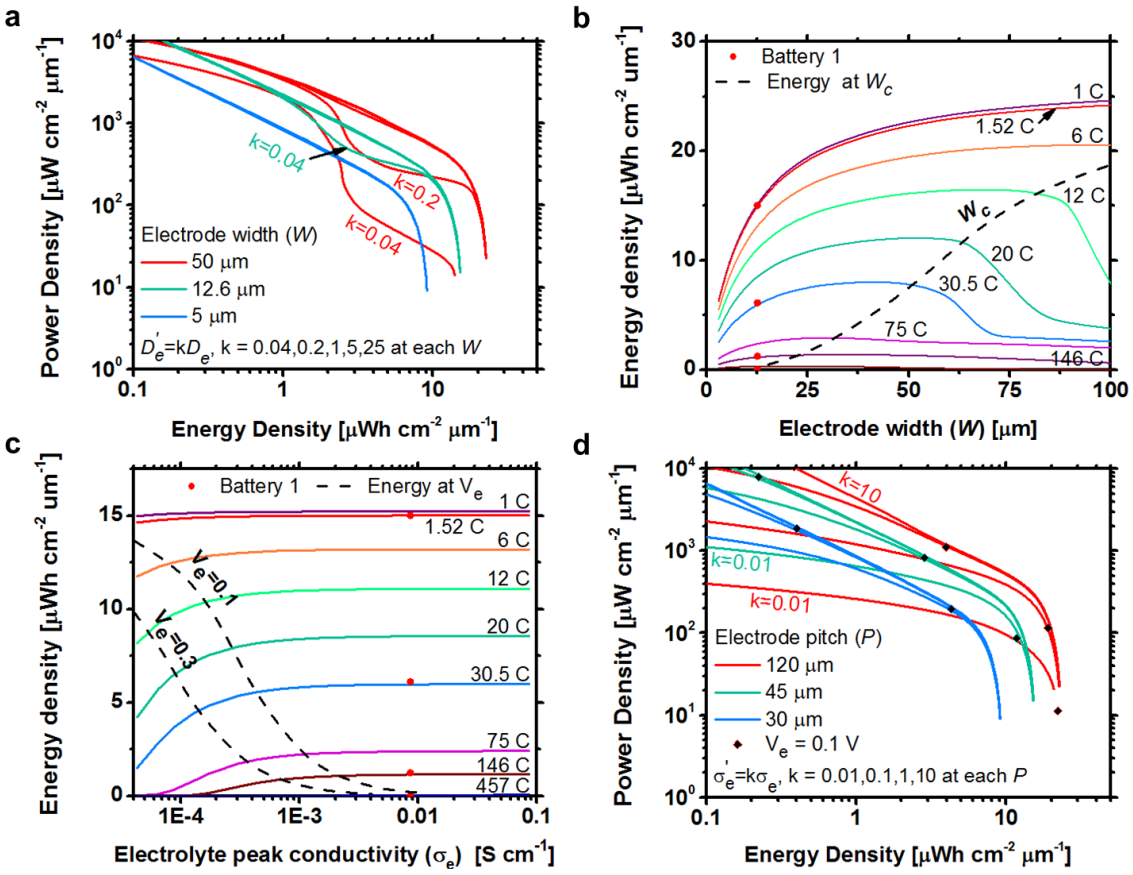

Figure 3.7: (**a**) Ragone plot of battery 1 as the diffusivity is varied by 0.04, 0.2, 1, and 10 in batteries with 5, 12.6, and 50 μm wide electrodes. (**b**) Simulated energy density versus electrode width for battery 1 at 1 to 146 C rate discharges. The dashed line is the design parameter, W_c, for the electrode width, which corresponds to the complete depletion of lithium ions at the cathode centerline for each C rate. (**c**) Simulated energy density versus electrolyte peak conductivity for battery 1 at 1 to 457 C rate discharges. The dashed lines are the design parameter, V_e, for the electrode pitch calculated with 0.1 and 0.3 voltage drops across the electrolyte for each C rate. (**d**) Ragone plot of battery 1 showing the effect of a change in electrolyte conductivity by 0.01,

0.1, 1, and 10 for each electrode pitch. The red dots are experimental data from battery 1. Black diamonds correspond to inflection points calculated from design parameters.

Electrode pitch (P)

Electrolyte conductivity is used as the independent variable to study the effect of the pitch on power performance because conductivity can be varied over many orders of magnitude without affecting other physics in the system. The pitch and conductivity are related through the conductance. Figure 3.7c shows the simulated energy density of battery 1 discharged at 1 – 500 C rates with electrolyte conductivities varied between 4×10^{-5} S cm^{-1} and 1×10^{-1} S cm^{-1}. Figure 3.7c shows that the energy density remains constant at each C rate as the conductivity decreases until the voltage drop in the electrolyte is greater than 0.1 volts, as shown by the dashed lines that represent a constant potential drop across the electrolyte. For a potential drop of 0.3 volts the energy density is further reduced. The voltage drop across the electrolyte is estimated from Ohm's law assuming that the electrolyte concentration does not vary significantly during discharge, which is valid if $W_{pos} < W_c$. The electrolyte conductivity, σ_e, is approximated as the conductivity at the initial electrolyte concentration and related to the pitch, *P*, by

$$V_e = IR = \frac{I}{A}\rho l = \sum_{pos,neg,sep} m \frac{I}{A}\frac{P}{\sigma_e\, \varepsilon_e^{1.5}}, \tag{3.13}$$

where V_e is the voltage drop and the current density is

$$\frac{I}{A} = \frac{F\left(c_i^{max} - c_i^0\right)\varepsilon_i\, W_i\, Crate}{3600}. \tag{3.14}$$

i is the electrode with the lowest total capacity. *m* = 0.5 in the positive and negative electrode region because on average only half the current is transported by ionic conduction and the other half by electron conduction in the electrode. *m* = 1 in the separator region. ε_e is the volume fraction of the electrolyte in each region. The electrode pitch should be designed so that V_e is less than 0.1 volts to maximize power performance.

Figure 3.7d further demonstrates how the electrolyte conductance affects power performance. The power density versus energy density is plotted for batteries with 30, 45, and 120 μm electrode pitches. At each pitch, the peak electrolyte conductivity is changed by a factor of 0.01, 0.1, 1 and 10, similar to fig. 3.7a. The performance of batteries with the same electrode pitch and different conductivity is the same at low power densities. As the discharge rate is increased, the energy density of batteries with low electrolyte conductivities becomes inferior to the other batteries with same electrode widths and high conductivities. The inflection point when the power performance significantly decreases is predicted well by equation 3.13 when V_e is 0.1 volts. The inflection point is marked with a black diamond for each battery.

Electrode electron pathway

Figure 3.8a shows how the electrode conductivity affects the energy density of battery 1 at 1 – 500 C discharge rates. The conductivity is varied by up to 1×10^{-8} times the conductivity in table 3.1. The dashed lines in fig. 3.8a correspond to the energy density of batteries where V_s is 0.3 and 0.1 volts. The voltage drop across the electrodes, V_s, is estimated using Ohm's law,

$$V_s = \frac{I}{A}\rho l = 0.5\,\frac{I}{A}\left(\frac{W_{pos}}{k_{pos}^{eff}\,\varepsilon_{pos}^{1.5}} + \frac{W_{neg}}{k_{neg}^{eff}\,\varepsilon_{neg}^{1.5}}\right) = 0.5\,\frac{I}{A}\left(\frac{L^2}{2\,\sigma_{pos}^{eff}\,W_{pos}\,\varepsilon_{pos}^{1.5}} + \frac{L^2}{2\,\sigma_{neg}^{eff}\,W_{neg}\,\varepsilon_{neg}^{1.5}}\right), \quad (3.15)$$

where the current density is calculated from equation 3.14 divided by half because on average only half the conduction across the electrode width is due to electron conduction. σ^{eff} is calculated using equation 3.6 and 3.7 for the bicontinuous electrode and corrected for the porosity using the Bruggeman approximation. L is the length of the current collector foil in conventional electrodes. Figure 3.8b shows simulated power density versus energy density for battery 1 with varying electrode conductivities. The point when the electrode conductivity reduces the power performance is marked with a black diamond and corresponds to when V_s = 0.1 volts. The electron conduction pathway through the battery should be designed so that V_s is

less than 0.1 volts to maximize power performance. In the interdigitated bicontinuous electrodes, the electrode lengths carry a larger voltage drop than the widths and the lengths are the primary engineering parameter for controlling electron conduction.

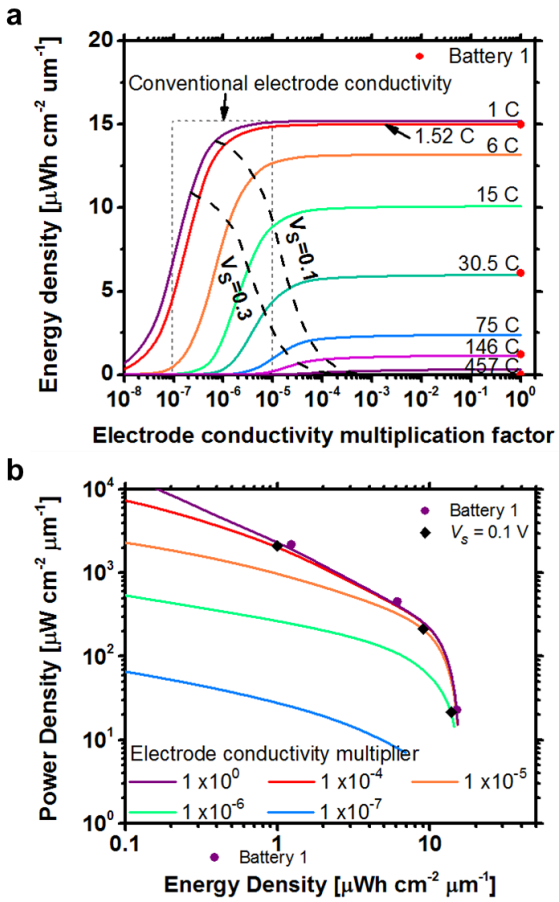

Figure 3.8 (**a**) Simulated energy density versus electrode conductivity multiplication factor for battery 1 at 1 to 457 C rate discharges. The dashed lines are the design parameter, V_s, for the electrode length and architecture calculated with 0.1 and 0.3 voltage drops across the electrode for each C rate. (**b**) Ragone plot of battery 1 as the electrode conductivity is scaled from 10^{-7} to 10^{0}.

Active material thickness (t)

The active material thickness influences the fraction of lithium extracted or inserted into the active material at a discharge rate. A smaller active material thickness or radius allows more capacity to be extracted in less time; however, it is not always possible or practical to engineer the active material as thin as possible. Figure 3.9a illustrates this by showing how the cathode active material thickness in battery 1 affects the energy density at 1 - 500 C rate discharges. A maximum energy density occurs because of competing effects between an increase in the total volume fraction of the active material and an increase in the distance that lithium must travel. The maximum can be predicted by comparing the diffusion time, τ, to the diffusion distance l. Crank shows that shape of the concentration solution is constant for diffusion in slabs, cylinders, and spheres undergoing a constant interface flux when $D\tau/l^2$ is constant (*38*). The amount of lithium extracted or inserted into the active material, integral under the concentration solution curve, is therefore constant for a constant $D\tau/l^2$ when the discharge is stopped at a set surface concentration, which is valid for batteries discharged at a constant C rate. The active material thickness, t_o, can then be related to the diffusivity, D_s, and C rate using,

$$t_o = n\sqrt{\frac{D_s\, 3600}{Crate}}. \tag{3.16}$$

n is a shape factor that changes based on the active material geometry. The dashed line in fig. 3.9a is the energy density corresponding to t_o, when n is 1, which agrees well with the thickness corresponding to the maximum energy density at a given Crate. The extracted capacity for t_o is always 2/3 of the total capacity when n =1 and when the shutoff concentration is set to the maximum concentration in the cathode or minimum in the anode. For spherical particles the extracted capacity is 2/3 of the total when n = $\sqrt{5}$. t_o can be used to design battery active materials to achieve 2/3 of their total capacity when discharged at a set C rate.

Figure 3.9b validates the use of t_o as a design parameter. Figure 3.9b is a Ragone plot for battery 1 simulated with cathode active material thicknesses between 13 and 100 nm. The power curve for 15.5 C, marked as the black curved line that intersects all the Ragone curves, plots the energy and power density of each battery when discharged at a 15.5 C rate. The maximum power performance occurs at the apex of the 15.5 C power curve and corresponds to the 55 nm thick battery, which is the optimal active material thickness predicted from equation 3.16 at 15.5 C rate. The energy and power density corresponding to t_o for each battery is marked with a diamond. Batteries achieve optimal power performance when the active material thickness is t_o.

Figures 3.9c and 3.9d show how the active material thickness affects the power performance independent of the volume fraction by varying the pore size and active material thickness such that the volume fraction remains constant, which is indicative of the design choices in conventional batteries. The pore diameters in fig. 3.9c and 3.9d are approximately proportional to the active material thickness. Figure 3.9c shows the energy densities of battery 1 discharged at various C rates with pore diameters varied between 50 and 2,000 nm. The dashed line in fig. 3.9c shows battery performances when the active material thickness is t_o. Increasing the active material thickness past t_o dramatically reduces the power performance at all C rates, including 1 C. Figure 3.9d is a Ragone plot for battery 1 simulated with pore diameters varied between 100 and 2,000 nm. The power performance can be improved by reducing the pore size (PS diameter) while maintaining the same active material thickness such that a battery fabricated with 109 nm PS diameter particles can be discharged at 300 C and maintain 55% of its total energy density.

Figure 3.10 shows the simulated energy densities of battery 1 when the surface area is changed by an order of magnitude and keeping all other parameters constant. Changing only the

surface area is similar to using different shapes of polystyrene particles for fabricating the battery scaffold. The large changes in energy density for small changes in thickness in fig. 3.9a and 3.9c compared to the small changes in energy density in fig. 3.10 shows that active material thickness has a more significant effect on battery performance than surface area. Therefore, the active material thickness should be a primary descriptor of high power materials, not the surface area.

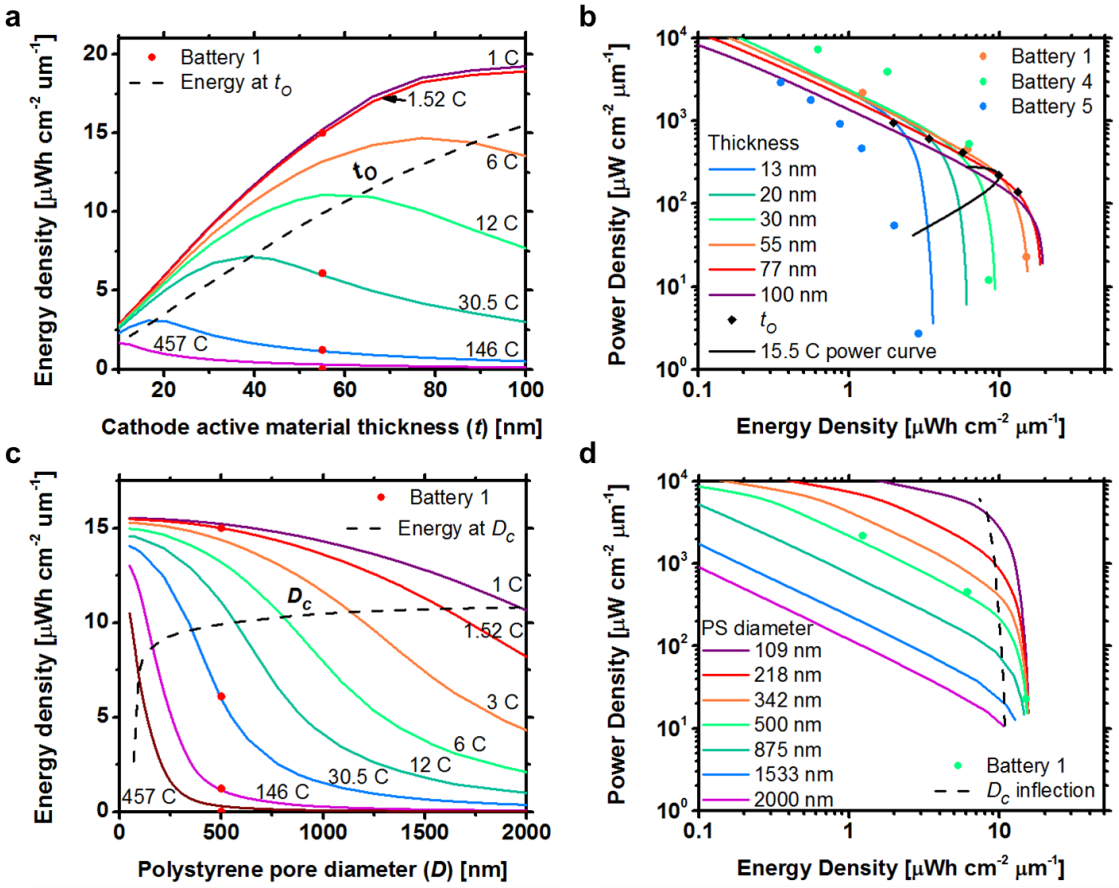

Figure 3.9: (**a**) Simulated energy density versus active material thickness for battery 1 at 1 to 457 C discharge rates. The dashed line is the design parameter t_o for the active material thickness calculated from a 2/3 extracted capacity at each discharge rate. (**b**) Ragone plot of battery 1 as active material thickness is varied. The 15.5 C power curve in is the energy and power density of batteries with varying thickness discharged at 15.5 C rate. Colored dots are experimental data. Black diamonds correspond to inflection points calculated from design parameters. (**c**) Simulated energy density versus pore diameter for battery 1 at 1 to 457 C discharge rates. The active material thickness is varied with the pore size to maintain a constant volume fraction. D_c is the pore diameter corresponding to t_o. (**d**) Ragone plot of battery 1 as active material thickness is varied and volume fraction maintained.

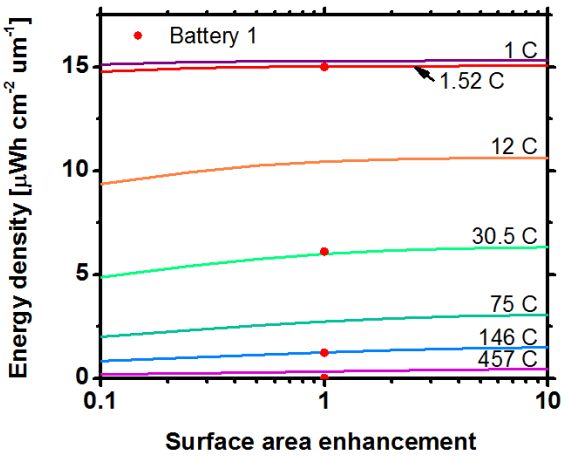

Figure 3.10: Energy density versus surface area enhancement for microbattery 1 at 1 – 457 C rate discharges. Red dots are experimental data.

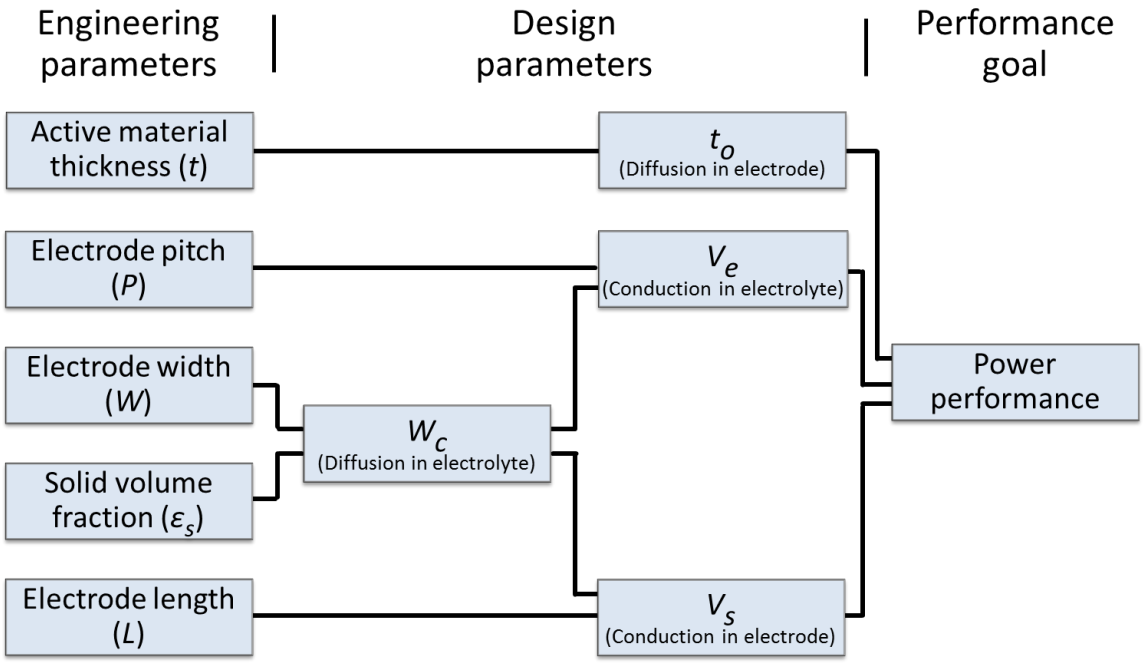

Figure 3.11: A high power performance design tree showing how engineering control parameters in battery architectures are related to important design criteria, their associated physics, and the final goal of high power performance.

Battery design summary

The major engineering parameters that control the power performance are electrode width, *W*, electrode pitch, *P*, electrode conduction pathway, and the active material thickness, *t*. The effect each engineering parameter has on the power performance was probed by simulating the power performance of battery 1 as individual engineering parameters or governing transport properties were varied. From these power performance curves, design rules that relate the battery geometric and material properties to the power performance were developed such that each engineering parameter can be optimized to achieve high power performance. Figure 3.11 summarizes the relationship between engineering parameters, design parameters and the power performance. The relationships between engineering and design parameters are based on battery 1 simulations because battery 1 has the best agreement between simulation and experiment. Data from battery 1 provides the only comparison between experiment and simulation in many of the design plots primarily because it is difficult to fabricate the microbatteries in a way that all engineering parameters and material properties are the same except for changes in a single engineering parameter. Battery 4 and 5 are added to fig. 3.9b because they have many similar parameters to battery 1 but vary in their active material thickness. The good agreement between experiment and simulation in fig. 3.9b, despite the simulation only varying thickness, and fig. 3.4, where parameters are specific to each battery, gives confidence that the design parameters developed are simple and relatively effective tools for optimizing and characterizing the power performance of high power microbatteries.

A battery that achieves 2/3 of its maximum capacity at a desired discharge rate can be designed by, in this order, setting the active material thickness to t_o, the cathode width to W_c, the pitch so $V_e \leq 0.1$, and the electrode architecture and length so that $V_s \leq 0.1$, while iterating the

engineering parameters as design parameters are added. Figure 3.12a shows a diagram of an interdigitated bicontinuous microbattery optimized for a 50 C rate discharge using the design parameters presented here and the same chemistry as the experimental batteries. Figure 3.12b shows discharge curves of the 50 C optimized microbattery. The capacity is 56% of the 1 C capacity at 50 C which agrees well with the 2/3 performance predicted by equation 3.16. Figure 3.12c shows the power performance compared to previously fabricated microbatteries. The energy density of the optimized microbattery at 50 C exceeds the maximum energy density of the fabricated batteries. The 50C optimized design has ≈10 X increase in energy density at 1,000 mW cm^{-2} μm^{-1} power density and ≈10 X increase in power density at 10 µWh cm^{-2} μm^{-1} energy density. The most significant power performance improvements were due to increasing the cathode width to improve the total energy density and decreasing the pore size to 250 nm. A sensitivity analysis shows how varying the engineering parameters away from the design parameters affect the power performance. Figure 3.12d shows sensitivity analysis results when all combinations of the active material thickness and electrode width are varied by ±10 and 25%. Microbatteries with better power performance than the 50 C optimized design are to the right of the red line. A majority of the microbatteries have lower power performance than the 50 C rate optimized design, which shows that microbatteries based on the design parameters will be near the local maximum power performance.

In addition to design optimization, the design parameters provide a basic characterization tool. The differences between experimental active material thicknesses or electrode widths and their design parameters, as well as calculating V_e and V_s and comparing the voltages to fig. 3.7 and 3.8, give insights into which parameters most limit battery power performance.

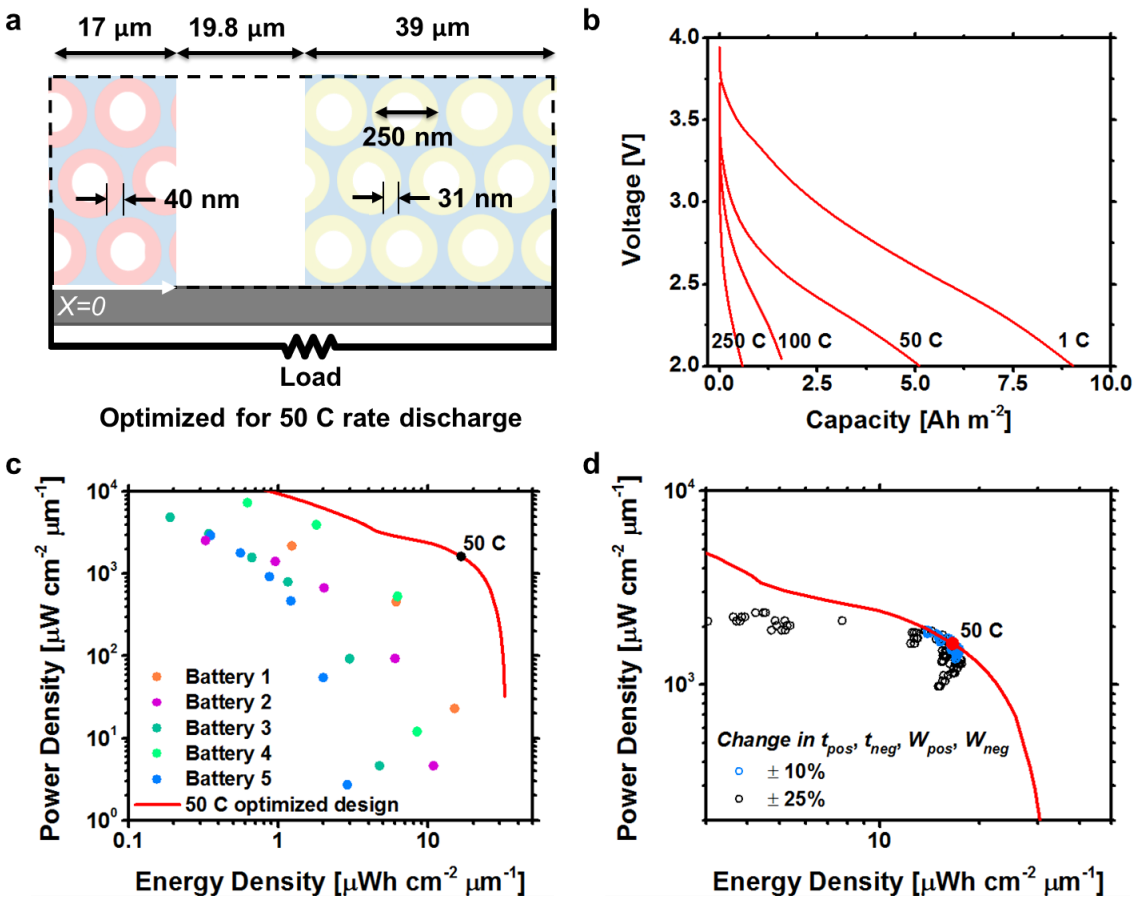

Figure 3.12: (**a**) A schematic of a battery architecture optimized for a 50 C discharge rate using the design rules presented here. The battery performance is then tested using the 1-D transport simulation. (**b**) Discharge curve of the battery. (**c**) Ragone plot of the battery performance compared to experimental batteries. The 50 C rate discharge point is marked. (**d**) Sensitivity analysis of the optimized battery. The electrochemically active material thickness and electrode width are independently and simultaneously varied by plus and minus 10 and 25 percent.

3.5 Conclusion

In conclusion, the performance of microbatteries with up to 7.4 mW cm^{-2} μm^{-1} power density are simulated using a 1-D transport model combined with a geometric model of the bicontinuous electrodes. The 1-D model shows good agreement between simulation and experiment at up to 600 C rate discharges and indicates that diffusion through the electrochemically active material limits batteries power performance. Individual engineering

parameters are tuned in the model to understand how they affect microbattery power performance, or amount of energy extracted at a power density. The trade-offs between energy and power density guide the development of design parameters that allow characterization and optimization of battery performance without multi-physics simulations. A 50 C rate optimized microbattery based on the interdigitated bicontinuous architecture shows a ≈10 X improvement in power performance, indicating that significant improvements in power performance are possible with advances in microbattery design and fabrication. The 1-D electrochemical model and design parameters provide a new tool for developing novel material architectures, nano composites, and full battery cells with improved power performance, which is critical for the maximum exploitation of energy storage technologies in many applications.

3.6 References

1. D. Golodnitsky *et al.*, Progress in three-dimensional (3D) Li-ion microbatteries. *Solid State Ionics* **177**, 2811 (Oct, 2006).
2. T. S. Arthur *et al.*, Three-dimensional electrodes and battery architectures. *MRS Bulletin* **36**, 523 (2011).
3. J. W. Long, B. Dunn, D. R. Rolison, H. S. White, Three-dimensional battery architectures. *Chemical Reviews* **104**, 4463 (Oct, 2004).
4. V. Narain, "Global thin-film batteries (TFB) market" (Frost and Sullivan, 2013).
5. J. H. Pikul, H. Gang Zhang, J. Cho, P. V. Braun, W. P. King, High-power lithium ion microbatteries from interdigitated three-dimensional bicontinuous nanoporous electrodes. *Nat. Commun.* **4**, 1732 (2013).
6. P. V. Braun, J. Cho, J. H. Pikul, W. P. King, H. Zhang, High power rechargeable batteries. *Curr. Opin. Solid State Mater. Sci.* **16**, 186 (2012).
7. C. Liu *et al.*, An all-in-one nanopore battery array. *Nat Nano* **9**, 1031 (2014).
8. Y. Tang, Y. Zhang, W. Li, B. Ma, X. Chen, Rational material design for ultrafast rechargeable lithium-ion batteries. *Chemical Society Reviews*, (2015).
9. S. Lee, Y. Cho, H.-K. Song, K. T. Lee, J. Cho, Carbon-Coated Single-Crystal LiMn2O4 Nanoparticle Clusters as Cathode Material for High-Energy and High-Power Lithium-Ion Batteries. *Angewandte Chemie International Edition* **51**, 8748 (2012).
10. S. Chen *et al.*, Self-supported Li4Ti5O12 nanosheet arrays for lithium ion batteries with excellent rate capability and ultralong cycle life. *Energy & Environmental Science* **7**, 1924 (2014).

11. M. A. Martin *et al.*, Morphological Influence in Lithium-Ion Battery 3D Electrode Architectures. *J. Electrochem. Soc.* **162**, A991 (January 1, 2015, 2015).
12. A. Shah *et al.*, A Layered Carbon Nanotube Architecture for High Power Lithium Ion Batteries. *J. Electrochem. Soc.* **161**, A989 (January 1, 2014, 2014).
13. Y. Tang *et al.*, Unravelling the Correlation between the Aspect Ratio of Nanotubular Structures and Their Electrochemical Performance To Achieve High-Rate and Long-Life Lithium-Ion Batteries. *Angewandte Chemie International Edition* **53**, 13488 (2014).
14. A. S. Westover *et al.*, On-chip high power porous silicon lithium ion batteries with stable capacity over 10 000 cycles. *Nanoscale* **7**, 98 (2015).
15. X. Wang *et al.*, Cu/Li4Ti5O12 scaffolds as superior anodes for lithium-ion batteries. *NPG Asia Mater* **7**, e171 (2015).
16. H. Zhang, X. Yu, P. V. Braun, Three-dimensional bicontinuous ultrafast-charge and -discharge bulk battery electrodes. *Nat. Nanotechnol.* **6**, 277 (2011).
17. M. Doyle, J. Newman, A. S. Gozdz, C. N. Schmutz, J.-M. Tarascon, Comparison of Modeling Predictions with Experimental Data from Plastic Lithium Ion Cells. *J. Electrochem. Soc.* **143**, 1890 (1996).
18. T. F. Fuller, M. Doyle, J. Newman, Simulation and Optimization of the Dual Lithium Ion Insertion Cell. *J. Electrochem. Soc.* **141**, 1 (January 1, 1994, 1994).
19. M. Doyle, J. Newman, Modeling the performance of rechargeable lithium-based cells: design correlations for limiting cases. *J. Power Sources* **54**, 46 (1995).
20. Á. G. Miranda, C. W. Hong, Integrated modeling for the cyclic behavior of high power Li-ion batteries under extended operating conditions. *Applied Energy* **111**, 681 (2013).
21. C. Min, G. A. Rincon-Mora, Accurate electrical battery model capable of predicting runtime and I-V performance. *Energy Conversion, IEEE Transactions on* **21**, 504 (2006).
22. I. Papic, Simulation model for discharging a lead-acid battery energy storage system for load leveling. *Energy Conversion, IEEE Transactions on* **21**, 608 (2006).
23. P. Arora, M. Doyle, A. S. Gozdz, R. E. White, J. Newman, Comparison between computer simulations and experimental data for high-rate discharges of plastic lithium-ion batteries. *J. Power Sources* **88**, 219 (2000).
24. O. Tremblay, L. A. Dessaint, A. I. Dekkiche, in *Vehicle Power and Propulsion Conference, 2007. VPPC 2007. IEEE*. (2007), pp. 284-289.
25. K. Smith, C.-Y. Wang, Solid-state diffusion limitations on pulse operation of a lithium ion cell for hybrid electric vehicles. *J. Power Sources* **161**, 628 (2006).
26. D. Cericola, P. W. Ruch, R. Kötz, P. Novák, A. Wokaun, Simulation of a supercapacitor/Li-ion battery hybrid for pulsed applications. *J. Power Sources* **195**, 2731 (2010).
27. S. Buller, M. Thele, R. W. A. A. De Doncker, E. Karden, Impedance-based simulation models of supercapacitors and Li-ion batteries for power electronic applications. *Industry Applications, IEEE Transactions on* **41**, 742 (2005).
28. B. Schweighofer, K. M. Raab, G. Brasseur, Modeling of high power automotive batteries by the use of an automated test system. *Instrumentation and Measurement, IEEE Transactions on* **52**, 1087 (2003).
29. P. M. Gomadam, J. W. Weidner, R. A. Dougal, R. E. White, Mathematical modeling of lithium-ion and nickel battery systems. *J. Power Sources* **110**, 267 (2002).
30. K. Smith, C.-Y. Wang, Power and thermal characterization of a lithium-ion battery pack for hybrid-electric vehicles. *J. Power Sources* **160**, 662 (2006).

31. J. M. Sullivan, D. C. Hanson, R. Keller, Diffusion Coefficients in Propylene Carbonate, Dimethyl Formamide, Acetonitrile, and Methyl Formate. *J. Electrochem. Soc.* **117**, 779 (June 1, 1970, 1970).
32. S.-i. Tobishima, T. Okada, Lithium cycling efficiency and conductivity for high dielectric solvent/low viscosity solvent mixed systems. *Electrochim. Acta* **30**, 1715 (1985).
33. K. Xu, Nonaqueous Liquid Electrolytes for Lithium-Based Rechargeable Batteries. *Chemical Reviews* **104**, 4303 (2004/10/01, 2004).
34. B. Klassen, R. Aroca, M. Nazri, G. A. Nazri, Raman Spectra and Transport Properties of Lithium Perchlorate in Ethylene Carbonate Based Binary Solvent Systems for Lithium Batteries. *The Journal of Physical Chemistry B* **102**, 4795 (1998/06/01, 1998).
35. M. Ue, Mobility and Ionic Association of Lithium and Quaternary Ammonium Salts in Propylene Carbonate and γ-Butyrolactone. *J. Electrochem. Soc.* **141**, 3336 (December 1, 1994, 1994).
36. N. J. Dudney *et al.*, Nanocrystalline Li x Mn2 − y O 4 Cathodes for Solid-State Thin-Film Rechargeable Lithium Batteries. *J. Electrochem. Soc.* **146**, 2455 (July 1, 1999, 1999).
37. M. Winter, J. O. Besenhard, Electrochemical lithiation of tin and tin-based intermetallics and composites. *Electrochim. Acta* **45**, 31 (1999).
38. J. Crank, *The mathematics of diffusion*. (Clarendon press Oxford, 1975), vol. 2.

CHAPTER 4

INTEGRATION OF HIGH CAPACITY MATERIALS INTO INTERDIGITATED ELECTRODES FOR HIGH ENERGY AND HIGH POWER DENSITY PRIMARY MICROBATTERIES

4.1 Introduction

Integration of miniature sensors and radio devices into consumer goods, biomedical devices, and industrial electronics has driven significant interest in microbatteries (*1*). Developments in electrode structure engineering have enabled microbatteries with power densities 100 times greater than commercial lithium ion batteries (up to 7.4 mW cm^{-2} μm^{-1}) (*2-4*); however, the volumetric energy density of all microbatteries lags behind that of conventional format batteries (*2-11*), limiting their application. The high power densities were achieved with interdigitated mesostructured electrode architectures that simultaneously reduce ion and electron transport resistances in the anode, cathode, and electrolyte. The electrodes consisted of thin films of electrochemically active materials coated on highly conductive porous metal current collectors, providing good electrical conductivity and reduced solid state ion diffusion distances (*2, 3*). Electrode interdigitation reduced ion transport lengths across the electrolyte. Here we consider how microbatteries with both high energy and power density can be realized by integrating large volume fractions of high capacity materials into high power microbattery architectures.

Integration of high capacity materials into high power architectures is challenging. Not

only must electrochemically active material be deposited with nanometer-scale thickness control within high surface area porous current collectors, but also in an interdigitated design, one must prevent electrical shorts and chemical contamination between narrowly spaced electrodes. Gas-phase deposition methods (e.g. ALD and CVD) provide high quality conformal coatings but require complicated strategies to limit deposition to only the anode or cathode (*4, 10, 11*). Electrodeposition techniques that take advantage of the electrical separation between anode and cathode have been used to deposit materials into high power electrodes, but the low electrochemically active material volume fractions provide limited energy density (*2, 3*). High capacity material selection is important for achieving high energy and power density, which has led to community to consider high capacity anode materials such as silicon and tin [(12)], lithium (*13-17*), and conversion reaction based oxides (*18-20*). Lithium is an interesting anode for primary and secondary batteries due to its high capacity, low density, and low reference voltage; however, dendrite and solid electrolyte interphase (SEI) evolution during lithium deposition limits its immediate use to primary battery systems (*13-17, 21-30*). High voltage cathode materials improve the total energy of a battery; however, the high processing temperature traditionally required for crystallization would be destructive to other microbattery components (*18-20, 31*).

Here we combine new techniques that integrate large volume fractions of high capacity materials into high power microbattery architectures with new material systems that can be processed near room temperature, enabling primary microbatteries with improved energy and power density. The primary microbatteries reported here contain manganese oxide conversion cathodes and lithium anodes integrated into an interdigitated 3D mesostructured bicontinuous architecture which simultaneously provides high energy and high power density. The

microbatteries have energy densities up to 45.5 μWh cm^{-2} μm^{-1}, which is greater than previous 3D microbatteries and comparable to commercially available conventional format lithium based batteries (*2*, *5-7*).

4.2 Results and Discussion

Integration

Figure 4.1a shows the interdigitated electrode architecture. The cathode is a composite electrode composed of a highly porous bicontinuous nickel current collector conformally coated with high volume fractions of high capacity manganese oxide. The anode is densely electroplated lithium metal. Figure 4.1b shows scanning electron microscope images of the microbattery electrodes. The electrodes are 15 um tall, 33 μm wide, and 45 μm center-to-center. This architecture is chosen to enable high power density by reducing ion and electron transport resistances (*2*, *3*, *32*, *33*). The bicontinuous cathode offers short lithium diffusion lengths through the manganese oxide and highly conductive continuous electron pathways in the nickel current collector. The bicontinuous current collector is not used in the lithium metal anode because lithium is electrically conductive and undergoes a de-plating reaction with no diffusion, eliminating the need for a continuous electron pathway and thin film morphology. The interdigitated electrodes reduce the voltage drop across the electrolyte by shortening ion diffusion and migration distances between electrodes (*3*).

Conversion reaction based manganese oxide is used as the cathode in the primary microbatteries because of its high irreversible capacity, ≈1 V average versus lithium, and room temperature processing, in contrast to its typical use as an anode (*18-20*). Lithium is used as the anode due to its high capacity and low, constant reference voltage which is important when using

lower voltage cathodes. The battery voltage can be up converted to a constant 1.8 to 5.5 volts at greater than 90% efficiency using recently developed boost converters, like the Texas Instruments tps61200, in the case where the battery voltage is too low to integrate directly to electronics.

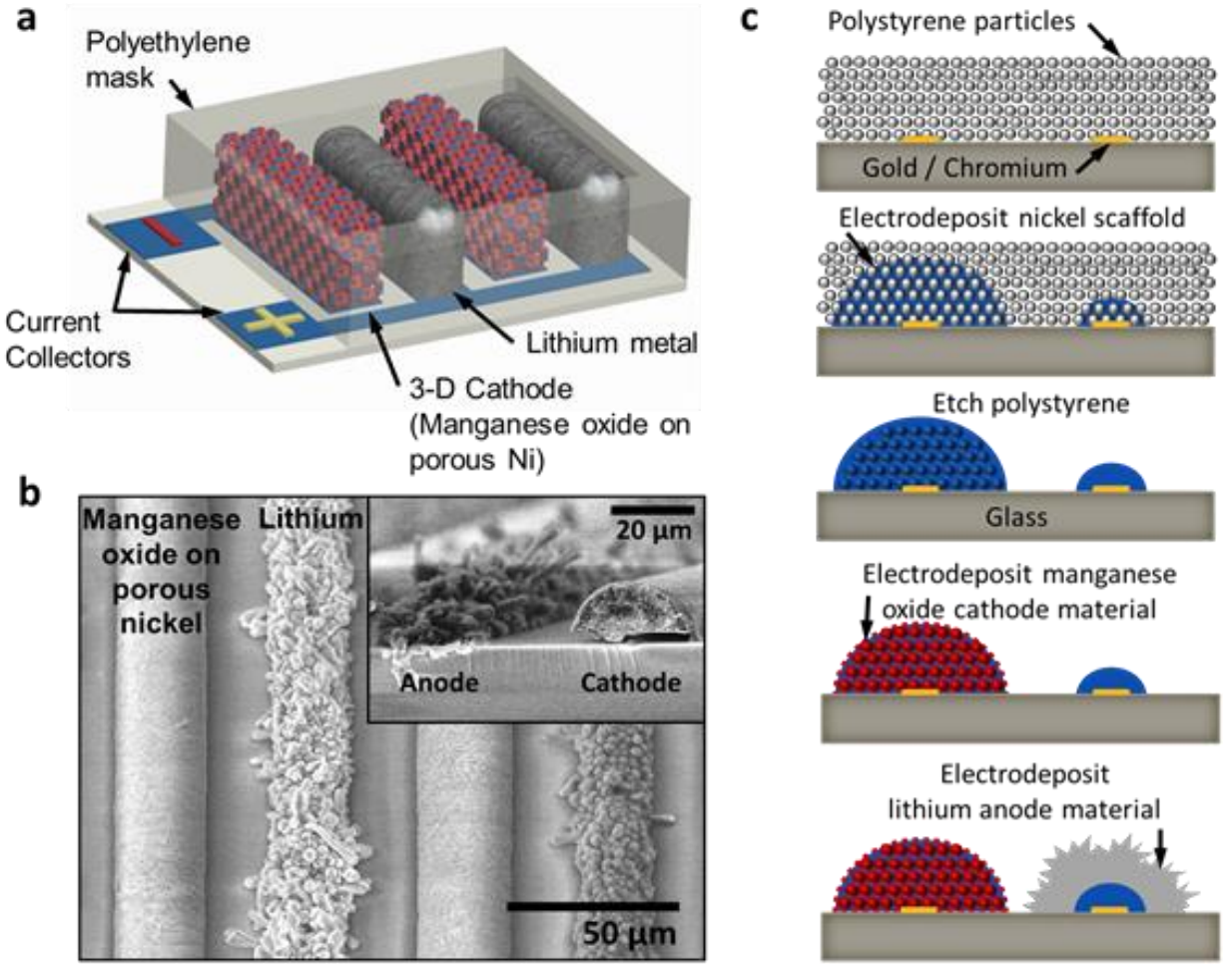

Figure 4.1: (**a**) The microbattery design, consisting of high capacity anode and cathode chemistry integrated into an interdigitated 3D mesostructured bicontinuous architecture that enables high power and high energy density. The mesoporous cathode is conversion reaction based manganese oxide (red) coated on an electrically conductive bicontinuous nickel current collector (blue). The anode is electrodeposited lithium. (**b**) Scanning electron microscope images of the interdigitated electrodes. The inset shows an anode and cathode cross-section. (**c**) Microbattery fabrication process. Polystyrene spheres are first self-assembled on to a gold coated glass substrate followed by nickel electrodeposition through the polystyrene. The polystyrene is then etched and manganese oxide is conformally coated on the porous nickel current collector.

Lithium is then densely electrodeposited on the other nickel current collector using a cesium salt based electrolyte.

Manganese oxide cathode

The manganese oxide is integrated into the microbattery architecture using electrodeposition. A key challenge is depositing large volume fractions of manganese oxide without compromising the electrode features that enable high power. The bicontinuous current collector initially has 500 nm diameter pores which grow smaller as manganese oxide is deposited onto the nickel, until they finally pinch closed. If the manganese oxide deposition is not conformal, the closed pores in one region of the electrode will prevent lithium ions from flowing to the rest of the electrode volume. To achieve conformal coating of manganese oxide in the porous nickel scaffold, the manganese oxide is cycled between additive electrochemical deposition and subtractive electrochemical stripping. Figure 4.2a shows the voltage profile and resulting current for two cycles of the voltage controlled electrodeposition and electrochemical stripping process. Manganese oxide was deposited at 0.6 volts vs. Ag/AgCl for eight seconds followed by stripping at -0.95 and -0.8 volts for 2 seconds each and open circuit for 25 seconds (0 mA). The voltage regulated the rate of material deposition or stripping and the time controlled the total deposit thickness. Similar to the time delay in transmission lines, the deposition process in porous media has a time delay where the electrolyte capacitance causes the oxide to preferentially deposit or strip at the electrode top near the bulk electrolyte (*34*). The two stripping voltages in Fig. 4.2a take advantage of the time delay. The -0.95 volt etch for 2 seconds stripped a large amount of oxide mostly near the electrode top. Reducing the etch voltage to -0.8 volts for the last 2 seconds reduced the amount of stripping at the electrode middle and bottom. This combination resulted in conformal deposition. Holding the voltage at -0.95 volts for the entire 4 seconds caused over etching in the middle and bottom electrode, resulting in a gradient in oxide

thickness from top to bottom. Figure 4.2b shows top, middle, and bottom SEMs of an electrode after 30 cycles of deposition and stripping using the waveform in Fig. 4.2a. The thickness of the oxide in the bottom and middle of the electrode was 40 – 50 nm, corresponding to 29% – 36% volume fraction of manganese oxide. The oxide coating was thinnest at the top, which is beneficial for high power density as the thin oxide allows larger volumes of electrolyte in the structure, and reduces the time for ions to diffuse to the interior of the electrode.

If stripping is not used, or the electrode is excessively stripped, very non-uniform manganese oxide deposition is observed. Figure 4.2c shows an electrode cross-section when stripping is not used during manganese oxide deposition. The manganese oxide layer is 500 nm thick at the electrode top and only a few nanometers thick at the electrode bottom. In this experiment, manganese oxide was deposited using 10 cycles of 0.6 volts for 4 seconds followed by open circuit for 25 seconds. Reducing the applied voltage time to less than a second did not significantly improve the uneven oxide deposition, indicating that the gradient in oxide thickness is not due to ion diffusion limitations in the electrolyte. The voltage, time, and duration between pulses controls the location of the thickest layer of manganese oxide as illustrated by the following experiment. Figure 4.2d shows the cross section of an electrode deposited using 29 cycles of 0.6 volts for 8 seconds followed by -0.8 volts for 2 seconds, open circuit for 10 seconds, -0.95 volts for 3 seconds, and open circuit for 25 seconds. The manganese oxide thickness alternates from thin on the electrode bottom to thick in the middle and thin again at the electrode top. The open circuit duration between stripping voltages caused most of the stripping to occur at the electrode top, compared to the result in Fig. 4.2a with no off time, which resulted in conformal deposition. Under proper conditions, the pulsed deposition and stripping of manganese oxide enables highly conformal and thick deposition, enabling a high active material

volume fraction. Experimentally, the volume fraction of the electrochemically active material was up to 50% of the available electrode volume, and most electrodes investigated had 30 - 40% manganese oxide by volume.

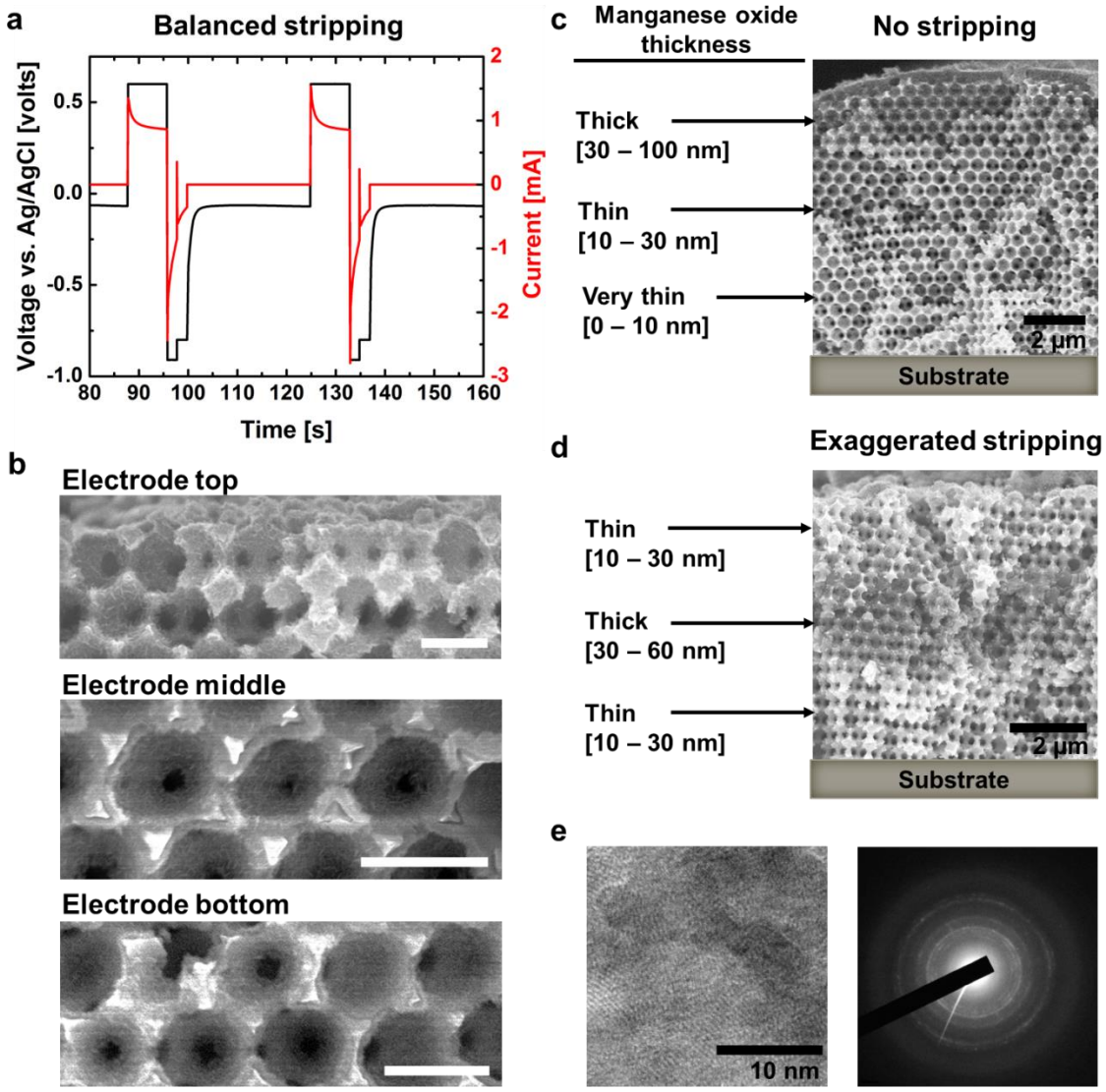

Figure 4.2: (**a**) The applied voltage and resulting current vs. time of the pulsed manganese oxide deposition technique. Manganese oxide deposits under positive applied voltage and is stripped under negative applied voltage to ensure a conformal coating on the mesoporous nickel scaffold. (**b**) SEM cross sections of the top, middle, and bottom of a microbattery cathode after deposition with the voltage profile in (a). The scale bars are 500 nm. (**c**) An SEM of an electrode cross section when no stripping is used. (**d**) An SEM of an electrode cross section where the thickest manganese oxide is deposited in the center of the electrode illustrating the ability to specifically engineer the thickness of the manganese oxide across the electrode depth. (**e**) TEM and selected

area diffraction images of the manganese oxide showing polycrystalline grains with nanometer grain size.

Lithium anode

The lithium anode was grown from a mixture of $LiClO_4$ and $CsPF_6$ in propylene carbonate/vinylene carbonate electrolyte. We initially found depositing thick and dense lithium metal films without forming electrical shorts between the deposited lithium and cathode to be challenging because of dendritic growth, leading to selection of this deposition chemistry (*13-17*). Table 4.1 shows the electrolytes tested to deposit lithium as well as their columbic efficiencies, which measures the capacity extracted from the deposited lithium compared to the charge during the plating process. Some electrolytes had columbic efficiencies as high as 80% due to the formation of a thin, solid SEI, which prevented the deposited lithium from further reacting with the electrolyte; however, these electrolytes still formed dendrites which shorted the battery before a large amount of lithium could be deposited. To suppress dendrite formation cesium salts were added to the electrolyte. Cesium ions have been reported to ionically shield the dendritic tips, smoothing the deposited lithium (*13*). Figure 4.3a shows the voltage during lithium deposition from an electrolyte consisting of 1 M $LiClO_4$ and 0.05 M $CsPF_6$ in 80% v/v propylene carbonate and 20% v/v vinylene carbonate at 0.75 mA cm^{-2} of interdigitated anode area. The voltage is kept above negative 0.1 volts, which is the reduction voltage of 0.05 M Cs^+ relative to 1 M Li^+ versus lithium (*13*). Figure 4.3b shows lithium dendrites formed after lithium deposition in this electrolyte. Figure 4.3c shows dendrites formed when lithium was deposited using 1 M $LiClO_4$ in cesium-free 1:1 EC:DMC electrolyte (a common battery electrolyte), which is indicative of the dendrite formation in cesium-free electrolytes. The dendrites formed in cesium-containing electrolytes were generally shorter, thicker, and less porous than those

deposited without cesium. The increased density of the dendrites formed in the cesium based electrolyte led to significantly higher anode capacities than lithium anodes deposited using electrolytes with high columbic efficiency but thinner and more porous dendrites.

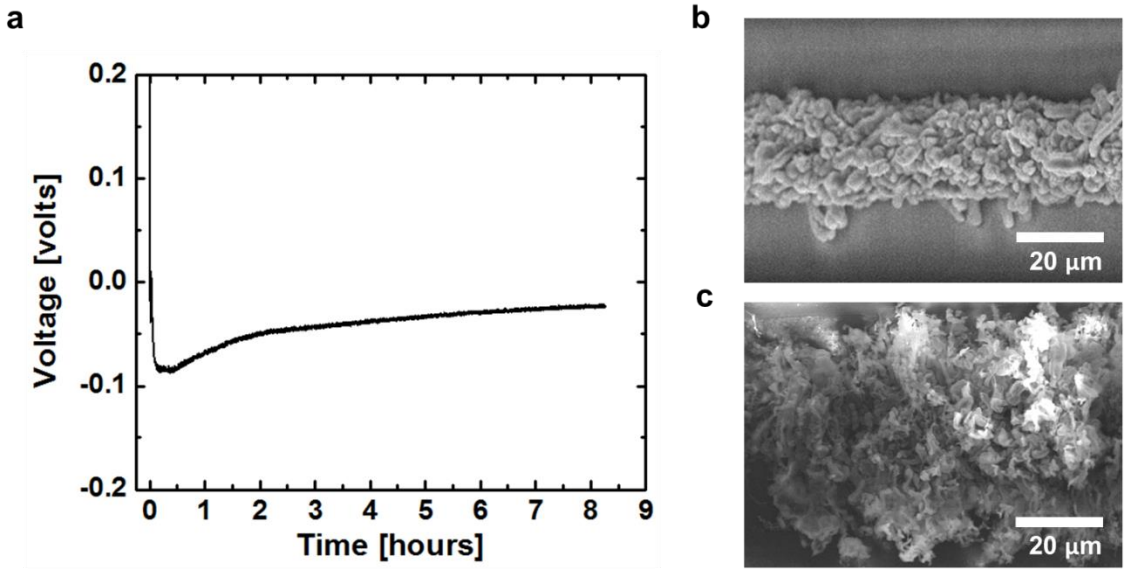

Figure 4.3: (**a**) Voltage versus time for lithium deposition at 0.75 mA cm^{-2} using 1 M $LiClO_4$ and 0.05 M $CsPF_6$ in 80% propylene carbonate and 20% vinylene carbonate. The voltage is versus lithium. (**b**) SEM of lithium deposited in (a). (**c**) SEM of lithium deposited using 1M $LiClO_4$ in 1:1 ethylene carbonate : dimethyl carbonate, a conventional battery electrolyte.

Table 4.1: Cycling efficiency of electrolytes tested for lithium metal deposition

Solvent	Salt	Cycling Efficiency [%]
2-methyltetrahydrofuran	1.5 M $LiAsF_6$	80
2-methyltetrahydrofuran w/ 1 % 2-methylfuran	1.5 M $LiAsF_6$	59
1:1 ethylene carbonate : 2-methyltetrahydrofuran	1.5 M $LiAsF_6$	66
2-methyltetrahydrofuran	1 M $LiPF_6$	< 10
1:1 ethylene carbonate : tetrahydrofuran	1 M $LiPF_6$	66
1,3-dioxolane	1.5 M $LiAsF_6$	69
dimethyl sulfoxide	1 M LiPF6	47
propylene carbonate	1 M $LiClO_4$	60
propylene carbonate w/ 0.05 M $CsPF_6$	1 M $LiPF_6$	43
propylene carbonate w/ 0.05 M $CsPF_6$	1 M $LiClO_4$	48
propylene carbonate w/ 20% vinylene carbonate & 0.05 M $CsPF_6$	1 M $LiClO_4$	45

Electrochemical Performance

Figure 4.4a shows a galvanostatic discharge curve for a primary microbattery between 3.2 and 0.5 volts. The voltage had an initial large slope versus capacity that changed to a smaller slope at 1.4 volts. The large slope in the discharge curve from 3.2 to 1.4 volts was from an intercalation reaction in the cathode, similar to previously reported Mn_2O_3 and Mn_3O_4 anodes during the first discharge (*18-20, 35*). The cathode then underwent conversion of the manganese oxide to lithium oxide and SEI formation reactions from 1.4 to 0.5 volts that account for 85% of the total capacity. The capacity due to SEI formation and other irreversible reactions was approximated by comparing the first and second discharge cycles of manganese oxide processed on a thin film of nickel. The manganese oxide was cycled between 3.5 and 0.25 volts to reduce the manganese oxide without reducing the gold under the nickel current collectors. The capacity of the first and second discharge at 0.5 volts were compared, and not the capacity at 0.25 volts, because of the 0.5 volt shutoff used in the full microbattery cell. The capacity at 0.5 volts was 2.25 times greater in the first cycle than the second cycle, indicating SEI formation and other irreversible reactions in the cathode enhanced the energy density of the full microbattery by about 100% when discharged to 0.5 volts. The capacity of the first discharge at 0.5 volts was 1.4 times greater than the reversible capacity at 0.25 volts indicating the capacity of the first manganese oxide discharge to 0.5 volts was similar to the 800 mAh g^{-1} reversible capacity reported for conversion reaction based manganese oxides (*18-20, 35*).

The microbatteries maintain high energy density when discharged at high average power densities, up to 2,300 μW cm^{-2}μm^{-1}. Figure 4.4b shows the voltage of a full cell discharged at various current densities. The voltage initially fell of quickly as the battery was discharged at high rate until it reached 0.5 volts. The battery was then discharged at lower rates until the full capacity was extracted, with 5 – 10 minutes of open circuit between discharges. The black curve

shows the lithium anode voltage versus a lithium reference electrode during the discharge. Near the end of discharge the lithium voltage increased dramatically. The total energy extracted for each discharge rate was the sum of the energy extracted at that rate and the energy extracted for all previous higher power rates. This approach enabled accurate rate performance data for batteries that can only be discharged once (*36*). The average power densities at each discharge were 2,300, 790, 120, 40, 15, 4, and 1 μW cm^{-2} μm^{-1}, with corresponding energy densities of 0.3, 1.9, 5.0, 7.8, 11.3, 19.7, and 45.5 μWh cm^{-2} μm^{-1}. Discharging the microbatteries to a cut-off voltage lower than 0.5 volts could further improve the energy density; however, the sharp increase in anode voltage at the end of discharge shows the energy density is limited by the amount of lithium deposited.

In addition to high constant current discharges, the microbatteries were discharged with multiple high pulsed currents, which more closely mimic microbattery use in applications such as sensing and wireless communication. Figure 4.4c shows a segment of a microbattery discharge curve during pulsed discharge. The same voltage profile as Fig. 4.4a can be seen with the addition of sharp decreases in voltage corresponding to high current discharges. The microbatteries had a zero volt shut-off limit to mimic scenarios where high power and high depth of discharge are needed. The first pulsed discharge was a 50 millisecond 1950 μA cm^{-2} μm^{-1} current for 120 cycles, with a constant current discharge of 0.3 μA cm^{-2} μm^{-1} between pulses. The battery was then discharged for 50 milliseconds at 970 μA cm^{-2} μm^{-1} for 180 cycles, with an open circuit between pulses. Figure 4.4d shows two cycles for each of these pulses. The microbattery voltage returned to approximately 75% of its pre-high rate discharge voltage within 1 second of rest under both pulsed discharge conditions. The discharge performance shows that the microbatteries can alternate between supercapacitor equivalent high power pulsed discharges

and low power / high energy sleep discharges, which is important for many wireless and remote system applications.

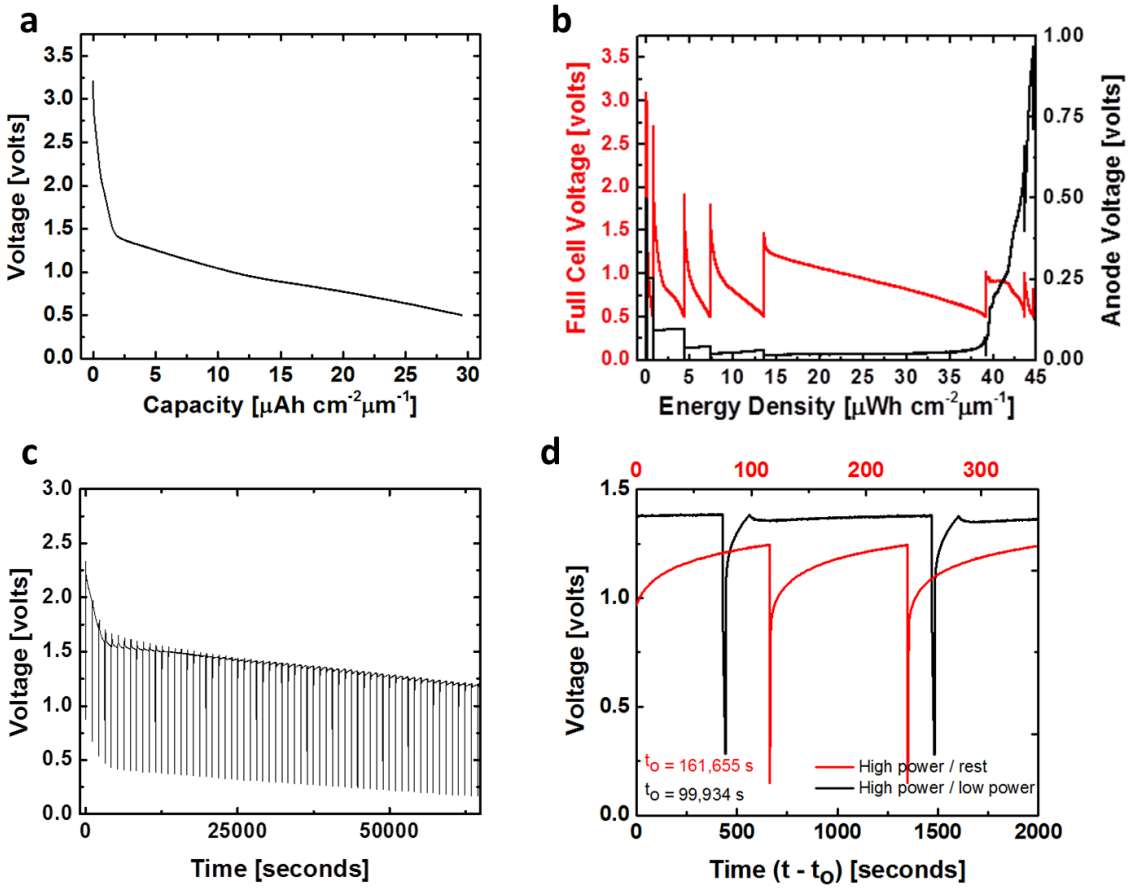

Figure 4.4: (**a**) A microbattery discharge curve. (**b**) A microbattery sequentially discharged at high to low current density with 5 – 10 minutes open circuit rests in between discharges. The peak energy and power densities are 45.5 µWh cm^{-2} $µm^{-1}$ and 5,300 µW cm^{-2} $µm^{-1}$. (**c**) The first 21 hours of a microbattery discharged with short, very high current pulses indicative of use in sensing and wireless communication applications. (**d**) Zoomed in sections of the pulsed discharge curve for the microbattery in (c). The black curve shows the battery voltage after 50% depth of discharge during a 50 ms high current pulse (1950 µA $cm^{-2}µm^{-1}$), followed by a 2 minute open circuit rest and 15 minute low power discharge. The red curve shows the battery voltage after 85% depth of discharge during a 970 µA cm^{-2} $µm^{-1}$ pulse for 50 ms, followed by a 2 minute open circuit rest.

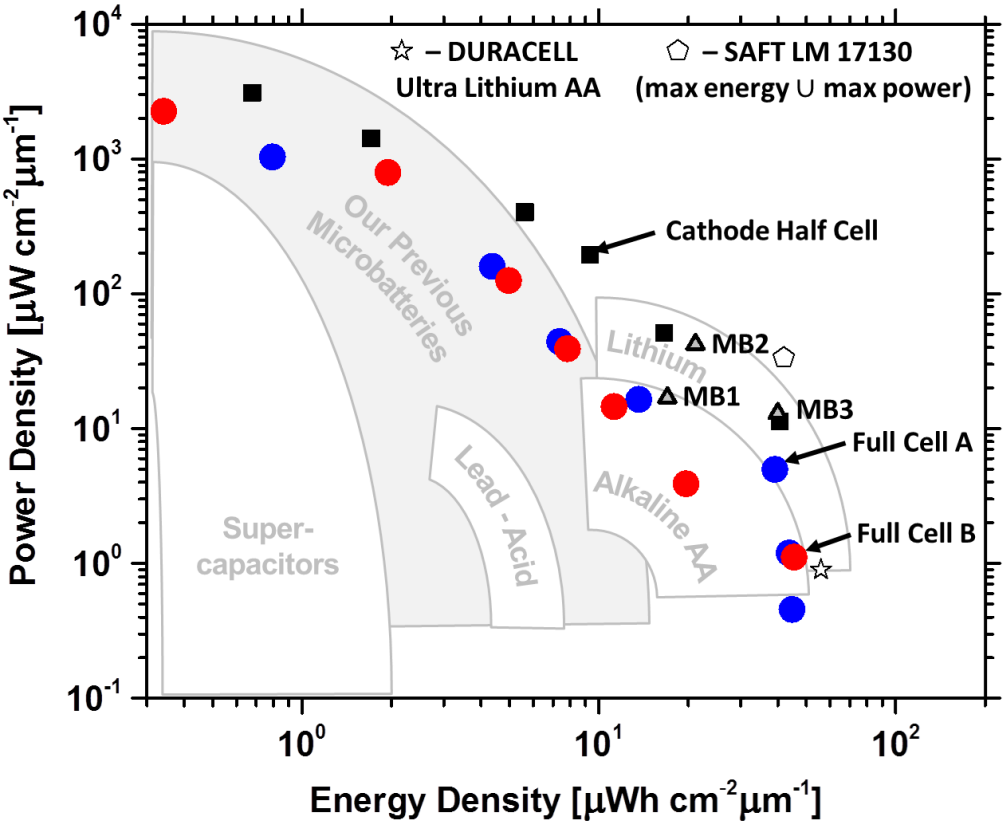

Figure 4.5: A Ragone plot comparing the power and energy density of two primary microbatteries (red and blue) to other technologies. The cathode half-cell (no lithium anode) is shown in black, along with recently published secondary microbatteries plotted at their highest energy density (MB1 through MB3). The plot also includes in the background the performance range of commercially available energy storage technologies and lithium/manganese oxide primary batteries from SAFT and DURACELL. The SAFT cell is plotted at the maximum energy density, 42 µWh cm^{-2} $µm^{-1}$, and maximum recommended power, 34 µW cm^{-2} $µm^{-1}$. The max energy and power are plotted together, despite the achievable energy at the maximum power being less than 42 µWh cm^{-2} $µm^{-1}$, because the energy density at the max power is not reported. The primary microbatteries have comparable energy density to commercially available primary batteries and 50X higher power densities, comparable to supercapacitors.

Figure 4.5 shows the average power density versus energy density of two full microbattery cells tested at multiple discharge rates. The data is presented on a Ragone plot to compare it to other energy storage technologies, including high power rechargeable microbatteries previously published by us (*2*). At low power, the two primary microbatteries have 44.7 and 45.5 µWh cm^{-2} $µm^{-1}$ energy densities. At high power the primary microbatteries

have similar energy and power density performance to our previous secondary microbatteries, which is ~100 X higher power density than other 3D microbatteries. The low rate energy densities corresponds to 2X the energy density of the best 3D secondary microbatteries, with the exception of work done by Lai et al. which achieved a cyclable 40 μWh cm^{-2} μm^{-1} energy density (*5-7*). The primary microbatteries have similar energy densities to commercially available lithium/manganese oxide based primary batteries with a ~50 X higher peak power density.

4.3 Conclusion

Primary microbatteries made from high capacity, low voltage materials integrated into high power architectures achieved 45.5 μWh cm^{-2} μm^{-1} energy and 5,300 μW cm^{-2} μm^{-1} peak power density. The interdigitated 3D mesostructured bicontinuous architecture enabled ultra-high power density. Proper electrochemical deposition strategies for the 3D mesoporous current collector and dense lithium anode deposition, coupled with judicious electrochemically active material choices enabled a high energy density. This demonstration of applying high energy density primary chemistry to the high power micro architecture provides confidence that the micro architecture concept can be extended to other battery chemistries to achieve ultra-high power density while maintaining commercial battery equivalent energy densities. The combination of high energy and power density primary microbatteries may be attractive for many devices, including medical, military, and industrial devices that require smaller power sources, faster computation, stronger actuation, long-range telemetry or high current therapy modalities (*22*, *23*).

4.4 Methods

Microbattery Fabrication:

Figure 4.1c outlines the microbattery fabrication, which followed a similar procedure we developed for secondary microbatteries (*2*). First, an interdigitated gold pattern that defined the geometry for the microbattery electrodes was fabricated by sputtering 8 nm of chromium followed by 70 nm of gold on a 1 mm thick soda lime glass slide, and then patterned and etched via conventional lithographic processing. The interdigitated gold pattern had 5 mm long and 5 μm wide parallel rectangles, called fingers, connected to two perpendicular 4 mm wide contact pads such that every other finger was electrically connected through a contact pad and neighboring fingers were electrically isolated. The glass slide with gold pattern was then cut into smaller samples, piranha cleaned for ten minutes, immersed in ultrapure water with 3-mercapto-1-propanesulfonic acid, sodium salt (2.2 % by weight) for 3 hours and rinsed. Polystyrene (PS) opals were self-assembled onto the gold patterned substrate by first placing the substrate vertically in 1 inch diameter plastic container filled with a colloid solution of 500 nm in diameter PS spheres. The plastic container was then set on a hotplate at 55o C, covered, and left for 24 to 30 hours until the solution was dry. The substrate was then sintered at 96 °C for 5 hours, which increased the contact area between the PS spheres to about 200 nm in diameter. This contact area determines the diameter of the holes, or interconnects, between the 500 nm pores in the inverted nickel current collector. A larger interconnect diameter allows for more active material deposition before the interconnect holes are pinched closed, which prevents the transport of ions through the porous structure. The PS colloidal solution was made by combining 8 wt% PS sphere solution (1.2 grams), purchased from Invitrogen, with ultrapure water (40 grams). The porous, bicontinuous nickel current collectors for the cathode electrodes were fabricated by

electrodepositing nickel through the PS opal at a constant -1.8 volts versus nickel reference electrode for 12 minutes in Technic RTU Mechanical Agitation commercial plating solution. In this step, only the current collector for the cathode is electrodeposited by making electrical contact with the cathode contact pad. Nickel was then electroplated on the anode interdigitated pattern at -1.8 volts for 2 minutes to create a barrier between the gold and lithium that was later deposited, as lithium electrochemically alloys with gold at the lithium deposition voltage. PS was removed by immersing the substrates in a tetrahydrofuran bath for 24 hours followed by a tetrahydrofuran and toluene rinse. The resulting nickel current collectors provided the architecture for the microbattery. The cathode current collectors are typically 33 μm wide, 15 μm tall, and 87% porous, separated between 5 μm wide and less than 1 μm tall interdigitated anode current collectors.

Electrochemically Active Material Electrodeposition:

The cathode and anode electrochemically active materials were independently electrodeposited onto the electrically isolated nickel current collectors. The cathode current collector was first primed for manganese deposition by applying 15 cycles of 1.2 and -0.5 pulsed voltage vs. Ag/AgCl for 0.1 and 3.0 seconds in ultrapure water with manganese acetate tetrahydrate (0.1 M) and sodium sulfate (0.1 M) titrated to pH 5.5 using sulfuric acid. Manganese oxide was then deposited and partially stripped for 30 cycles by applying 0.6 volts vs. Ag/AgCl for 8 seconds followed by -0.95 and -0.8 volts for 2 seconds each, with a 25 second open circuit rest between each cycle. After deposition, the manganese oxide was electrochemically oxidized by holding the cathode at 1.1 V vs. Ag/AgCl for ten minutes in ultrapure water titrated to pH 3.5 using sulfuric acid.

A 1 mm thick polyethylene mask with acrylic adhesive and a 0.5 mm^2 through hole was placed on the microbattery substrate to enable precise measurement of the microbattery area after discharge. Only the electrodes beneath the through hole are exposed to the electrolyte. The substrate was preheated to 110 °C before the mask was added to improve the mask adhesion and prevent electrolyte from leaking to other areas of the electrodes. The microbattery substrate was moved to an argon filled glovebox. Lithium was then deposited onto the anode current collector at 0.75 mA cm^{-2} current density with $LiClO_4$ (1.0 M) and $CsPF_6$ (0.05 M) in 80% propylene carbonate (PC) solution with 20% vinylene carbonate based on a recipe from Ding et al. (*13*). The solution was made by first mixing $AgPF_6$ (0.05 M) with CsI (0.05 M) in PC (25 ml), and stirring for 12 hours in an argon filled glovebox. After mixing, AgI formed a yellow precipitate that was filtered out by running the solution through a 0.45 μm syringe filter. A piece of lithium was then inserted into the solution to react any excess silver ions followed by another filtration step. VC (5 ml) was then added along with $LiClO_4$ (1 M), after which the solution was filtered and ready for lithium deposition. The cycling efficiencies reported in Table 4.1 were determined by galvanostatically depositing lithium on a flat nickel substrate for set period of time, typically 1 hour, and then galvanostatically de-plating lithium at the same current density until the sample potential reached 0.2 volts versus lithium. The cycling efficiency was determined by dividing the coulombs de-plated by the total deposited coulombs. The reported numbers in Table 4.1 represent the best performance for each electrolyte.

Electrochemical characterization:

The completed microbatteries were galvanostatically discharged to 0.5 volts vs. a lithium reference at various current densities and pulsed sequences in 1:1 EC:DMC liquid electrolyte with 1 M $LiClO_4$. The energy and power density of the microbattery cells were calculated by

measuring the discharge voltage and current and normalizing the total energy and power to the volume of the microbattery cell, which includes the total volume occupied by the electrodes (anode, cathode, Ni current collector, and electrolyte in the porous 3D electrode) and the electrolyte in the separation between the electrodes. The volume was calculated by multiplying the height of the electrodes by the cell area, which was measured in a SEM.

4.5 References

1. V. Narain, "Global thin-film batteries (TFB) market" (Frost and Sullivan, 2013).
2. J. H. Pikul, H. Gang Zhang, J. Cho, P. V. Braun, W. P. King, High-power lithium ion microbatteries from interdigitated three-dimensional bicontinuous nanoporous electrodes. *Nat. Commun.* **4**, 1732 (2013).
3. H. Ning *et al.*, Holographic patterning of high-performance on-chip 3D lithium-ion microbatteries. *Proceedings of the National Academy of Sciences*, (May 11, 2015, 2015).
4. C. Liu *et al.*, An all-in-one nanopore battery array. *Nat Nano* **9**, 1031 (2014).
5. K. Yoshima, H. Munakata, K. Kanamura, Fabrication of micro lithium-ion battery with 3D anode and 3D cathode by using polymer wall. *J. Power Sources* **208**, 404 (2012).
6. K. Sun *et al.*, 3D Printing of Interdigitated Li-Ion Microbattery Architectures. *Advanced Materials* **25**, 4539 (2013).
7. W. Lai *et al.*, Ultrahigh-Energy-Density Microbatteries Enabled by New Electrode Architecture and Micropackaging Design. *Advanced Materials* **22**, E139 (2010).
8. S. R. Gowda, A. Leela Mohana Reddy, X. Zhan, P. M. Ajayan, Building Energy Storage Device on a Single Nanowire. *Nano Letters* **11**, 3329 (2011/08/10, 2011).
9. D. Golodnitsky *et al.*, Progress in three-dimensional (3D) Li-ion microbatteries. *Solid State Ionics* **177**, 2811 (Oct, 2006).
10. T. S. Arthur *et al.*, Three-dimensional electrodes and battery architectures. *MRS Bulletin* **36**, 523 (2011).
11. J. W. Long, B. Dunn, D. R. Rolison, H. S. White, Three-dimensional battery architectures. *Chemical Reviews* **104**, 4463 (Oct, 2004).
12. B. A. Boukamp, G. C. Lesh, R. A. Huggins, All-Solid Lithium Electrodes with Mixed-Conductor Matrix. *J. Electrochem. Soc.* **128**, 725 (1981).
13. F. Ding *et al.*, Dendrite-Free Lithium Deposition via Self-Healing Electrostatic Shield Mechanism. *J. Am. Chem. Soc.* **135**, 4450 (2013/03/20, 2013).
14. S.-i. Tobishima, T. Okada, Lithium cycling efficiency and conductivity for high dielectric solvent/low viscosity solvent mixed systems. *Electrochim. Acta* **30**, 1715 (1985).
15. G. Zheng *et al.*, Interconnected hollow carbon nanospheres for stable lithium metal anodes. *Nat Nano* **9**, 618 (2014).
16. H. Ota, K. Shima, M. Ue, J.-i. Yamaki, Effect of vinylene carbonate as additive to electrolyte for lithium metal anode. *Electrochim. Acta* **49**, 565 (2004).

17. Z. Tu, Y. Kambe, Y. Lu, L. A. Archer, Nanoporous Polymer-Ceramic Composite Electrolytes for Lithium Metal Batteries. *Adv. Energy Mater.* **4**, n/a (2014).
18. Y. Deng *et al.*, Porous Mn2O3 microsphere as a superior anode material for lithium ion batteries. *RSC Advances* **2**, 4645 (2012).
19. J. Gao, M. A. Lowe, H. D. Abruña, Spongelike Nanosized Mn3O4 as a High-Capacity Anode Material for Rechargeable Lithium Batteries. *Chem. Mater.* **23**, 3223 (2011/07/12, 2011).
20. L. Chang *et al.*, Pore-controlled synthesis of Mn2O3 microspheres for ultralong-life lithium storage electrode. *RSC Advances* **3**, 1947 (2013).
21. "World primary lithium battery market" (Frost and Sullivan, 2009).
22. G. Blomgren, Primary Batteries for Military Applications. *Encyclopedia of Applied Electrochemistry*, 1720 (2014).
23. P. A. Tamirisa, K. Chen, G. Jain, Primary Batteries for Medical Applications. *Encyclopedia of Applied Electrochemistry*, 1713 (2014).
24. C. C. Liang, J. Epstein, G. H. Boyle, A High-Voltage, Solid-State Battery System: II . Fabrication of Thin-Film Cells. *J. Electrochem. Soc.* **116**, 1452 (October 1, 1969, 1969).
25. A. Piqué, C. B. Arnold, H. Kim, M. Ollinger, T. E. Sutto, Rapid prototyping of micropower sources by laser direct-write. *Appl Phys A* **79**, 783 (2004/09/01, 2004).
26. C. B. Arnold, H. Kim, A. Piqué, Laser direct write of planar alkaline microbatteries. *Appl Phys A* **79**, 417 (2004/08/01, 2004).
27. F. Albano *et al.*, A fully integrated microbattery for an implantable microelectromechanical system. *J. Power Sources* **185**, 1524 (2008).
28. J. B. Bates, N. J. Dudney, B. Neudecker, A. Ueda, C. D. Evans, Thin-film lithium and lithium-ion batteries. *Solid State Ionics* **135**, 33 (2000).
29. P. H. Humble, J. N. Harb, R. LaFollette, Microscopic Nickel-Zinc Batteries for Use in Autonomous Microsystems. *J. Electrochem. Soc.* **148**, A1357 (December 1, 2001, 2001).
30. K. T. Braam, S. K. Volkman, V. Subramanian, Characterization and optimization of a printed, primary silver–zinc battery. *J. Power Sources* **199**, 367 (2012).
31. J. B. Goodenough, Y. Kim, Challenges for Rechargeable Li Batteries†. *Chem. Mater.* **22**, 587 (2010/02/09, 2009).
32. H. Zhang, X. Yu, P. V. Braun, Three-dimensional bicontinuous ultrafast-charge and -discharge bulk battery electrodes. *Nat. Nanotechnol.* **6**, 277 (2011).
33. P. V. Braun, J. Cho, J. H. Pikul, W. P. King, H. Zhang, High power rechargeable batteries. *Curr. Opin. Solid State Mater. Sci.* **16**, 186 (2012).
34. S. Wu *et al.*, Electrochemical Stability of Orthopedic Porous NiTi Shape Memory Alloys Treated by Different Surface Modification Techniques. *J. Electrochem. Soc.* **156**, C187 (June 1, 2009, 2009).
35. H. Wang *et al.*, Mn3O4−Graphene Hybrid as a High-Capacity Anode Material for Lithium Ion Batteries. *J. Am. Chem. Soc.* **132**, 13978 (2010/10/13, 2010).
36. M. Doyle, J. Newman, J. Reimers, A quick method of measuring the capacity versus discharge rate for a dual lithium-ion insertion cell undergoing cycling. *J. Power Sources* **52**, 211 (1994).

CHAPTER 5

MICROMECHANICAL DEVICES WITH CONTROLLABLE STIFFNESS FABRICATED FROM REGULAR POROUS CELLULAR SOLIDS*

5.1 Introduction

The hierarchical pore structure of solid foams allows for a large range of densities and material properties (*1*). Most solid foams have broad distribution of pore sizes, randomly-located pores, and irregular pore shapes that can be difficult to engineer (*2*). However recent advances in self-assembly processes have increasingly offered routes to regular foams with tightly controlled 3-D periodic structures (*3, 4*). The regular, ordered nature of these foams allows for new applications including miniature electrical and mechanical devices (*5, 6*). Additionally, regular microarchitectures that resemble foams have been used to demonstrate materials with exceptional strength to weight ratios, suggesting that regular macroporous foams could provide similar mechanical properties (*7*).

This chapter demonstrates microcantilevers fabricated from regular 3-D macroporous foams having a nickel inverse opal or alumina shell structure. The fabrication, based on an inverse-opal template process, offers 3-D spatial control of the ordered foams with unique geometries and composite materials not achievable by subtractive fabrication. The mechanical

---

properties of these devices depend upon the porosity, as expected, however the deformation modes are dramatically different, depending upon the micro-architecture. The Young's moduli of the microcantilevers ranged from 2.0 to 44.3 GPa, which are comparable to materials ranging in stiffness from Nylon to high strength concrete or magnesium. At a 0.15 solids volume fraction, the Young's moduli of the inverse opal and shell structures differ by a factor of 10.

5.2 Methods and Materials Architecture

Figure 5.1 shows the fabrication steps for the inverse opal nickel microcantilevers. First, 10 nm chromium and 50 nm gold layers were sputtered on a double-side polished silicon wafer and patterned to the microcantilever geometry by photolithography and gold/chromium etching. The wafers were then soaked in acetone, diced into 1 cm by 3 cm chips, and piranha cleaned. The chips were then immersed in Millipore water with 2.2 % by weight 3-mercapto-1-propanesulfonic acid, sodium salt for 3 hours. 1.8 ± 0.09 μm in diameter polystyrene opals, measured by transmission electron microscopy, were then self-assembled onto the chips by positioning the chips vertically in a colloidal solution made from 1.2 grams of 8 wt% PS sphere solution and 40 grams of Millipore water. The chips and solution were set on a hot plat at 50^{o} C, covered, and left for 24 to 30 hours. (*9*, *10*). During evaporation the spheres at the receding water-substrate meniscus are self-assembled onto the substrate into an opal. The substrates were then sintered at 95 °C for 4 hours. The resulting polystyrene opal is typically face centered cubic in structure. Nickel was electroplated through the polystyrene opal using a 10 mA/cm^2 current density in a commercial electrolyte of Nickel Sulfamate Semi-Bright RTU Mechanical Agitation by Technic. The deposited nickel had a measured Young's modulus of 174.3 ± 12.3 GPa, which is in good agreement with electrodeposited nickel having a <001> out-of-plane texture (*11*). The

polystyrene was removed with *tetrahydrofuran*, *resulting in an inverted opal structure*. The volume and surface area of a single pore in the inverse opal structure, including half the volume and area of the interconnects between pores, is approximately 4 μm^3 and 10 μm^2.

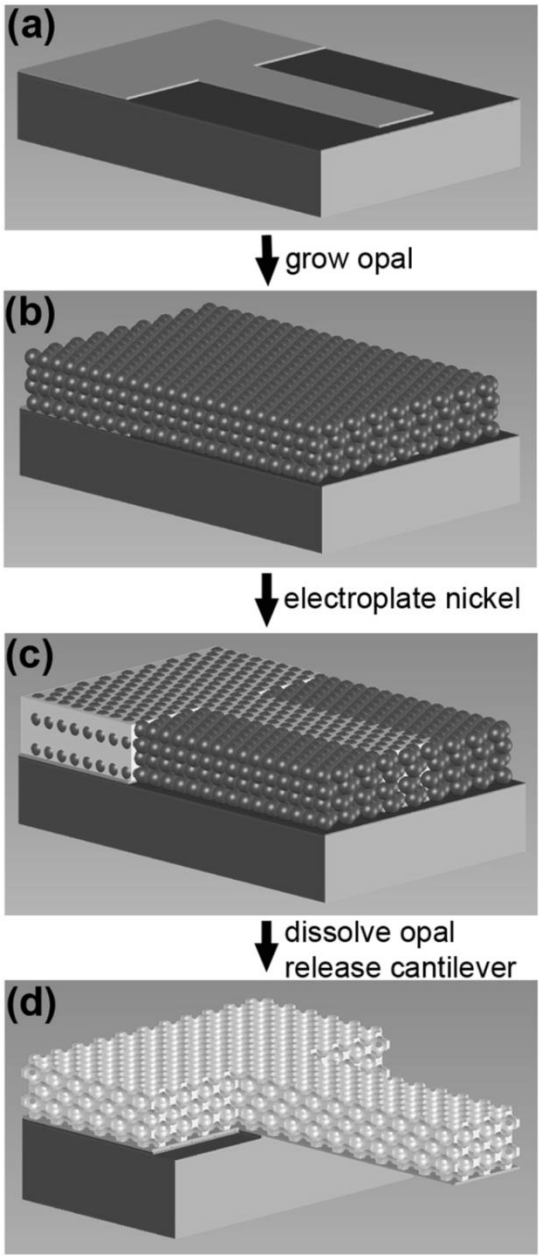

Figure 5.1: Fabrication process for a regular 3D macroporous nickel inverse opal microcantilever. (**a**) The fabrication starts with a gold template on a silicon wafer. (**b**) The

polystyrene colloidal scaffold is self-assembled on the substrate. (**c**) Nickel is electrodeposited though the polystyrene. (**d**) The polystyrene is removed and the microcantilever is released.

The microcantilevers were released by first spin coating both sides of the chip with an adhesion layer (AP 8000) at 3000 rpm and a thick photoresist layer (AZ 4620) at 1000 rpm for 40 seconds. The back side of the chip was then exposed under the mask aligner for 25 seconds and developed for 90 seconds. Freshly spun photoresist (AZ 4620, 1000 rpm) is used as an adhesive for manually attaching the chip to a carrier wafer, after the wafer was hardbaked at 110^{o}C on a hotplate for 10 minutes. The carrier wafer with the chip attached was then hard bake again at 110^{o}C for 10 minutes and 130^{o}C for another 10 minutes. The silicon substrate was etched through in a PlasmaTherm ICP with the Bosch process. The chip and the carrier wafer were separated in photoresist stripper (AZ400T) at 70^{o}C for 4 hours. Last, the silica layer under the microcantilever was removed by dipping the chip into 49% hydrofluoric acid for 20 seconds.

The template shape and additive chemistry can be changed to precisely engineer the hierarchical structure, making the template fabrication advantageous over subtractive techniques. Additionally, the size, shape, and thickness of the nickel inverse opal microcantilever can be readily adjusted by changing the lateral dimensions and geometry of the metal seed layer and the duration of nickel electrodeposition. The solids volume fraction of the nickel inverse opal microcantilevers is initially 0.25. The nickel can be isotropically etched to reduce the solids volume fraction to 0.15 by electropolishing the nickel structure (*10*). Electropolishing was performed using the Electro Polish Systems EPS1250 solution under a 4 volt pulsed deposition with 1 second on and 10 second rest times. Stainless steel was used as a reference and counter electrodes. The volume of active material removed can be precisely measured by the current and duration of etching. Figures 5.2a and 5.2d show SEM images of released nickel inverse opal microcantilevers. Figure 5.2b and 5.2c show the top surfaces of nickel inverse opal

microcantilevers with 0.25 and 0.15 volume fractions. Figures 5.2e and 5.2f show a composite bilayer microcantilever made of gold and nickel. The bimaterial structure was achieved by a second electrodeposition step before the polystyrene was etched. Figures 5.2g – 5.2i show the complex shapes that can be patterned using the template based fabrication process. The bottom up template fabrication process is advantageous for engineering miniature devices since the material properties can be precisely controlled by independently engineering the size and shape of the polystyrene template materials, the geometry of the patterned seed layer, and the chemical composition of the electrodeposited materials.

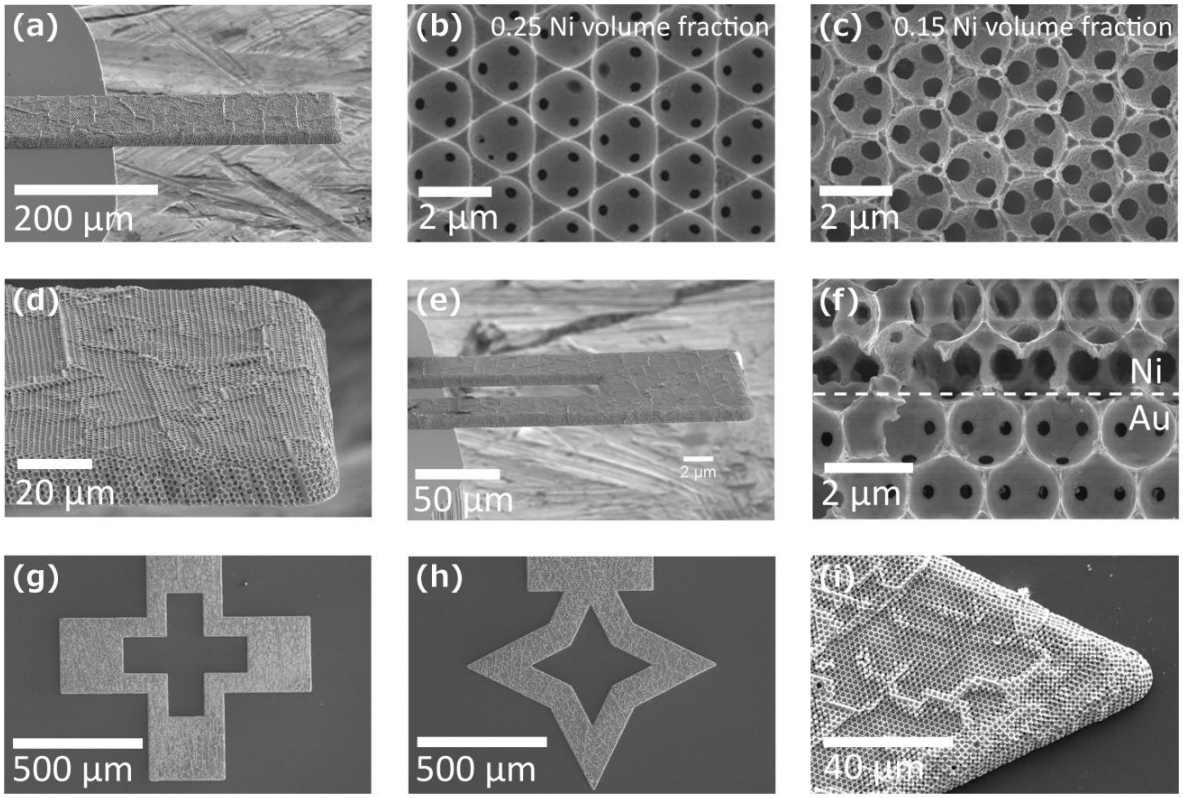

Figure 5.2: (**a**) Scanning electron microscopy (SEM) images of a microcantilever with a regular, porous inverse opal macrostructure. (**b**, **c**) Top view of nickel inverse opal microcantilevers with 0.25 and 0.15 volume fractions. (**d**) Close up of a microcantilever with a regular, porous inverse opal macrostructure. (**e**) A bimaterial microcantilever cantilever with a gold and nickel inverse opal composite microstructure. (**f**) A close up of the bimaterial cantilever in (**e**), where the

bottom layer is gold and the top layer is nickel that has been selectively electropolished. (**g**, **h**) Nickel inverse opal macrostructure patterned into complex shapes. (**i**) A close up of the star shape shown in (**h**).

Alumina based microcantilevers with a unique regular 3-D macroporous structure were formed by conformally coating the nickel inverse opal microcantilever with alumina followed by etching of the nickel, resulting in a shell structure. Figures 5.3a – 5.3c show the microfabrication process of a microcantilever with a shell structure. First, the nickel inverse opal microcantilever was coated with 75 nm thick amorphous alumina by atomic layer deposition (ALD). The alumina was deposited by first heating the sample chamber to 80° C. Trimethyl aluminum was pulsed into the chamber for 0.03 seconds, followed by vacuum pumping for 65 seconds. Water was then pulsed into the chamber for 0.03 seconds, followed by vacuum pumping for 65 seconds. This cycle was repeated 750 times for an average growth rate of 0.1 nm per cycle. The extreme conformality of the ALD-deposited alumina film allowed for an even coating throughout the 3D structure. Next, the edges of the microcantilever were cut with a focused ion beam (FIB) to expose the nickel. The microcantilever was then soaked in nickel etchant (Transene, type TFB) until only the alumina shell remained. For a 100 μm wide microcantilever, this typically takes 7 hours. Figure 4 shows the nickel etching process in the shell microcantilevers. The nickel can be etched in 7 hours. Figures 5.3d – 5.3f shows SEM images of a microcantilever with an alumina shell structure and magnified images of the cross-section. This approach is rather general, and could be applied for any material which can be conformally coated on the nickel structure.

The solids volume fraction of the microcantilevers is calculated using a geometric model of the microstructure unit cell (*10*). The solids volume fraction is the cubic unit cell volume, 16.5 μm^3, minus the volume occupied by the FCC ordered 1.8 ± 0.09 μm polystyrene spheres, about

12.4 μm^3. The electropolishing isotropically increases the void and interconnect volume. The change in the size of the interconnect diameters between pores was measured in a SEM and used to calculate the increase in pore volume due to etching. The interconnect diameters for un-etched nickel inverse opal microcantilevers were 190 nm with a 6% standard deviation, corresponding to a 0.2% difference in nickel volume calculated. Additionally, the volume of the alumina in the alumna shell structures can be calculated by assuming a uniform thickness deposited on to the nickel inverse opal structure. The thickness of the alumina was measured in a SEM. Cracks and vacancy defects in the opal can contribute to error between the predicted volume fraction and actual volume fraction. Samples with visible defects had 1 – 5 μm wide cracks in the polystyrene opal, which after nickel electrodeposition increase the nickel volume fraction over the volume predicted from the model by up to 3%. In the presence of defects the model over predicts the volume fraction of the alumina shell structure and under predicts the volume fraction of the nickel inverse opal structure. The model shows that the solids volume fraction can be theoretically as low as 0.05 by using 20 nm coatings of alumina, instead of the 75 nm coating used in this work.

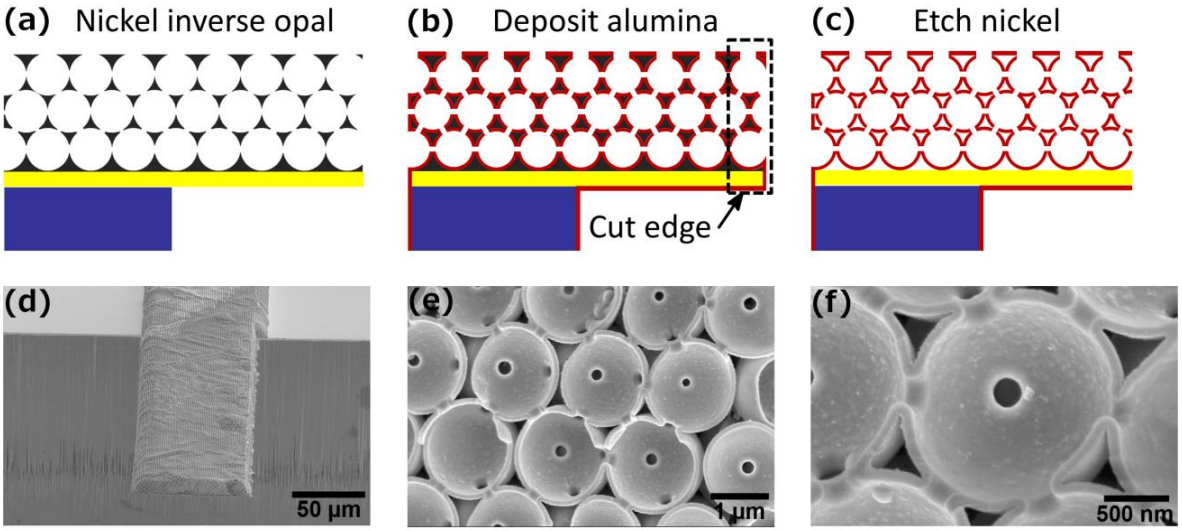

Figure 5.3: (**a** – **c**) Fabrication process of the alumina shell microcantilever. 75 nm of alumina is atomic layer deposited on a nickel inverse opal microcantilever. The edge is cut and the nickel etched. (**d** – **f**) Scanning electron microscopy images of an alumina shell microcantilever.

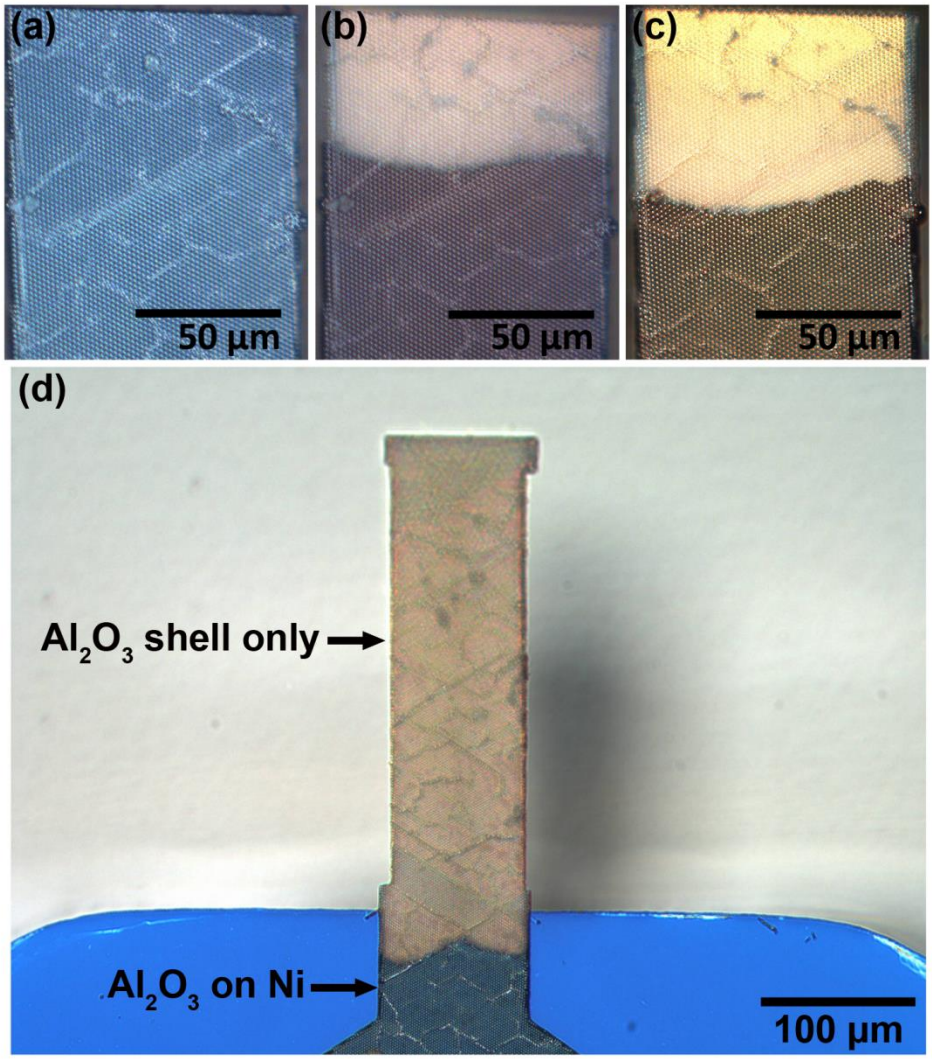

Figure 5.4: (**a**) Optical image of a cantilever with nickel inverse opal microstructure coated with 75 nm alumina. The free end edge is cut off by a focused ion beam (FIB) to expose the nickel. (**b**), (**c**) Optical images of the same device after being soaked in nickel etchant for 18 hr and 24 hr. (**d**) Optical image of another device with all three edges cut off by a FIB and soaked in nickel etchant for 7 hr. The nickel in the free standing cantilever is completely removed.

We characterized mechanical properties of the nickel inverse opal and alumina shell microcantilevers. Devices with stiffness greater than 1 N/m were measured in an Agilent Nanoindenter (MT200), while softer microcantilevers were measured in an atomic force microscope (AFM) (Asylum MFP3D) using the Sader method (*12*). Figure 5a shows the load versus displacement measurements of a nickel inverse opal microcantilever deflected at 30, 80,

130, and 160 μm from the microcantilever end in the nanoindenter. The stiffness of the microcantilever is the slope of the load versus displacement curve at each location. The spring constant was found by fitting the load versus displacement data with a $1/L^3$ fit, since stiffness is proportional to $1/L^3$. The stiffness at the end of the microcantilever, $L/L_o = 1$, is the spring constant of the full microcantilever. The Young's moduli, E, of the microcantilevers were calculated from the spring constant and geometry using $E=4kL^3/Wt^3$, where k is the spring constant, L, W and t are the length, width and thickness of the microcantilever (*13-15*). The length, width, and thickness were measured in a SEM. Additionally, the Young's moduli calculations are sensitive to errors in the length and thickness measurements because of the 3rd power dependence. Figure 5.5c shows the thermal spectrum for an inverse opal microcantilever. The thermal spectrum shows the frequency dependent motion of the cantilever due to the Brownian motion of atoms. The cantilever geometry constrains the cantilever to vibrate the most intense at its resonant frequency, which is detected by a large peak in the thermal spectrum. Figure 5.5d shows the resonant frequency versus spring constant for the inverse opal and shell microcantilevers, along with a silicon microcantilever for reference.

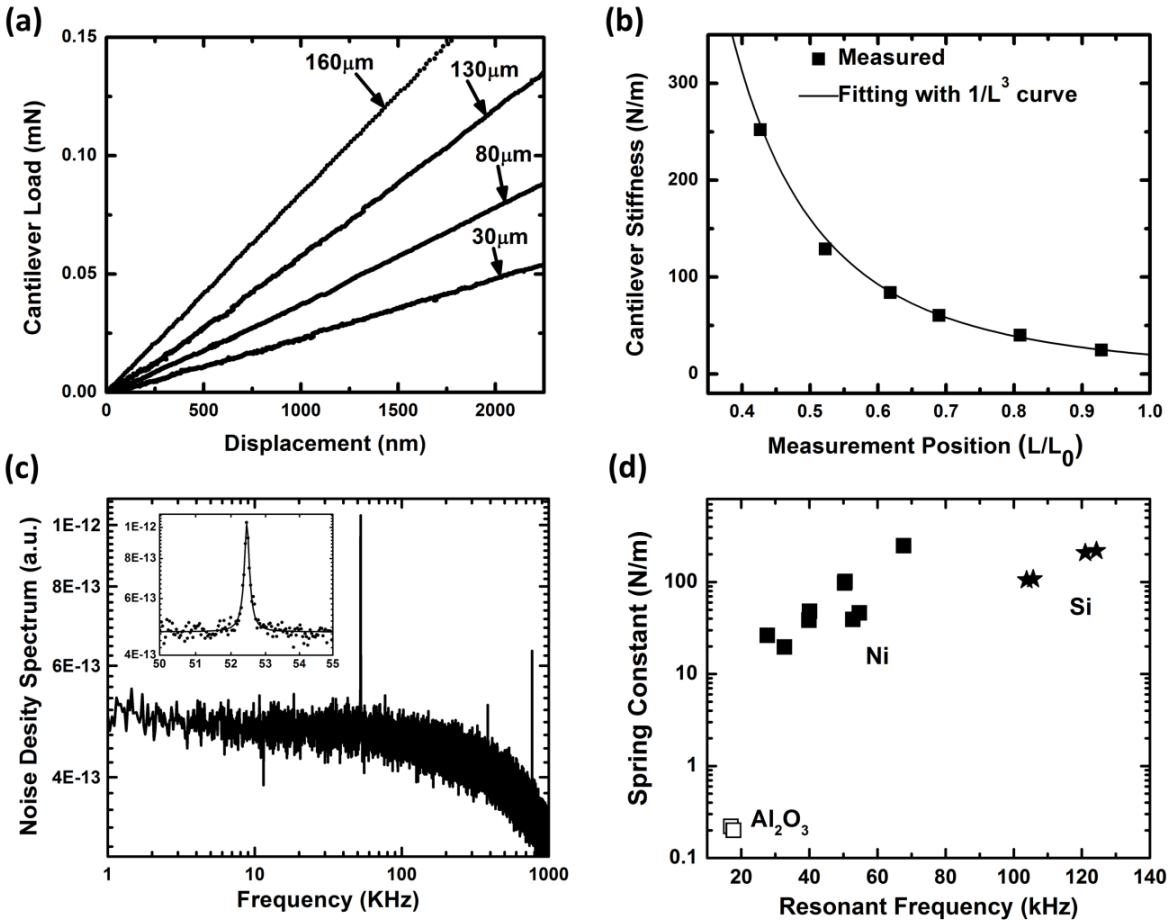

Figure 5.5: Measured mechanical properties of inverse opal and alumina shell microcantilevers. The nickel inverse opal microcantilevers had an average length, width, and thickness of 380, 180, and 11 μm. The alumina shell microcantilevers had 321, 95, and 5 μm average dimensions. (**a**) Load versus displacement measurements of a 0.15 solids volume fraction nickel inverse opal microcantilever deflected at 30, 80, 130, and 160 μm from the microcantilever end. (**b**) The stiffness at each location on the microcantilever with a $1/L^3$ fit. (**c**) The thermal spectrum of a 0.15 solids volume fraction nickel inverse opal microcantilever used to measure the resonance frequency. (**d**) The spring constant versus resonant frequency for the alumina shell and nickel inverse opal microcantilevers. Data from a silicon cantilever is used as a reference.

Table 5.1. Mechanical properties of microcantilevers with different volume fractions.

Material	Volume Fraction	Length (μm)	Width (μm)	Thickness (μm)	Spring Constant (N/m)	Resonant Frequency (kHz)	Quality Factor	Young's Modulus (GPa)
Ni	1	330.1	202.5	9.8	247.2	67.7	442	186.6
Ni	1	375.3	128.3	10.0	101.3	50.5	440	166.9
Ni	1	374.7	128.3	9.8	97.3	50.4	518	169.5
Ni	0.25	399.7	221.9	10.8	47.9	40.1	412	43.8
Ni	0.25	310.4	136.1	9.7	46.0	54.7	658	44.3
Ni	0.22	363.1	224.6	10.9	38.4	39.9	365	25.3
Ni	0.22	459.7	218.3	11.9	26.3	27.7	427	27.8
Ni	0.15	387.9	215.6	13.0	39.1	52.8	383	19.3
Ni	0.15	418.7	141.4	12.6	19.6	32.7	426	20.3
Al_2O_3	0.16	327.9	97.8	4.6	0.22	17.0	60	3.3
Al_2O_3	0.16	319.5	92.3	5.2	0.20	17.7	46	2.0
Al_2O_3	0.16	316.0	93.3	4.8	0.20	17.8	43	2.4
Si	1	345.0	119.3	9.9	105.0	103.8	870	149.0
Si	1	342.6	119.9	9.9	107.9	105.7	830	149.2
Si	1	313.5	191.8	9.8	218.9	124.3	461	149.4
Si	1	318.3	192.4	9.8	208.1	121.0	445	148.2

5.3 Results and Discussion

The Young's moduli of the nickel inverse opal and alumina shell microcantilevers can be tuned by controlling the porosity, however, the different micro architecture leads to dramatically different Young's moduli. Figures 5.6a and 5.6b show the Young's moduli of nickel inverse opal and alumina shell microcantilevers with different volume fractions and densities. Table 5.1 shows detailed measurements of each cantilever. The Young's moduli of the nickel inverse opal microcantilevers with 0.15 – 0.25 solids volume fraction ranged between 19.3 and 44.3 GPa, as compared to the 174 GPa average Young's modulus measured from fabricated non-porous nickel microcantilevers. The Young's moduli of the nickel inverse opal microcantilevers can be tuned by controlling the porosity through etching. The alumina shell microcantilevers were fabricated from ALD alumina, which has a 172 GPa average Young's modulus (*16*). The Young's moduli of the three alumina shell microcantilevers with 0.16 solids volume fractions varied between 2.0 and 3.3 GPa, which is 10X lower than the nickel inverse opal microcantilevers despite having similar volume fractions of 0.16 and 0.15 and similar bulk material Young's moduli.

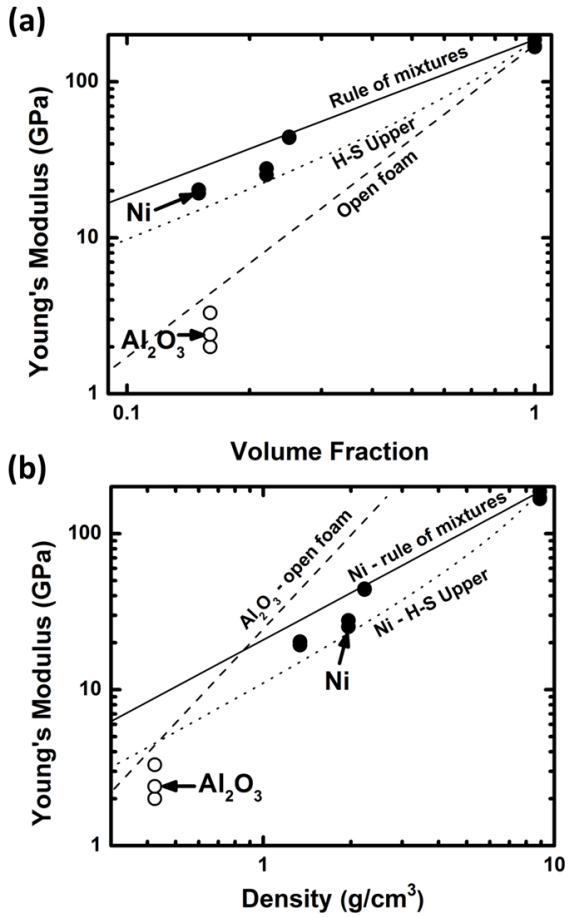

Figure 5.6: (**a**) The Young's moduli of the various microcantilevers with different volume fractions. The nickel inverse opal data lies between the Hashin – Shtrikman upper bound for isotropic materials and the limit set by the rule of mixtures. (**b**) The Young's moduli of the various microcantilevers versus density. The alumina shell structure has a density and Young's modulus of 0.4 g cm^{-3} and 2 – 3.3 GPa.

The nickel inverse opal devices and the alumina shell devices have different micro architectures that lead to different deformation modes and ultimately different mechanical properties. The nickel inverse opal architecture has solid struts in between large interconnected spherical pores. The alumina shell architecture is based on the same geometry but composed of thin walls surrounding the interconnected spherical pores. The hierarchical structure of the alumina shell microcantilevers changes the deformation mode of the microcantilevers despite

having similar pore size and strut width as the inverse opal architecture. Most foam-like and cellular porous materials deform by bending, as opposed to stretching, of the internal nodes or connections between nodes, which causes these materials to be pliant (*17*). The Young's modulus, *E*, can be related to the solids volume fraction, ε, and non-porous modulus, E_o, by $E/E_o \approx A\varepsilon^n$, where *A* is a constant that depends on the material pore structure. The exponent *n* is dependent on the degree of stretching versus bending deformation, and is near 1 for stretching-dominated deformation and near 2 for bending-dominated deformation (*18*). The maximum Young's modulus a porous material can achieve is given by the rule of mixtures, where $A = 1$ and $n = 1$. Considerable work has gone into designing materials with architectures that maximize the Young's modulus (*19, 20*), with the most studied materials having a tetrahedral or octet truss core structure (*18, 21-23*). These isotropic micro architectures are limited by the Hashin – Shtrikman (H.-S.) bounds for isotropic materials, which is lower than the rule of mixtures limit (*24*). The upper Hashin – Shtrikman bounds for the bulk modulus, *K*, and shear modulus, *G*, are the following, where subscripts 1 and 2 denote the bulk property for the first and second phase in the composite:

$$K_{upper} = K_2 + \frac{\varepsilon_1}{\frac{1}{K_1 - K_2} + \frac{\varepsilon_2}{K_2 + \frac{4}{3}G_2}}, \tag{5.1}$$

$$G_{upper} = G_2 + \frac{\varepsilon_1}{\frac{1}{G_1 - G_2} + \frac{2\varepsilon_2(K_2 + 2G_2)}{5G_2(K_2 + \frac{4}{3}G_2)}}. \tag{5.2}$$

Phase 1 is air for a porous media, so G_1 and K_1 are assumed to be zero and ε_1 is the material porosity. The Young's Modulus can be related by $E = 9KG/(3K + G)$ [19]. The relationship between the Young's modulus and porosity can be dramatically changed by engineering the isotropy and deformation modes of the micro architecture.

From figure 5.6, the Young's moduli of the nickel inverse opal microcantilevers lie between the Hashin – Shtrikman bounds and the rule of mixtures limit, which is comparable to non-isotropic materials that primarily deform elastically. The inverse opal microcantilevers at 0.25 volume fraction have a Young's moduli that are on average 17.5 GPa above the H.-S. bound. At the 0.15 and 0.22 volume fractions the Young's moduli are 3.6 and 4.8 GPa over the H.-S. bound. The Young's moduli of the lower volume fraction devices, achieved by etching the inverse opal, are closer to the H.-S. bound, possibly because the material is more isotropic or, by narrowing the struts, more deformation by bending is initiated. Defects and grains present in the opal structure could influence the Young's moduli of the microcantilevers by causing the microcantilevers to stiffen favorably in a direction or to deform more isotropically. At larger strains the inverse opal might deform primarily by bending and lose the properties it shows at small strains, since the inverse opal structure does not satisfy the Maxwell criteria for elastic deformation.

The alumina shell microcantilevers, by contrast, are very pliant and have Young's moduli below the modulus predicted for an open cell foam structure. The Young's moduli of an open cell foam depends on the volume fraction by $E = \varepsilon^2$ due to the bending-dominated deformation. The Young's moduli of the alumina shell microcantilevers are 2 – 3.3 GPa at 0.16 volume fractions, or 0.4 g cm^{-3} assuming a 2.65 g cm^{-3} density for ALD alumina deposited at 80°C (*25*). The lower Young's moduli than predicted by the open cell foam might be due to local cracking or buckling of the hollow nodes between pores. The alumina shell structure has a Young's modulus similar to a polymer such as Nylon, but with half the density of most polymers. The material in the shell structure could be easily changed to attain higher melting temperatures or different electrical/thermal conductivity compared to polymers. Previous publications that report

simulations of FCC foams similar to the alumina shell structure (*19, 20, 26*) predict both a high bulk modulus and $E = 0.72\varepsilon^{1.13}$ Young's modulus dependence on volume fraction. The primary difference between the shell structure and simulated foams is the interconnection between the spherical shells, which must induce the shell structure to undergo bending dominated deformation. The low Young's moduli of the alumina shell microcantilevers demonstrate that slight changes in the micro architecture can lead to dramatic changes in the mechanical properties of the bulk material.

5.4 Conclusion

In conclusion, microcantilevers with an inverse opal and shell micro architecture were fabricated. These micro architectures are regular, periodic and can be fabricated with a wide variety of materials, demonstrated here with nickel and alumina. The micro architecture and solids volume fraction of the microcantilevers were engineered to allow for broad control of the Young's modulus between 1.3 and 25% of the material's bulk Young's moduli. The different deformation modes in the micro architectures were found to have the largest impact on the mechanical properties.

Micromechanical devices are being developed with increasingly more complicated designs and under more harsh environmental conditions. The small selections of materials that are easy to fabricate limit the applications of micromechanical devices. The hierarchical structure of the inverse opal and shell microcantilevers is advantageous in addressing the challenges of advanced micromechanical devices because of the strict engineering control of the mechanical properties and device geometry that can be afforded while retaining the chemical, electrical, or physical properties of the structural materials. The isotropy of the inverse opal lattice could be

engineered by changing the geometry of the polystyrene opals, from spherical to rods for example, or by layering multiple materials within the microarchitecture such that each material contributes to the mechanical properties in different deformation directions. Regular mesoporous microcantilevers with inverse opal and shell micro architectures could enable new micromechanical devices with unique and highly controllable mechanical properties, for example micromechanical sensors (*27*), flexible batteries (*5*), or chemical sensors (*6*).

5.5 References

1. M. F. Ashby, The properties of foams and lattices. *Philosophical Transactions of the Royal Society A: Mathematical, Physical and Engineering Sciences* **364**, 15 (January 15, 2006, 2006).
2. J. Banhart, Manufacture, characterisation and application of cellular metals and metal foams. *Progress in Materials Science* **46**, 559 (2001).
3. A. H. Lu, F. Schüth, Nanocasting: A Versatile Strategy for Creating Nanostructured Porous Materials. *Advanced Materials* **18**, 1793 (2006).
4. M. Fu *et al.*, Anisotropic colloidal templating of 3D ceramic, semiconducting, metallic and polymeric Architectures. *Advanced Materials*, (Forthcoming 2014).
5. J. H. Pikul, H. Gang Zhang, J. Cho, P. V. Braun, W. P. King, High-power lithium ion microbatteries from interdigitated three-dimensional bicontinuous nanoporous electrodes. *Nat. Commun.* **4**, 1732 (2013).
6. X. You, J. H. Pikul, W. P. King, J. J. Pak, Zinc oxide inverse opal enzymatic biosensor. *Appl. Phys. Lett.* **102**, 253103 (2013).
7. J. Bauer, S. Hengsbach, I. Tesari, R. Schwaiger, O. Kraft, High-strength cellular ceramic composites with 3D microarchitecture. *Proceedings of the National Academy of Sciences*, (February 3, 2014, 2014).
8. H. P. James *et al.*, Micromechanical devices with controllable stiffness fabricated from regular 3D porous materials. *Journal of Micromechanics and Microengineering* **24**, 105006 (2014).
9. N. D. Denkov *et al.*, 2-Dimensional Crystallization. *Nature* **361**, 26 (Jan, 1993).
10. X. Yu, Y. J. Lee, R. Furstenberg, J. O. White, P. V. Braun, Filling Fraction Dependent Properties of Inverse Opal Metallic Photonic Crystals. *Advanced Materials* **19**, 1689 (2007).
11. K. J. Hemker, H. Last, Microsample tensile testing of LIGA nickel for MEMS applications. *Materials Science and Engineering: A* **319–321**, 882 (2001).
12. J. E. Sader, J. W. M. Chon, P. Mulvaney, Calibration of rectangular atomic force microscope cantilevers. *Review of Scientific Instruments* **70**, 3967 (1999).

13. J. P. Cleveland, S. Manne, D. Bocek, P. K. Hansma, A nondestructive method for determining the spring constant of cantilevers for scanning force microscopy. *Review of Scientific Instruments* **64**, 403 (1993).
14. X. Li, T. Ono, Y. Wang, M. Esashi, Ultrathin single-crystalline-silicon cantilever resonators: Fabrication technology and significant specimen size effect on Young's modulus. *Appl. Phys. Lett.* **83**, 3081 (2003).
15. T. Akihiro, S. Minoru, H. Kazuhiro, O. Shigeru, A method for determining the spring constant of cantilevers for atomic force microscopy. *Measurement Science and Technology* **7**, 179 (1996).
16. M. K. Tripp *et al.*, The mechanical properties of atomic layer deposited alumina for use in micro- and nano-electromechanical systems. *Sensors and Actuators A: Physical* **130–131**, 419 (2006).
17. V. S. Deshpande, M. F. Ashby, N. A. Fleck, Foam topology: bending versus stretching dominated architectures. *Acta Materialia* **49**, 1035 (2001).
18. L. J. Gibson, M. F. Ashby, *Cellular Solids : Structure and Properties*. (Cambridge University Press, Cambridge, ed. Second, 1997).
19. O. Sigmund, A new class of extremal composites. *Journal of the Mechanics and Physics of Solids* **48**, 397 (2000).
20. X. Huang, A. Radman, Y. M. Xie, Topological design of microstructures of cellular materials for maximum bulk or shear modulus. *Computational Materials Science* **50**, 1861 (2011).
21. D. J. Sypeck, H. N. G. Wadley, Cellular Metal Truss Core Sandwich Structures. *Adv. Eng. Mater.* **4**, 759 (2002).
22. H. N. G. Wadley, N. A. Fleck, A. G. Evans, Fabrication and structural performance of periodic cellular metal sandwich structures. *Compos. Sci. Technol.* **63**, 2331 (Dec, 2003).
23. V. S. Deshpande, N. A. Fleck, M. F. Ashby, Effective properties of the octet-truss lattice material. *Journal of the Mechanics and Physics of Solids* **49**, 1747 (2001).
24. Z. Hashin, S. Shtrikman, A variational approach to the theory of the elastic behaviour of multiphase materials. *Journal of the Mechanics and Physics of Solids* **11**, 127 (1963).
25. M. D. Groner, F. H. Fabreguette, J. W. Elam, S. M. George, Low-Temperature Al2O3 Atomic Layer Deposition. *Chem. Mater.* **16**, 639 (2004/02/01, 2004).
26. W. S. Sanders, L. J. Gibson, Mechanics of BCC and FCC hollow-sphere foams. *Materials Science and Engineering: A* **352**, 150 (2003).
27. B. Kwon, M. Rosenberger, R. Bhargava, D. G. Cahill, W. P. King, Dynamic thermomechanical response of bimaterial microcantilevers to periodic heating by infrared radiation. *Review of Scientific Instruments* **83**, (2012).

CHAPTER 6

SELF-ASSEMBLED LARGE AREA CELLULAR SOLIDS WITH ULTRA-HIGH STRENGTH MESOSCALE STRUTS AND CONTROLLABLE STIFFNESS

6.1 Introduction

Materials with continuous nano to microscale hierarchy have the potential to reshape our world by replacing structural materials, such as steel or titanium, with nanoscale cellular solids that have strengths approaching their theoretical yield strength, suppress brittle failure, and allow broad chemical functionality (*1-6*). In nanoscale cellular solids, reducing the characteristic lengths of struts or pore walls changes the dynamics of plasticity and improves strength by taking advantage of size based effects (*1, 2, 7, 8*). For example, dislocation starvation in sub-μm diameter pillars enables size based strengthening so that the pillar strength approaches the theoretical strength of the constituent material, which can be greater than ten times the bulk material strength (*1, 9-12*). The mechanical advantages of nanoscale confinement provide strong motivation for finding ways to scale the manufacturing of high strength nanoscale cellular solids so that they can be integrated and tested in engineered devices; however, the lack of fabrication technologies that can control nanoscale structure and chemistry over large areas has so far limited the nanoscale cellular solids to $< 5\ mm^2$ areas (*2, 3, 13-17*).

Most nanoscale cellular solids are fabricated from optical based techniques like two-photon lithography, three-dimensional (3-D) direct laser writing, and microstereolithography (*2,*

13-18). These optical techniques are serial, suffering from long processing times and small volumes, or when scalable suffer from low solid volume fractions and a lack of nm-level control over structural dimensions. Despite displaying several unique mechanical properties, the specific strengths of cellular solids fabricated from optical techniques, even with octet-truss architecture, vary between 20 – 140 MPa / (Mg/m^3), with most having lower specific strength than polymers like PMMA and nylon (*2, 3, 17*). Electrochemical de-alloying of gold-silver alloys is an alternative approach to achieve samples of nanoporous gold larger than mm^2; however, the high cost of raw materials and low specific strength, 16 MPa / (Mg/m^3), severely limits its applications (*7, 11, 19-22*). Self-assembly based techniques have the potential to provide nm-level control over structure and chemistry while being scalable to areas on the order of cm^2 and larger (*4, 23-26*). Inverse opals, fabricated from the self-assembly of spherical particles, have been integrated with may materials to enable high performance optical devices (*27*), batteries (*28, 29*), and sensors (*30, 31*); however their mechanical properties are not well known. A relationship between hardness and sub-μm pore sizes has been demonstrated in inverse opals, but detailed analysis and strength measurements were not provided (*32*). Recently, inverse opals made from SiO_2 and TiO_2 have demonstrated high specific strengths between 145 and 369 MPa / (Mg/m^3) (*33*). The combination of high strength, broad materials availability, and scalable fabrication make inverse opal based cellular solids a promising platform for fabricating the next generation of high strength multi-functional structural materials.

In this chapter we present nickel and rhenium nanocomposite inverse opal cellular solids with controllable specific moduli between 4 and 20 GPa / (Mg/m^3) and specific strengths up to 230 MPa / (Mg/m^3), which is greater than most high strength alloys including 4143 steel and Ti-6Al-4V. The inverse opal cellular solids are fabricated over 2 cm^2 areas and made flexible or

rigid based on the underlying substrate. Finite element simulations combined with nanoindentation and micropillar compression tests relate the nanoarchitecture to the bulk strength and stiffness. The yield strengths of the nanoscale struts that connect the inverse opal architecture increase from 3.57 GPa to 10.00 GPa when the effective strut diameter decreases from 115 nm to 17 nm. The combination of self-assembly and near room temperature electrodeposition allow for scalable fabrication of the cellular solids with high specific strength and down to 10 nm control of structure and chemistry.

6.2 Results and Discussion

Figure 6.1a shows the fabrication of a unit cell of the inverse opal cellular solid used in this study. First, monodisperse polystyrene (PS) particles of diameter 260 – 930 nm are self-assembled onto a gold/chromium coated substrate in a face centered cubic (FCC) orientation. The PS is sintered at 96 ºC to improve stability and increase the interconnect diameter between PS spheres. Nickel is then electrodeposited into the voids of the PS structure, followed by PS etching in tetrahydrofuran. The result is an open cell nickel cellular solid characterized by interconnected spherical pores arranged in a FCC orientation. Rhenium-nickel alloy (80 wt% rhenium) and nickel are conformally electrodeposited onto the cellular solid to increase the solid volume fraction, strut diameter, and mass. In addition, the rhenium-nickel coating demonstrates the ability to fabricate composite cellular solids with multiple materials. Figures 6.1b – 6.1g show SEM images of nickel cellular solids with 500 nm pores fractured on the (111) plane. Figures 6.1b and 6.1c are nickel cellular solids with no coating and a solid volume fraction of 0.16. Figures 6.1d and 6.1e show a nickel cellular solid uniformly coated with additional nickel of 19 nm average thickness. The coating increases the solids volume fraction from 0.16 to 0.35.

Figures 6.1f and 6.1g show a nickel cellular solid uniformly coated with additional rhenium-nickel alloy of 25 nm average thickness. The coating increases the solids volume fraction to 0.46. Figure 6.1h shows a 2 cm^2 nickel cellular solid with 500 nm pores and 15 μm thickness grown on a gold/chromium coated glass slide. Figure 6.1i shows a nickel cellular solid with 300 nm pores grown on gold/chromium-coated polyimide with 20 μm thickness. The nickel cellular solid on polyimide is flexible and can be bent past a 0.5 cm radius. Inverse opal cellular solids can act as photonic crystals and the colors in Fig. 6.1i are structural coloration. The self-assembly technique presented here allows the fabrication of cellular solids with larger than cm^2 areas, while retaining the ≈10 nm control of structure and chemistry.

The specific strength of inverse opal cellular solids results from the combination of two mechanical processes: porosity based weakening (size independent) and size based strengthening of the pore struts (nanoscale). Porosity based weakening is the reduction in load that a cellular solid can support due to reduced volume fraction of solid material and mediated by bending dominated deformation of cellular solid struts (*34*). Size based strengthening increases the local strength of the cellular solid constituent material because of dislocation starvation in < 1 μm strut widths (*1, 9-11*). The macroscopic cellular solid yield strength, σ^*, is related to the relative density (ρ^*/ρ_s) and strut yield stress, σ_y, by

$$\sigma^* = C_1\, \sigma_y(d)\, \left(\frac{\rho^*}{\rho_s}\right)^{C_2}, \tag{6.1}$$

where σ_y can be greater than the strength due to size based strengthening and depends on the strut effective diameter, *d* (*21, 34*). C_1 and C_2 are constants unique to the geometry of the inverse opal and independent of pore size or constituent material. If C_1 and C_2 are known, the size based

strengthening effect, $\sigma_y(d)$, can be determined by measuring σ^* for cellular solids with varying d and (ρ^*/ρ_s).

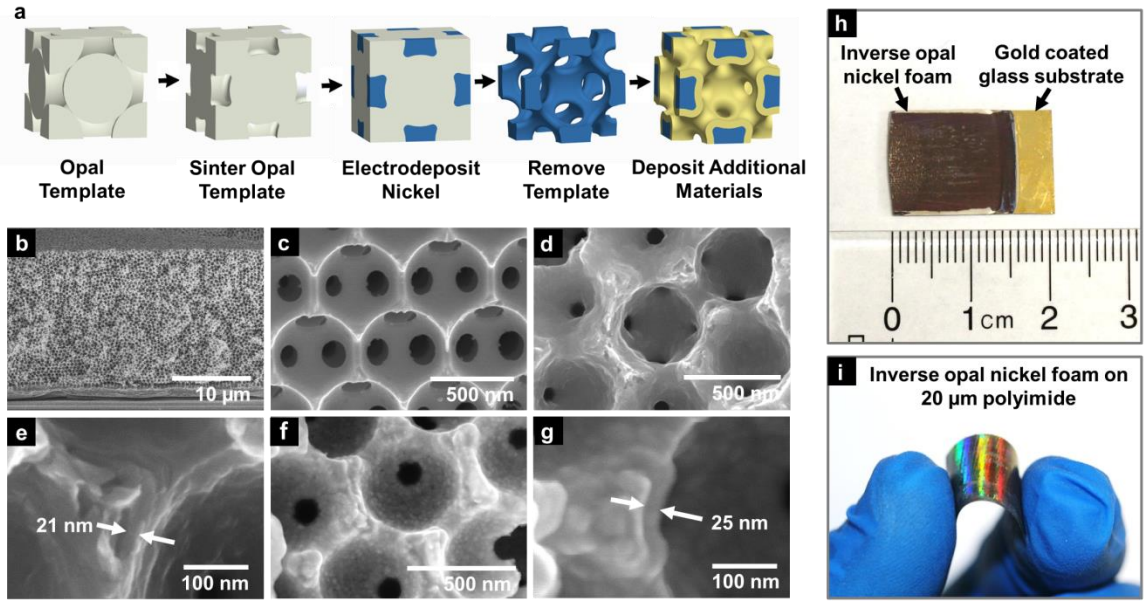

Figure 6.1: (**a**) The fabrication process for a unit cell of the cellular solid. (**b**-**g**) Cross section SEM images of nickel cellular solids used for mechanical testing. (**b**-**c**) A nickel inverse opal with no coating. (**d**-**e**) A nickel inverse opal with 19 nm of additional nickel electrodeposited. (**f**) A nickel inverse opal with 25 nm of additional rhenium-nickel electrodeposited. (**g**) A closer image of one of the struts in (f). (**h**) A 2 cm^2 nickel cellular solid with 500 nm pores and 15 µm thickness grown on a gold/chromium coated glass slide. (**i**) A nickel cellular solid with 300 nm pores grown on gold/chromium coated 20 µm thick polyimide.

Simulations of the cellular solid plastic deformation under uniaxial stress produce solutions for C_1 and C_2 by relating the cellular solid strength, σ^*, to variations in the relative density, (ρ^*/ρ_s). Figure 6.2a shows repeat cells of the cellular solids used in the finite element simulations. The relative density is varied by adding thin coatings to the cellular solid structure, as done experimentally. The colors in Fig. 6.2a correspond to Von Mises stresses after 0.012 strains. The maximum stress occurs in the narrow region of the struts parallel to the displacement

direction. Figure 6.2b shows corresponding stress-strain curves for the cellular solids with multiple coating thicknesses. The initial linear stress-strain relationship provides the elastic modulus of the cellular structure and yield strength is calculated by the 0.2% offset method. From these results, the cellular solid yield stress is related to the relative density by

$$\sigma^* = 1.06\,\sigma_y \left(\frac{\rho^*}{\rho_s}\right)^{1.73}. \tag{6.2}$$

The cellular solid elastic modulus, E^*, is related to the relative density and nickel elastic modulus, E, by

$$E^* = 1.19\,E \left(\frac{\rho^*}{\rho_s}\right)^{1.70}. \tag{6.3}$$

The polynomial relationship between the mechanical properties and relative density shows that the cellular solid deforms primarily through bending (*6*). Bending dominated deformation occurs in structures that do not satisfy the Maxwell criterion, which is the case for the inverse opal unit cell with 32 struts that connect 21 joints (*35*). The relationships in equation 6.2 and 6.3 are specific to the inverse opal geometry and valid for coated and un-coated inverse opals made from any one material. The simulation results are verified by measuring the elastic moduli of inverse opal cellular solids by nanoindentation and micropillar compression tests, and compared to the elastic modulus of 171 GPa for the electrodeposited solid nickel. The moduli measured during loading in micropillar compression tests are within 1 - 25% error of the moduli calculated by Equation 6.3, which shows good agreement between simulation and experiment considering the errors in strength and volume fraction measurements. The micropillar unloading moduli are 2 – 5X greater than the loading moduli and are similar to moduli measured with nanoindentation. The unloading and nanoindentation moduli are expected to be higher because they measure the

stiffness of already deformed cellular solids, which have a higher relative density. Table 6.1 shows the elastic moduli of nickel and rhenium-nickel coated nickel cellular solids. Equation 6.2 decouples the nanoscale strength enhancement from the porosity based weakening in the inverse opal cellular solids.

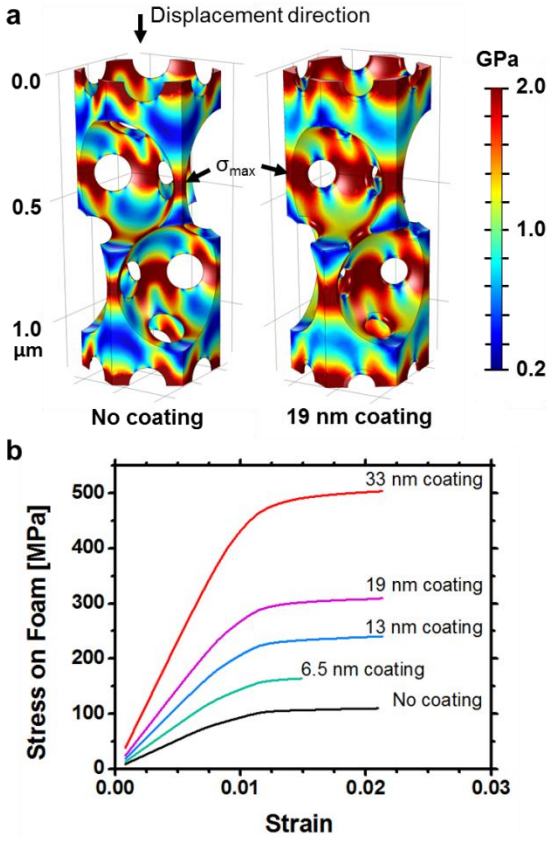

Figure 6.2: (**a**) Repeat cells of the inverse opal cellular solid used to determine the yield strength and elastic modulus through finite element simulations. The colors correspond to Von Mises stress at a 15 nm displacement, near the yield point. (**b**) Simulated stress-strain curves of cellular solids with multiple coating thicknesses.

With C_1 and C_2 known, the yield strength and relative density of cellular solids with varying strut size are measured to deduce the size based strengthening effect. SEM measurements combined with a geometric model of the inverse opal cellular solid determine the

cellular solid relative density ($\rho^*/\ \rho_s$). The SEM measurements and model are detailed in the methods section. Micropillar compression tests measure the cellular solid yield strength, σ^* (*36*). Figure 6.3a shows before and after SEMs of 4 μm diameter cellular solid micropillars used in the compression tests. The pillars are made from 500 nm diameter PS opals. The second pillar has a 19 nm nickel coating. Failure predominately occurs along the [111] direction at the narrowest region of the struts, which agrees with the finite element simulations. The [111] direction is parallel to the micropillar axis. Figure 6.3b shows the stress-strain curves for several cellular solid and bulk nickel micropillars loaded to a strain of about 0.2. The yield stress is measured at 0.2% offset strain. The cellular solid micropillars have 500 nm pores. The average yield strengths are 274, 612, and 878 MPa for cellular solids with no coating, 19 nm, and 33 nm coatings. Equation 6.2 calculates corresponding strut yield strengths of 6.03, 3.57, and 3.57 GPa for the cellular solids. The strut yield strengths are much larger than the 1.98 GPa yield strength of bulk electrodeposited nickel. 1.98 GPa yield stress is near the maximum reported for bulk nickel (*37*). Table 6.1 shows the compressive yield strengths of several cellular solids and their struts tested in this study. The effective diameter of each strut is compared to the strut strength to calculate the size based strengthening effect. The inverse opal strut has a pseudo-triangular shape with concave edges that result from the intersection of three spheres. The effective diameter is four times the area divided by the perimeter, 4A / (3s). The area of the strut, *A*, and perimeter, 3*s*, are determined from SEM measurements of *R* and *b*, which is detailed in the methods section. Figure 6.3c shows the dependence of the strut yield strength on the strut effective diameter at the narrowest region of the struts, approximately where failure occurs. The strut strength increases significantly as the effective strut diameter decreases. The best fit power law, shown in black, is $\sigma_{strut} = 50\ d^{-0.57}$ GPa, which agrees well with the ≈-0.6 power dependence reported for

nanopillars made of nickel and other materials (*10, 36*). The strut yield strength is greater than the yield strength of electrodeposited nickel with 15 nm grain size when the strut diameter is less than 300 nm. The highest strut yield strength is 10.00 GPa for the cellular solid with 260 nm pore size, 0.099 solid volume fraction, and 17 nm effective strut diameter. The nanoscale confinement of the strut diameter provides up to a 5X increase in the nickel strength over the bulk electrodeposited nickel.

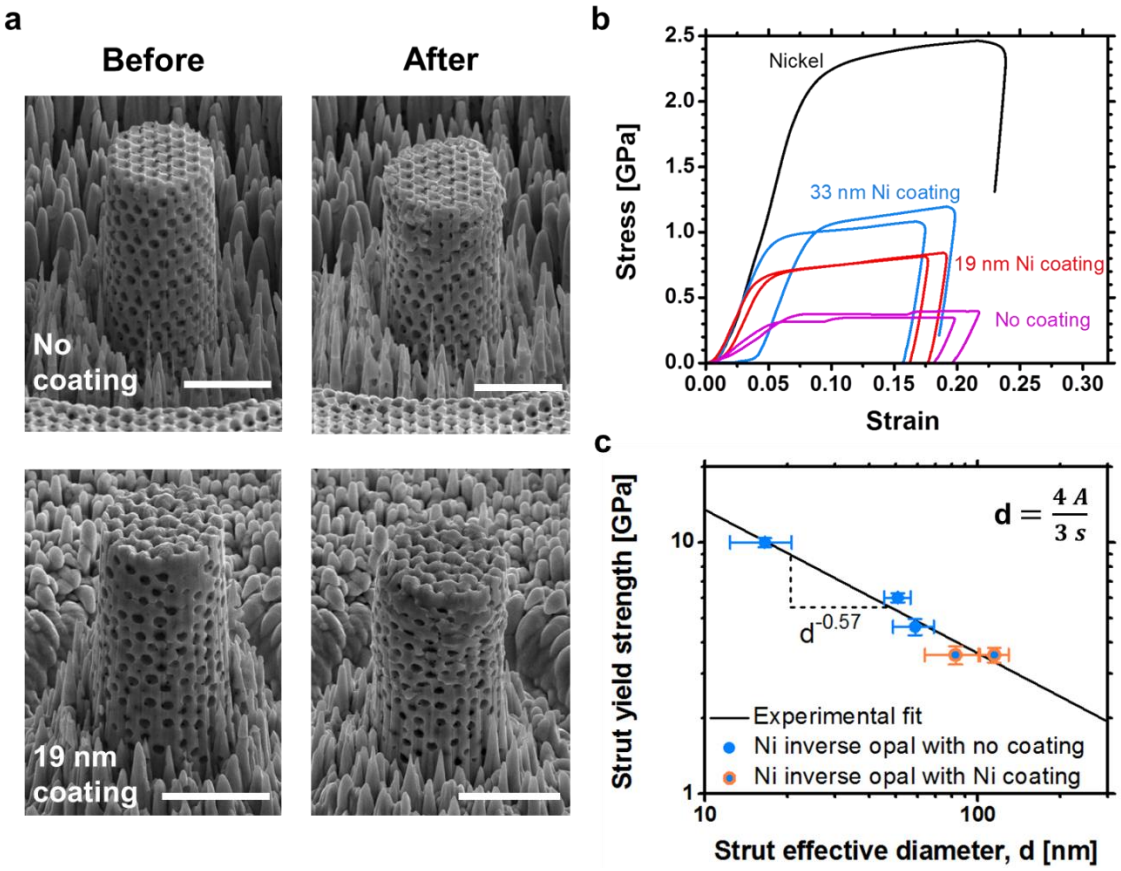

Figure 6.3: (**a**) SEM images of inverse opal cellular solid micropillars with 500 nm pores before and after being subjected to compression testing. The uncoated sample is 84% porous and the 19 nm Ni coated samples is 58% porous. Failure occurs in [111] direction, parallel to the compression axis. Scale bars are 3 µm. (**b**) Stress-strain data for micropillars tested under compression. The inverse opal cellular solids have 500 nm pores. The nickel sample is fully dense electroplated nickel. (**c**) Variation of strength with strut diameter for nickel inverse opals with 260, 500, and 930 nm pores (left to right in blue) and 500 nm pore samples coated with 19 and 33 nm of additional nickel (left to right in blue and orange).

Nanoindentation hardness measurements provide a rapid investigation of the cellular solid strength when compared to micropillar compression tests. Hardness, *H*, is a material's resistance to plastic deformation and can be correlated to yield strength. The yield strength of bulk materials are approximately equal to *H*/3, but for cellular solids with low relative density the yield strength is approximately equivalent to hardness due to the plastic Poisson's ratio approaching zero (*34, 38, 39*). Figure 6.4a shows hardness measurements for various nickel cellular solids with 500 nm diameter pores coated with nickel and rhenium-nickel alloy. The plateau region values were taken as the sample's hardness for each test. Figure 6.4b shows hardness versus total solids volume fraction for various cellular solids with 500 nm pores. Error bars show standard deviations. Linear and quadratic relationships between the bulk hardness and volume fraction are included to guide the eye. Most samples have hardness above the quadratic and below the linear relationships. The specific hardness of the 33 nm nickel coated nickel cellular solid with 0.43 volume fraction is 3.7 X greater than the non-coated inverse opal sample. The degree that hardness can predict yield stress is determined by comparing hardness values to yield stress measurements from micropillar compression tests. Figure 6.4c shows hardness and yield stress measurements of nickel inverse opals with and without coatings. The black line shows a polynomial fit for the yield stress of nickel samples with 500 nm pores. The hardness and yield stresses are similar at low solid volume fractions and diverge at high volume fractions. There is less than 15% difference between hardness and yield stress measurements for samples with less than 0.16 solids volume fraction. Hardness values start to diverge from the yield stress measurements at greater than 0.3 solids volume fraction as the plastic Poisson's ratio approaches the bulk value. Nanoindentation hardness measurements provide a rapid and simple technique to determine the yield strength of cellular solids with less than 0.3 solids volume fraction.

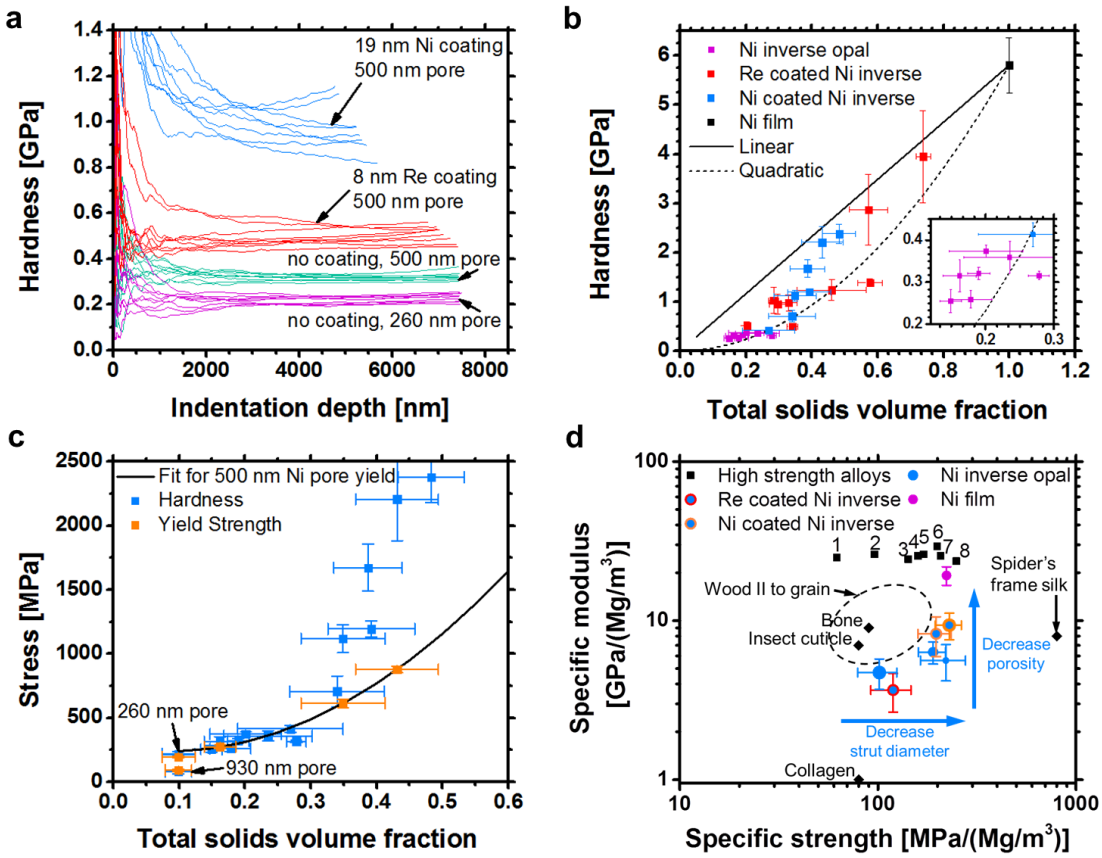

Figure 6.4: (**a**) Nanoindentation hardness of plain nickel inverse opals and inverse opals coated with rhenium and nickel. (**b**) Hardness versus total solids volume fraction of several plain and composite cellular solids measured using nanoindentation. The inset shows hardness between 0.12 and 0.3 total solids volume fraction. (**c**) Hardness and yield strength versus solids volume fraction of several uncoated and nickel coated nickel cellular solids. The solid line is a polynomial fit for yield stress of nickel cellular solids with 500 nm pores. (**d**) An Ashby plot comparing the specific modulus and specific strength of the nanoporous nickel cellular solids with nickel coating (orange) and rhenium coating (red) to other high strength materials. Natural materials are shown in green (*40*). Bulk electrodeposited nickel is shown in blue. Common Ti, Al, Ni, and Fe high strength alloys are labeled 1 – 8: 1 - CP Ti, 2 - 2024-T4, 3 - Inconel 718, 4 - 4143 steel, 5 - 7075-T6, 6 - HSSS steel, 7 - Ti-6Al-4V, 8 - Ti-10V-2Fe-3Al (*41-44*).

The inset in Fig. 6.4b also shows how the hardness, and therefore strength, of non-coated inverse opals varies with disorder in the self-assembly process of ≈500 nm diameter PS particles. The non-coated inverse opal hardness, the violet data points, increases with solid

volume fraction at an approximately quadratic rate. The increased volume fraction is due to defects in the self-assembly process that lead to disorder and lower coordination numbers. Additional details regarding the relationship between the level of disorder and volume fraction is provided in the methods section. The specific hardness of the inverse opals with 500 nm pores decreases from 220 to 130 MPa / (Mg/m^3) as solids volume fraction, and therefore disorder, increases from 0.16 to 0.28. The best fit power law for the specific hardness and volume fraction is 65 $(\rho^*/ \rho_s)^{-0.62}$. The decrease in specific hardness shows that regular ordering of the pores is important to achieving high specific strength. Fabrication techniques with random sphere packing, like slurry casting, are less likely to produce high specific strength materials than fabrication techniques with regular architectures. This observation might also explain why the nanoporous gold prepared with de-alloying which has a random porosity does not have the ultra-high strength observed in this study (*7, 11, 19-22*).

The inverse opal cellular solid architecture enables high specific strength. Table 6.1 shows detailed specific strength data for the cellular solids. The specific strengths vary between 168 and 230 MPa / (Mg/m^3), with the exception of the 930 nm pore sample. The 930 nm pore inverse opal cellular solid has a lower specific strength of 102 MPa / (Mg/m^3) than other cellular solids because of the large strut diameter and low solids volume fraction. The strut diameter is approximately quadratically related to the PS diameter, so as the PS diameter increases the size based strengthening reduces considerably. The bending dominated deformation in the inverse opal architecture should result in reduced strength when compared to structures that deform elastically and have similar relative density. Interestingly, the specific strengths of the inverse opal architecture reported here and in ref. (*33*) are greater than specific strengths reported for nanoscale octet-truss architectures, which should deform elastically. Specific strengths of 140,

17.2, 21.6, 23, and 35.19 MPa / (Mg/m^3) have been reported for octet-truss structures fabricated from alumina, 1,6-hexanediol diacrylate, and Ni-P hollow tubes (*2, 3, 17*). The high specific strength of the inverse opals is primarily due to the large concentration of regularly ordered high strength nm confined struts. There are 32 50-nm diameter struts in every 0.35 μm^3 for non-coated 500 nm pore inverse opals. These nm confined struts with large number density can be fabricated over very large areas and with the assembly of relatively large colloidal crystals. Additionally, the highest stress concentrations occur in the narrowest part of the strut, which is also where the material is strongest due to size based strengthening. This balance between local strength and stress concentration, and the smooth transitions between stress concentrations, provides the inverse opal with high specific strength.

The strut size, solids volume fraction, and chemistry of inverse opal cellular solids can be tuned to control the specific modulus and specific strength. Figure 6.4d shows the specific strength versus specific modulus of inverse opal cellular solids, select high strength Ti, Ni, Al, and steel alloys, and important natural materials. The solids volume fraction or density of the constituent materials controls the cellular solid specific modulus. The specific elastic moduli of nickel cellular solids and fully dense nickel vary between 4 and 20 GPa / (Mg/m^3). The specific strengths of nickel cellular solids are higher than most high strength alloys including 4143 steel and Ti-6Al-4V. Coating additional layers of nickel on 500 nm pore cellular solids increased the solids volume fraction from 0.16 to 0.43 and increased the specific modulus from 6.2 to 9.4 GPa / (Mg/m^3). Interestingly, the specific strength of 500 nm diameter pore cellular solids remained near 200 MPa / (Mg/m^3) as additional layers of nickel were coated. The specific strength remained relatively constant because of the competing effects of porosity and size based strengthening. An increased porosity increased the strength but also increased the strut diameter,

which reduced the strut strength, such that there was no net effect on the bulk cellular solid strength. Decreasing the pore size to 260 nm increased the specific strength of inverse opal cellular solids to 220 MPa / (Mg/m^3) because the solids volume fraction remained near the same as 500 and 930 nm pores, but the struts became considerably smaller and stronger. Nickel inverse opals with 0.3 and 0.5 solid volume fractions and < 12nm struts could achieve high specific strengths of 600 and 870 MPa / (Mg/m^3) because the strut strengths would be near the 12.1 GPa theoretical yield strength of nickel. Overall, the inverse opal cellular solids exhibit specific moduli that are similar to natural materials like bone, collagen, insect cuticles, spider silk and wood parallel to the grain. However, only the specific strength of silk exceeds the nickel cellular solids. When compared to other engineered materials, nickel inverse opal cellular solids provide a unique combination of moderate specific stiffness similar to natural structural materials and high specific strengths greater than most engineering alloys.

Table 6.1 Mechanical and physical measurements of inverse opal cellular solids.

Material	PS** size [nm]	Coating thickness [nm]	Hardness [Gpa]	Modulus [Gpa]*	Total solids volume fraction	Yield strength [Gpa]	Strut yield strength [Gpa]	Specific strength [MPa /(Mg/m^3)]	Specific modulus [GPa /(Mg/m^3)]
Ni Bulk			5.806	171	1.00	1.98		222	19.2
Ni inverse	260		0.213	17	0.10				18.7
Ni inverse	260		0.218	5*	0.10	0.19	10.00	220	5.6
Ni inverse	500		0.321	34	0.19				20.0
Ni inverse	470		0.255	25	0.15				19.1
Ni inverse	520		0.315	9*	0.16	0.27	6.03	190	6.2
Ni inverse	500		0.359	30	0.23				14.7
Ni inverse	500		0.316	27	0.28				10.9
Ni inverse	470		0.374	27	0.21				14.9
Ni inverse	490		0.259	21	0.18				13.3
Ni inverse	930		0.082	4*	0.10	0.09	4.62	102	4.5
Re on Ni Inv.	520	5	0.508	51	0.21				26.6
Re on Ni Inv.	500	8	0.499	44	0.34				14.5
Re on Ni Inv.	490	15	1.024	71	0.32				25.3
Re on Ni Inv.	500	18	0.977	48	0.36				15.0
Re on Ni Inv.	490	19	0.953	51	0.34				16.9
Re on Ni Inv.	500	25	1.236	21*	0.46	0.69	2.48	168	5.1
Re on Ni Inv.	500	41	1.386	70	0.57				13.8
Re on Ni Inv.	470	59	2.870	100	0.57				19.6
Re on Ni Inv.	470	87	3.950	116	0.72				17.9
Ni on Ni inv.	500	5	0.413	42	0.27				17.4
Ni on Ni inv.	500	13	0.706	59	0.34				19.7
Ni on Ni inv.	470	19	1.118	29*	0.35	0.61	3.57	197	9.3
Ni on Ni inv.	470	25	1.193	70	0.39				20.0
Ni on Ni inv.	495	28	1.672	85	0.39				24.8
Ni on Ni inv.	495	33	2.206	36*	0.43	0.88	3.57	229	9.4
Ni on Ni inv.	520	38	2.379	74	0.48				17.3

* Modulus data from nanoindentation measurements.
** PS: polystyrene

6.3 Methods

The inverse opal cellular solids were fabricated by self-assembling polystyrene (PS) opals onto a gold coated glass slide, electrodepositing nickel, and etching the remaining PS. The gold coated glass slide was fabricated by sputtering 8 nm of chromium followed by 50 nm of gold on a 1 mm thick soda lime glass slide. The glass slide with gold pattern was cut into smaller samples, piranha cleaned for ten minutes, immersed in Millipore water with 3-mercapto-1-propanesulfonic acid, sodium salt (2.2 % by weight) for 4 hours and rinsed. Polystyrene (PS) opals were self-assembled onto the gold coated substrates by placing the substrates vertically in a 1 inch diameter plastic container filled with a colloidal solution of PS spheres. The plastic container was then set on a hot plate at 55^{o}C, covered, and left for 24 to 30 hours until the solution was dry. The PS diameters were varied between 200 – 2,000 nm to change the cellular solid strut size. The substrates were then sintered at 96 °C for 30 minutes to 6 hours depending on the PS diameter. Longer sinter times increase the interconnect diameter between spheres and reduce the nickel volume fraction. The PS colloid solution was made by combining 8 wt% PS sphere solution (1.2 grams), purchased from Invitrogen, with ultrapure water (40 grams). Nickel was then electrodeposited through the PS opal at a constant -1.8 volts versus a nickel reference electrode for 32 minutes in commercial plating solution, Technic RTU Mechanical Agitation. PS was removed by immersing the substrates in a tetrahydrofuran bath for 24 hours followed by a tetrahydrofuran and toluene rinse. The resulting cellular solids were about 15 – 20 μm thick. Additional nickel was coated on the inverse opal cellular solids using the same electroplating solution, but pulsing -1.7 volts for 30 seconds in between 20 second intervals of 0 amperage current for 15 – 90 cycles.

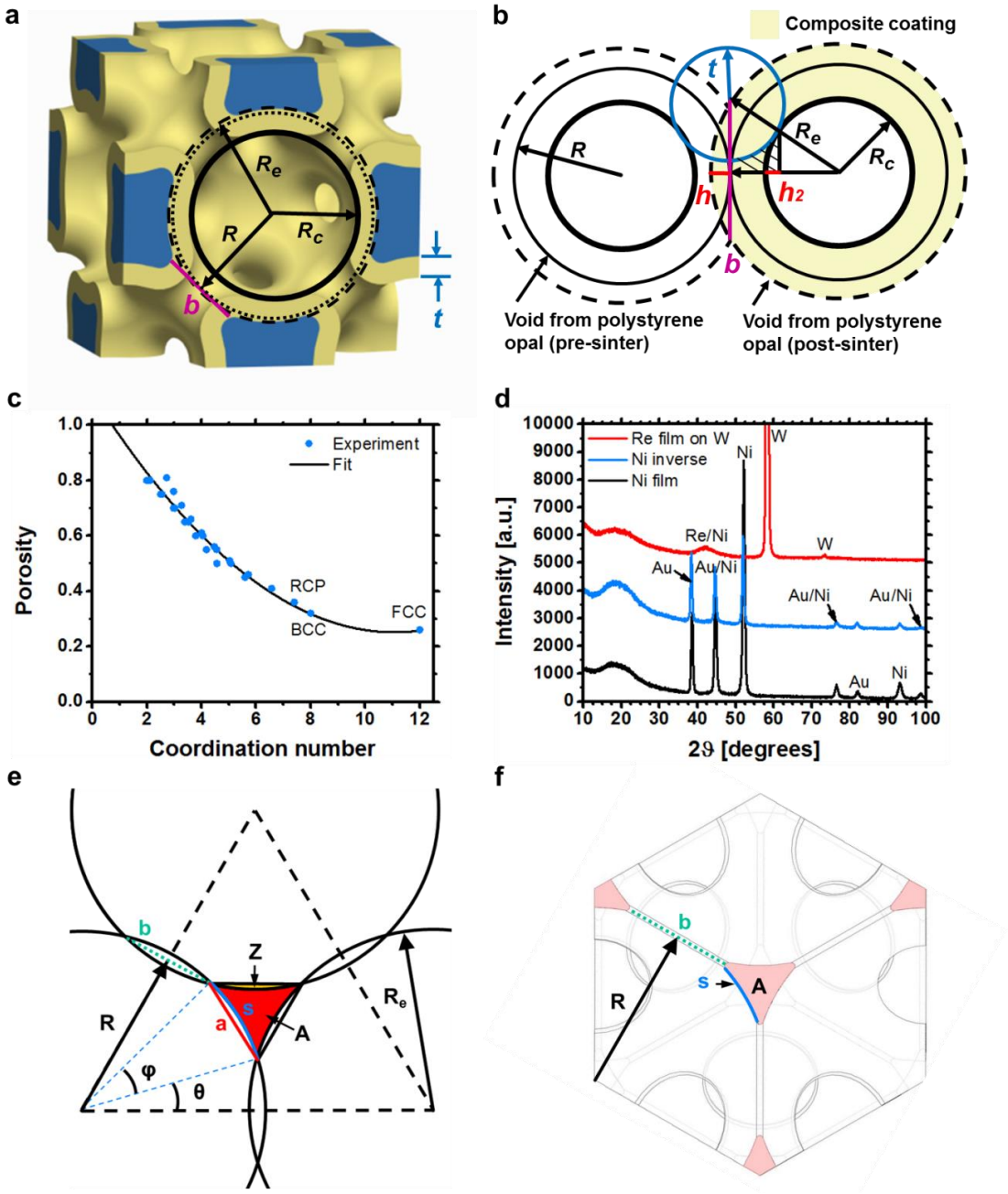

Figure 6.5: (**a**) A unit cell of the nanocomposite inverse opal cellular solid with important geometric properties. (**b**) A geometric model of the nanocomposite cellular solid used to calculate the volume fraction of each material in the composite. (**c**) Experimental data and curve fit relating the porosity of packed spheres to the coordination number. Experimental data is from (*42*, *44*, *45*). The curve fit is used to correct the volume fraction of the cellular solids for defects during assembly. (**d**) X-ray diffraction data for an electrodeposited nickel film, nickel inverse opal, and rhenium film used to characterize the crystallinity of the composite materials. (**e**-**f**) Geometry of the inverse opal struts at the narrowest region. An effective diameter is calculated from measurements of *R* and *b* to relate the strut diameter to size based strengthening effect.

Rhenium-nickel alloy is used as a coating because of its high ductility, strength, and creep resistance at high temperatures (*45*). The rhenium-nickel alloy coating was deposited galvanostatically with a 5 $mA \cdot cm^{-2}$ current density in a pH 5 electroplating bath with 34 mM NH_4ReO_4, 93 mM $Ni(NH_2SO_3)_2 \bullet 4H_2O$ and 300 mM $C_6H_8O_7$ modified from ref. (*46*). NaOH was used to adjust the pH. ReO_4^- is the most stable form of rhenium ion in solution. Citric acid, a tri-basic acid, deprotonates gradually as the pH is increased and is as a complexing agent. The plating bath was immersed in silicone oil at 75°C. A platinum reference and counter electrode was used. Varying the precursor concentration changes the alloy composition. The plated alloy was about 80 weight percent rhenium measured with energy-dispersive X-ray spectroscopy.

The nickel inverse opal volume fraction, ε_{Ni}, and coating volume fraction, ε_{coat}, calculate the relative density of the cellular solid, which is the independent variable for calculating the effective mechanical properties of cellular solids. ε_{Ni} and ε_{coat} are calculated from SEM measurements of PS radius, *R*, interconnect diameter, *b*, and coating thickness, *t*, combined with a geometric model of self-assembled PS spheres organized in a FCC unit cell. Figure 6.5a shows a unit cell of the inverse opal cellular solid and indicates important geometrical parameters. The inverse opal volume is the cubic unit cell volume minus the volume of the sintered polystyrene spheres, V_{PS}. The conformally coated layer volume, V_{coat}, is the volume of a thin layer subtracted from V_{PS}. The symmetry of the FCC unit cell allows V_{coat} and V_{PS} to be calculated from the geometry of two neighboring PS spheres. Figure 6.5b shows the geometric model used to calculate the volume fractions. The circles with radius *R* represent two PS spheres in contact after opal self-assembly with an initial 0.74 volume fraction expected for FCC packing. The PS volume increases after sintering and is calculated by increasing *R* to R_e such that neighboring

radii overlap by a length b. V_{PS} is the volume of 4 spheres of radii R_e minus the volume of 48 overlapping spherical caps of height *h* or

$$V_{PS} = 4\ \frac{4}{3}\ \pi\ {R_e}^3 - 48\ \frac{1}{3}\ \pi\ h^2(3\ R_e - h), \tag{6.4}$$

where $R_e = \sqrt{(b/2)^2 - R^2}$ and h is R_e - R. V_{coat} is the volume of the sphere of radius R_c subtracted from V_{PS}. Additionally, the volume where the coating does not deposit, marked with hatching, is integrated and subtracted out, but not including the volume of the spherical cap marked by *h2*.

$$V_{coat} = V_{PS} - \ 4\ \frac{4}{3}\ \pi\ (R_c)^3 - 48\ \int_0^{\frac{R_c\,R}{R_e}} \pi\ \left(\frac{b}{2} - \sqrt{t^2 - x^2}\right)^2\ dx + 48\frac{1}{3}\ \pi\ h2^2(3\ R_c - h2), \tag{6.5}$$

where *h2* is R_c (1 – R / R_e) and t is R_e – R_c. ε_{Ni} and ε_{coat} are calculated from V_{PS} and V_{coat} normalized by the unit cell volume, $\left(2\ R\ \sqrt{2}\right)^3$.

$$\varepsilon_{Ni} = 1 - \frac{V_{PS}}{\left(2\ R\ \sqrt{2}\right)^3} \text{ and} \tag{6.6}$$

$$\varepsilon_{coat} = \frac{V_{coat}}{\left(2\ R\ \sqrt{2}\right)^3}. \tag{6.7}$$

Equations 6.6 and 6.7 are used to generate a sample of volumes based on the exhausted combination of the measured *R*, *b*, and *t*. These representative samples determine the mean and standard deviations of ε_{Ni} and ε_{coat}. *R* and *b* are measured in SEMs of the inverse opal with no coating. *R* is half the average distance between the center of interconnect openings, the distance from the center of *b* on one side of the PS void to the center of *b* on the other. *b* is the average measured interconnect diameter. *t* is measured by taking half the difference in the measured interconnect opening, *b*, before and after deposition. *t* is also measured directly at the inverse opal struts in cross-section SEMs, although this is difficult for coatings less than 15 nm.

The self-assembly process does not always result in a perfect FCC orientation of the PS spheres. Oversized PS particles cause the loss of contact between adjacent PS spheres, usually resulting in a small separation between spheres and rarely in a vacancy. As the number of defects increases the regular PS orientation can degenerate into a random close packed structure (RCP) resulting in a nickel volume fraction of 0.36 (*47, 48*). It is important to be able to quantify the level of defects in inverse opal cellular solids and adjust the solids volume fraction accordingly as the mechanical properties have a polynomial dependence on the solids volume fraction. The coordination number of packed spheres has been shown to correlate to their volume fractions (*47, 49, 50*). Figure 6.5c shows experimental data that relates coordination number to porosity combined with known FCC, BCC, and RCP coordination numbers (*47, 49, 50*). A polynomial correlation of $\varepsilon_{pore} = 0.007\ CN^2 - 0.155\ CN + 1.1093$ was determined using the data in Fig. 6.5c, where ε_{pore} is the void volume fraction of polystyrene spheres before sintering and CN is the average coordination number of the sample. CNs greater than 10 minimally affect the volume fraction. An FCC orientation has a CN of 12. When neighboring PS spheres are in contact and sintered, the resulting interconnect reduces the volume fraction of the inverted structure. When the CN is less than 12, the total volume lost from sintering is reduced and the starting volume fraction, ε_{pore}, is increased. ε_{Ni} is corrected to ε'_{Ni} by subtracting the amount of volume lost due to sintering from ε_{pore}, such that

$$\varepsilon'_{Ni} = \varepsilon_{pore} - CN\frac{\varepsilon_{Ni}(b) - \varepsilon_{Ni}(b=0)}{12}, \tag{6.8}$$

where $\varepsilon_{Ni}(b)$ is the mean solved using Equation 6.6 with exhausted combinations of *R* and *b*. When the inverse opal cellular solid is coated with additional material, the coating volume fraction, ε_{coat}, is corrected to ε'_{coat} by multiplying the mean of ε_{coat} in Equation 6.7 by 1/12 the

CN and adding the volume fraction of a thin film that would cover the area where there are no interconnects between pores. The thin film volume fraction is 1/12 the volume fraction of a spherical shell made by the film thickness on the interior of a sphere with the diameter of the PS, multiplied by (12 – CN). The final total solid volume fraction is

$$\varepsilon''_{Ni} = \varepsilon'_{Ni} + \varepsilon'_{coat}. \tag{6.9}$$

In addition to defects in the ordered structure, cracks several micrometers wide separate ordered islands of PS particles. The cracks become fully dense nickel after nickel electrodeposition. These areas are avoided during inverse opal mechanical measurements.

The mechanical properties of the bulk materials depend on their crystal structure. Figure 6.5d shows XRD data for a solid nickel film, nickel inverse opal, and solid rhenium film deposited on tungsten. The average grain sizes of the nickel film and nickel inverse opals calculated from the XRD data using the Scherrer equation are 12.4 nm and 15.1 nm. A 15 nm grain size in pure nickel corresponds to a ≈6.4 GPa hardness (*37*), near the peak hardness values of pure nickel, which agrees well with our electrodeposited nickel thin film nanoindentation hardness measurements of 5.8 GPa. The deposited rhenium-nickel alloy was amorphous with some polycrystallinity detected in transmission electron microscopy diffraction patterns.

Plastic deformation simulations are performed in COMSOL using the nonlinear structural materials module. The repeat cell is chosen with the (111) plane on top to best represent the deformation in the nanoindentation and micropillar compression tests. A symmetric boundary condition is used on vertical faces and roller boundary condition on the bottom. The elastic modulus and yield strength of the bulk nickel are 171 GPa and 2 GPa, based on measurements of the bulk electrodeposited nickel. A Poisson's ratio of 0.31 is used. A displacement boundary

condition is applied normal to the top surface and the average reaction force at the displaced boundary is recorded at each displacement increment (*51, 52*). The elastic modulus of cellular structures is calculated at the first increment of simulations. The flow stress at 0.2% offset plastic deformation is chosen as the yield strength. The structure is simulated with five combined repeat cells of twice the vertical height to validate the boundary conditions. Structural steel from the COMSOL library is also simulated in the cellular solid and yields a similar relationship between volume fraction, modulus and yield stress as nickel.

The inverse opal cellular solids were mechanically characterized using nanoindentation and micropillar compression. An Agilent G200 Nanoindenter with a diamond Berkovich tip measured the hardness and elastic modulus of the samples through continuous stiffness measurements. The continuous stiffness technique provides mechanical properties as a function of indentation depth. The indentation depths were limited to 7.5 μm or the maximum peak load of 600 mN. The data has a large standard deviation due to the surface roughness inherent to the porous structure at indentation depths below 500 nm. Material aggregation and substrate mechanical properties affect the measurements at indentation depths comparable to the sample thickness (*53, 54*). In between these extremes, the data has a plateau typically near 2000 nm depth. The hardness and elastic modulus from each indentation were determined by the average value in this plateau range. For each sample, the reported values are the average of 10 indentations or more.

Micropillar specimens were prepared by using an FEI Helios Nanolab 600i focused ion beam. Annular milling in three steps using beam currents of 21 nA, 2.5 nA and 80 pA resulted in cylindrical specimens of ≈3.6 μm diameter and ≈8 μm height. A final 100 nm-wide ring milling facilitated adjusting the height of the micropillars and minimizing their taper. The Agilent G200

Nanoindenter with a 10 μm diameter flat diamond punch compressed the micropillars at an average strain rate of ≈1e-4 s^{-1}. The nanoindenter deformed the micropillars to a total strain of about 20%. SEM-measured micropillar diameter and height allowed the calculation of stress-strain behavior. The stress at 0.2% strain offset was used as the yield strength. The loading and unloading moduli are corrected to account for the substrate thickness using the method described in ref. (*55*). The Poisson's ratio of the inverse opal cellular solids is taken as zero for nanoindentation and micropillar compression calculations based on previous testing of nanoporous open-cell foams and qualitative experimental observations (*7*, *21*).

Measurements of the polystyrene radius, *R*, and interconnect diameter, *b*, calculate the effective diameter of the inverse opal cellular solid struts using the inverse opal geometry. *R* and *b* are the same measurements required to calculate the inverse opal volume fractions. Figure 6.5e shows the geometry of the narrowest part of the strut. The effective diameter, *d*, is calculated from the strut area, *A*, perimeter, *P*, and coating thickness, *t*, by

$$d = \frac{4A}{P} + 2t. \tag{6.10}$$

t is measured experimentally as discussed in the volume fraction calculation section. The area of the strut is the area of the triangle that connects the strut tips with side length *a* minus the area of the 3 circular segments, *Z*.

$$Z = 0.5\left({R_e}^2\varphi - 0.5a\sqrt{4{R_e}^2 - a^2}\right). \tag{6.11}$$

The angle between strut edges from the pore center, φ, is $\pi/3 - 2\tan^{-1}(b/2R)$. The edge length between the strut tips, *a*, is calculated using the law of cosines with R_e and φ. R_e is $\sqrt{(b/2)^2 - R^2}$. The strut area is therefore

$$A = \frac{\sqrt{4}}{3}a^2 - 3\frac{1}{2}\left(R_e{}^2\varphi - \frac{1}{2}a\sqrt{4R_e{}^2 - a^2}\right). \quad (6.12)$$

The strut perimeter is three times the arc length of the strut side,

$$P = 3s = 3R_e\varphi. \quad (6.13)$$

6.4 Conclusion

In conclusion, we present nickel and rhenium nanocomposite inverse opal cellular solids with controllable specific moduli between 4 and 20 GPa / (Mg/m^3) and specific strengths up to 230 MPa / (Mg/m^3). The cellular solid strut diameter and porosity determine the strength of the cellular solids whereas only the porosity determines the stiffness of the cellular solids. Additional coatings of nickel and rhenium-nickel alloy allow further control of the specific modulus and strength. The struts in the inverse opal cellular solids have yield strengths up to 5 times the strength of bulk electrodeposited nickel due to the size based strengthening effect. The inverse opal cellular solids have specific strengths greater than most high strength alloys, yet deform primarily by bending, resulting in specific stiffness similar to natural materials. Nickel inverse opal cellular solids are easy to fabricate, can be processed at room temperature in any lab, and represent a promising platform architecture for measuring the size based strength enhancements in multiple metallic, ceramic, and polymer materials. In addition, self-assembly based fabrication overcomes the maximum sample size restrictions common with other fabrication technologies, enabling macroscopic cellular solids to be fabricated and integrated into engineered devices. Future work could explore the effects of adding multiple layers of composite materials on the mechanical properties and measuring the fracture toughness of the inverse opal cellular solids, which is predicted to be low, but requires large sample sizes to accurately measure.

6.5 References

1. Z. Shan, R. K. Mishra, S. S. Asif, O. L. Warren, A. M. Minor, Mechanical annealing and source-limited deformation in submicrometre-diameter Ni crystals. *Nat. Mater.* **7**, 115 (2008).
2. L. R. Meza, S. Das, J. R. Greer, Strong, lightweight, and recoverable three-dimensional ceramic nanolattices. *Science* **345**, 1322 (September 12, 2014, 2014).
3. L. R. Meza *et al.*, Resilient 3D hierarchical architected metamaterials. *Proceedings of the National Academy of Sciences*, (September 1, 2015, 2015).
4. P. Fratzl, R. Weinkamer, Nature's hierarchical materials. *Progress in Materials Science* **52**, 1263 (2007).
5. R. Lakes, Materials with structural hierarchy. *Nature* **361**, 511 (1993).
6. M. F. Ashby, The properties of foams and lattices. *Philosophical Transactions of the Royal Society A: Mathematical, Physical and Engineering Sciences* **364**, 15 (January 15, 2006, 2006).
7. J. Biener, A. M. Hodge, A. V. Hamza, L. M. Hsiung, J. H. Satcher, Nanoporous Au: A high yield strength material. *Journal of Applied Physics* **97**, 024301 (2005).
8. J.-H. Lee, L. Wang, M. C. Boyce, E. L. Thomas, Periodic Bicontinuous Composites for High Specific Energy Absorption. *Nano Letters* **12**, 4392 (2012/08/08, 2012).
9. J. R. Greer, W. C. Oliver, W. D. Nix, Size dependence of mechanical properties of gold at the micron scale in the absence of strain gradients. *Acta Materialia* **53**, 1821 (2005).
10. C. P. Frick, B. G. Clark, S. Orso, A. S. Schneider, E. Arzt, Size effect on strength and strain hardening of small-scale [111] nickel compression pillars. *Materials Science and Engineering: A* **489**, 319 (2008).
11. C. Volkert, E. Lilleodden, D. Kramer, J. Weissmuller, Approaching the theoretical strength in nanoporous Au. *Appl. Phys. Lett.* **89**, 061920 (2006).
12. M. D. Uchic, D. M. Dimiduk, J. N. Florando, W. D. Nix, Sample Dimensions Influence Strength and Crystal Plasticity. *Science* **305**, 986 (August 13, 2004, 2004).
13. J. Bauer, S. Hengsbach, I. Tesari, R. Schwaiger, O. Kraft, High-strength cellular ceramic composites with 3D microarchitecture. *Proceedings of the National Academy of Sciences*, (February 3, 2014, 2014).
14. X. Wendy Gu, J. R. Greer, Ultra-strong architected Cu meso-lattices. *Extreme Mechanics Letters* **2**, 7 (2015).
15. D. Jang, L. R. Meza, F. Greer, J. R. Greer, Fabrication and deformation of three-dimensional hollow ceramic nanostructures. *Nat Mater* **12**, 893 (2013).
16. L. C. Montemayor, L. R. Meza, J. R. Greer, Design and Fabrication of Hollow Rigid Nanolattices via Two-Photon Lithography. *Adv. Eng. Mater.* **16**, 184 (2014).
17. X. Zheng *et al.*, Ultralight, ultrastiff mechanical metamaterials. *Science* **344**, 1373 (June 20, 2014, 2014).
18. T. A. Schaedler *et al.*, Ultralight Metallic Microlattices. *Science* **334**, 962 (November 18, 2011, 2011).
19. J. Biener, A. M. Hodge, A. V. Hamza, Microscopic failure behavior of nanoporous gold. *Appl. Phys. Lett.* **87**, 121908 (2005).

20. J. Biener *et al.*, Size Effects on the Mechanical Behavior of Nanoporous Au. *Nano Letters* **6**, 2379 (2006/10/01, 2006).
21. A. M. Hodge *et al.*, Scaling equation for yield strength of nanoporous open-cell foams. *Acta Materialia* **55**, 1343 (2007).
22. D. Lee *et al.*, Microfabrication and mechanical properties of nanoporous gold at the nanoscale. *Scripta Materialia* **56**, 437 (2007).
23. K. A. Arpin *et al.*, Multidimensional architectures for functional optical devices. *Advanced Materials* **22**, 1084 (2010).
24. P. Jiang, J. F. Bertone, K. S. Hwang, V. L. Colvin, Single-Crystal Colloidal Multilayers of Controlled Thickness. *Chem. Mater.* **11**, 2132 (1999/08/01, 1999).
25. C. Park, J. Yoon, E. L. Thomas, Enabling nanotechnology with self assembled block copolymer patterns. *Polymer* **44**, 6725 (2003).
26. U. G. K. Wegst, H. Bai, E. Saiz, A. P. Tomsia, R. O. Ritchie, Bioinspired structural materials. *Nat Mater* **14**, 23 (2015).
27. J. D. Joannopoulos, P. R. Villeneuve, S. Fan, Photonic crystals: putting a new twist on light. *Nature* **386**, 143 (1997).
28. J. H. Pikul, H. Gang Zhang, J. Cho, P. V. Braun, W. P. King, High-power lithium ion microbatteries from interdigitated three-dimensional bicontinuous nanoporous electrodes. *Nat. Commun.* **4**, 1732 (2013).
29. H. Zhang, X. Yu, P. V. Braun, Three-dimensional bicontinuous ultrafast-charge and -discharge bulk battery electrodes. *Nat. Nanotechnol.* **6**, 277 (2011).
30. A. Stein, B. E. Wilson, S. G. Rudisill, Design and functionality of colloidal-crystal-templated materials-chemical applications of inverse opals. *Chemical Society Reviews* **42**, 2763 (2013).
31. X. You, J. H. Pikul, W. P. King, J. J. Pak, Zinc oxide inverse opal enzymatic biosensor. *Appl. Phys. Lett.* **102**, 253103 (2013).
32. Z. Li *et al.*, Effects of pore size on the mechanical properties of three-dimensionally ordered macroporous nickel. *Materials & Design* **45**, 52 (2013).
33. J. J. do Rosário *et al.*, Self-Assembled Ultra High Strength, Ultra Stiff Mechanical Metamaterials Based on Inverse Opals. *Adv. Eng. Mater.*, n/a (2015).
34. L. J. Gibson, M. F. Ashby, *Cellular Solids : Structure and Properties*. (Cambridge University Press, Cambridge, ed. Second, 1997).
35. V. S. Deshpande, M. F. Ashby, N. A. Fleck, Foam topology: bending versus stretching dominated architectures. *Acta Materialia* **49**, 1035 (2001).
36. M. D. Uchic, P. A. Shade, D. M. Dimiduk, Plasticity of Micrometer-Scale Single Crystals in Compression. *Annual Review of Materials Research* **39**, 361 (2009).
37. A. M. El-Sherik, U. Erb, G. Palumbo, K. T. Aust, Deviations from hall-petch behaviour in as-prepared nanocrystalline nickel. *Scripta Metallurgica et Materialia* **27**, 1185 (1992).
38. E. J. Pavlina, C. J. Van Tyne, Correlation of Yield Strength and Tensile Strength with Hardness for Steels. *J. of Materi Eng and Perform* **17**, 888 (2008/12/01, 2008).
39. P. Zhang, S. X. Li, Z. F. Zhang, General relationship between strength and hardness. *Materials Science and Engineering: A* **529**, 62 (2011).
40. R. W. Blake, *Efficiency and economy in animal physiology*. (Cambridge University Press, 2005).

41. G. Welsch, R. Boyer, E. Collings, *Materials properties handbook: titanium alloys*. (ASM international, 1993).
42. H. Ledbetter, *Physical Properties Data Compilations Relevant to Energy Storage*. (National Bureau of Standards, 1982).
43. M. J. Donachie, S. J. Donachie, *Superalloys: a technical guide*. (ASM international, 2002).
44. S.-H. Kim, H. Kim, N. J. Kim, Brittle intermetallic compound makes ultrastrong low-density steel with large ductility. *Nature* **518**, 77 (2015).
45. R. C. Reed, *The superalloys: fundamentals and applications*. (Cambridge university press, 2006).
46. A. Naor, N. Eliaz, E. Gileadi, Electrodeposition of rhenium–nickel alloys from aqueous solutions. *Electrochim. Acta* **54**, 6028 (2009).
47. J. van de Lagemaat, K. D. Benkstein, A. J. Frank, Relation between Particle Coordination Number and Porosity in Nanoparticle Films: Implications to Dye-Sensitized Solar Cells. *The Journal of Physical Chemistry B* **105**, 12433 (2001/12/01, 2001).
48. G. Mason, A model of the pore space in a random packing of equal spheres. *Journal of Colloid and Interface Science* **35**, 279 (1971).
49. K. D. Benkstein, N. Kopidakis, J. van de Lagemaat, A. J. Frank, Influence of the Percolation Network Geometry on Electron Transport in Dye-Sensitized Titanium Dioxide Solar Cells. *The Journal of Physical Chemistry B* **107**, 7759 (2003/08/01, 2003).
50. M. Ni, M. K. H. Leung, D. Y. C. Leung, K. Sumathy, An analytical study of the porosity effect on dye-sensitized solar cell performance. *Solar Energy Materials and Solar Cells* **90**, 1331 (2006).
51. J. R. Li, H. F. Cheng, J. L. Yu, F. S. Han, Effect of dual-size cell mix on the stiffness and strength of open-cell aluminum foams. *Materials Science and Engineering: A* **362**, 240 (2003).
52. D. P. Kou, J. R. Li, J. L. Yu, H. F. Cheng, Mechanical behavior of open-cell metallic foams with dual-size cellular structure. *Scripta Materialia* **59**, 483 (2008).
53. T. Y. Tsui, G. M. Pharr, Substrate effects on nanoindentation mechanical property measurement of soft films on hard substrates. *Journal of Materials Research* **14**, 292 (1999).
54. W. C. Oliver, G. M. Pharr, An improved technique for determining hardness and elastic modulus using load and displacement sensing indentation experiments. *Journal of Materials Research* **7**, 1564 (1992).
55. H. Fei, A. Abraham, N. Chawla, H. Jiang, Evaluation of Micro-Pillar Compression Tests for Accurate Determination of Elastic-Plastic Constitutive Relations. *Journal of Applied Mechanics* **79**, 061011 (2012).

CHAPTER 7

CONCLUSIONS AND FUTURE WORK

This dissertation presents the design and fabrication of hierarchical structures that dramatically improved the performance of microbatteries and cellular materials. Colloidal self-assembly with capillary forces combined with electrodeposition and microfabrication enabled hierarchical structures with nm to cm geometric control of multiple chemistries. Colloidal self-assembly is fairly robust and allowed the assembly of 20+ μm thick polystyrene opals across many cm^2 of substrate area with good uniformity. Electrodeposition techniques allowed integration of sensitive chemistries, like lithium, into micrometer wide structures as well as deposition of conformal coatings through structures with < 100 nm pores. Electrodeposition also enabled the precise deposition of chemically incompatible materials within μm proximity to each other, which was critical for the integration of anode and cathode materials into the high power microbattery architecture. Judicious design of the hierarchical microbattery and cellular solid architectures enabled their remarkable performance; however, the designs were ultimately realized through the fabrication technologies developed in this dissertation. Similarly, design traits of high performance hierarchical structures found in nature are known, but, in contrast, their realization through modern manufacturing technologies is not currently possible. The fabrication techniques developed here can be scaled to larger areas through further chemical processing and present methods towards the scalable manufacturing of complex hierarchical materials with multifunctional properties like those present in nature.

The integration of high capacity chemistry into high power hierarchical electrodes enabled microbatteries with unprecedented 7.4 mW cm^{-2} μm^{-1} power and 45.5 μWh cm^{-2} μm^{-1} energy

density. The simultaneous reduction of ion and electron transport resistance in the 3-D interdigitated bicontinuous microelectrodes enabled the high power density. Additionally, any battery chemistry can be integrated into the architecture and achieve high power performance. This is demonstrated by the high power achieved with primary and secondary chemistries. The combination of experiment and simulation allowed for key insights into the microbattery architecture. The electrochemically active material thickness and electron pathways are the most important characteristics for improving high power performance, and not the surface area. Diffusion through the active material as well as migration and diffusion in the electrolyte occur primarily through one material, thus microbattery power performance can be improved by reducing the transport distance that ions or electrons travel through that single material. In contrast, electrical transport occurs through many materials in series and parallel and it is the need for continuous high electrical conductivity in the electrodes that necessitates the bicontinuous architecture. Therefore, when designing battery architectures, special attention should be paid to how that architecture enables continuous electron transport. The physical processes that limit power performance, and thus design and engineering parameters that control those processes, can be broken into two categories: 1) those that can be designed with a threshold that below which have minimal impact on power performance and 2) diffusion through the electrochemically active material which can always be improved with thinner electrodes. Manufacturing constraints, architecture geometry, and side reactions ultimately limit the practical minimal electrode thickness. The design rules developed in this dissertation guide the choice of a single electrode thickness with near maximum performance so as to produce minimal need for compromise on other constraints. The high power design rules that allow these insights into the high power architecture are powerful engineering tools because they are applicable to all

battery architectures and can, in a very simple manner, optimize battery performance and characterize the performance limiting physics. The combination of high capacity materials integrated into high power hierarchical electrodes enabled microbatteries with unprecedented volumetric energy and power densities. Microbatteries with both high energy and power density are attractive for medical, military, and industrial devices that require smaller power sources, faster computation, stronger actuation, long-range telemetry or high current therapy modalities (*1*, *2*).

In addition to high power microbatteries, high specific strength cellular materials with tunable mechanical properties were also developed. The Young's Moduli of microcantilevers fabricated from inverse opal and shell architectures could be controlled from 2.0 to 44.3 GPa by changing the volume fraction and deformation mode of the constituent materials. In addition, a broad set of materials can be integrated into the hierarchical structure, demonstrated with nickel and alumina. The alumina shell microcantilevers had the modulus of polymers, but unlike polymers the alumina is functional at high temperatures, has higher surface area, and can be functionalized with self-assembled monolayers. The integration of hierarchical materials with unique chemical and mechanical properties into micromechanical devices can enable a broad set of new applications in microelectromechanical systems. Nickel inverse opal based cellular solids with specific strength greater than 230 MPa / (Mg m−3) were also studied. The high specific strength, even at low volume fractions, is due to the size strengthening effect of the nanometer sized struts in the inverse opal architecture. The relationship between strut size and yield strength was determined by deconvoluting the size strengthening effect from the porous architecture mechanics. 15 nm effective diameter struts had yield strengths 5X greater than the already high 2.0 GPa yield strength of the bulk nickel. The specific strength of the pure nickel foams exceeds

that of most high strength steel and titanium alloys, but the porous nature allowed the specific stiffness to be varied between that of biological materials and engineering alloys. Perhaps most importantly, the nickel inverse opal cellular solids are easy to assemble, can be processed at room temperature in any lab, and represent a promising platform architecture for measuring the size based strength enhancements in multiple metallic, ceramic, and polymer materials. In addition, self-assembly based fabrication overcomes the small area samples common with other fabrication technologies, enabling large areas of the cellular solids to be fabricated and integrated into engineered devices. Overall, cellular solids based on self-assembly can independently tune material chemistry, deformation mechanics, and materials strength enabling materials with macroscopic properties and technological applications beyond today's alloys and composites.

7.1 Future Work

7.1.1 High Power Architectures and Microbattery Integration

The main obstacle to overcome for the wide spread adoption of high power microbatteries is the fabrication of high aspect ratio hierarchical electrodes. High aspect ratio electrodes are critical to achieve high areal energy and power density, which an important metric for miniature power sources (*3*). A target electrode height of 250 μm would enable energy and power sufficient to power many microelectronic devices. The height and width of the electrodes in the current design is about 15 and 30 μm. A primary constraint in achieving high power porous electrodes is the volumes encompassed by the electrodes need to be filled with a scaffold material, like PS particles, while at the same time the fabrication should prevent electrical shorting between the anode and cathode. This can be achieved by tall vertical walls defined by

the separator width; however a 20 μm separator width, used in the optimized battery configuration from chapter 3, would require an aspect ratio of 12.5:1 to achieve a 250 μm tall electrode. The challenge is to fabricate 12.5:1 aspect ratio features without shorting the electrodes or increasing the separator width. New scalable fabrication methods that allow for microporous high power architectures, like holographic lithography, should be explored to develop high aspect ratio electrodes (*4*). An electrode architecture that could achieve high aspect ratio porous electrodes with a low volume fraction current collector and low cost manufacturing would enable the fabrication of microbatteries with unprecedented energy and power.

A promising area for future work with broad applicability would be applying the model developed in chapter 3 to design and develop high power architectures for conventional format batteries. High power conventional format batteries would enable cell phones and cars that charge in tens of seconds among other useful applications. The microbattery cell optimized for a 50C discharge rate required 80 μm wide electrodes, which is similar to the electrode with of conventional format batteries (*5*). The major changes required to achieve high power density would be integrating a large volume fraction of spherical particles with diameters less than 500 nm with a low volume fraction highly conductive continuous current collector. That challenge would be to integrate this last architecture with the slurry casting manufacturing technique currently used for conventional format batteries so as to maintain low cost, as cost is a key metric of conventional batteries. A new low cost manufacturing technique that takes advantage of the unique requirements of high power architectures could also be developed. Developing techniques to manufacture high power batteries at scale would enable many portable power applications.

7.1.2 High Strength Cellular Materials

Future work could improve the specific strength and modulus of cellular materials by creating microporous foam architectures that primarily deform elastically. The octet-truss architecture is a model architecture that deforms elastically and approaches the maximum homogenous relationship between mechanical properties and relative density, known as the Hashin-Shtrikman bounds (*6, 7*). Fabricating the octet-truss structure with nanometer struts over areas larger than 1 mm^2 has proven difficult (*8*). However, a non-homogenous architecture that primarily deforms elastically could be designed by combining multiple self-assembly technologies that provide more directional control of the nano scale architecture. Eutectic, block-co-polymers, and rods-like template self-assembly instead of spheres could create microporous cellular materials that deform elastically with superior mechanical properties (*9, 10*). In addition, new materials like SiC or high strength carbons could be integrated into the self-assembly process to take advantage of their superior mechanical properties, leading to scalable cellular materials with higher specific modulus and strength.

Perhaps the biggest challenge for high strength cellular solids is overcoming the reduced fracture toughness of foams with small pore sizes. Fracture toughness scales with the square root of the unit cell length and the 3/2 power of the relative density (*11, 12*). Cellular foams that take advantage of the size strengthening effect have the problem of very low fracture toughness due the nanometer size of the struts that make up the open cell architecture. Additionally, it has been challenging to study the fracture toughness of cellular solids with nanometer struts because the small size, less than 100 μm^2, of most high strength cellular solids has made it difficult to test the materials in tension. Cellular solids made from self-assembly allow for sample sizes greater than cm^2 and can be used to study the fracture toughness of cellular materials. It is possible that the

low fracture toughness can be overcome by creating cells with a more directional architecture, at the cost of less homogenous material properties. These materials could them be combined into composites similar to composites made from fibers. In addition, cellular solids made from 2-D nanomaterials that stretch uniformly could present unique opportunities for overcoming the low fracture toughness. The low fracture toughness of cellular solids with nanometers struts is an important obstacle to overcome before these materials can be used in engineering applications with large tensile loads.

7.2 References

1. G. Blomgren, Primary Batteries for Military Applications. *Encyclopedia of Applied Electrochemistry*, 1720 (2014).
2. P. A. Tamirisa, K. Chen, G. Jain, Primary Batteries for Medical Applications. *Encyclopedia of Applied Electrochemistry*, 1713 (2014).
3. T. S. Arthur *et al.*, Three-dimensional electrodes and battery architectures. *MRS Bulletin* **36**, 523 (2011).
4. H. Ning *et al.*, Holographic patterning of high-performance on-chip 3D lithium-ion microbatteries. *Proceedings of the National Academy of Sciences*, (May 11, 2015, 2015).
5. M. Doyle, J. Newman, A. S. Gozdz, C. N. Schmutz, J.-M. Tarascon, Comparison of Modeling Predictions with Experimental Data from Plastic Lithium Ion Cells. *J. Electrochem. Soc.* **143**, 1890 (1996).
6. V. S. Deshpande, N. A. Fleck, M. F. Ashby, Effective properties of the octet-truss lattice material. *Journal of the Mechanics and Physics of Solids* **49**, 1747 (2001).
7. V. S. Deshpande, M. F. Ashby, N. A. Fleck, Foam topology: bending versus stretching dominated architectures. *Acta Materialia* **49**, 1035 (2001).
8. X. Zheng *et al.*, Ultralight, ultrastiff mechanical metamaterials. *Science* **344**, 1373 (June 20, 2014, 2014).
9. M. Fu *et al.*, Anisotropic Colloidal Templating of 3D Ceramic, Semiconducting, Metallic, and Polymeric Architectures. *Advanced Materials* **26**, 1740 (2014).
10. C. Park, J. Yoon, E. L. Thomas, Enabling nanotechnology with self assembled block copolymer patterns. *Polymer* **44**, 6725 (2003).
11. S. Choi, B. V. Sankar, A micromechanical method to predict the fracture toughness of cellular materials. *International Journal of Solids and Structures* **42**, 1797 (2005).
12. S. K. Maiti, M. F. Ashby, L. J. Gibson, Fracture toughness of brittle cellular solids. *Scripta Metallurgica* **18**, 213 (1984).